Chemical bath deposition of Zn(S,O) buffer layers and application in Cd-free chalcopyrite-based thin-film solar cells and modules

Dissertation
zur Erlangung des akademischen Grades
Doktor der Naturwissenschaften
(Dr. rer. nat.)

von
Rodrigo Sáez Araoz

eingereicht im Fachbereich Physik der
Freien Universität Berlin

Angefertigt am
Helmholtz-Zentrum Berlin
für Materialien und Energie

HELMHOLTZ
ZENTRUM BERLIN
für Materialien und Energie

Juni 2009

Eingereicht am: 5. Juni 2009

Tag der mündlichen Prüfung: 4. November 2009

Gutachter:

1.) Frau Prof. Dr. M. Ch. Lux-Steiner

2.) Herr Prof. Dr. J. I. Pascual

To my father.

Contents

Chapter 1

Introduction

Over the last decades, mainly after the oil crisis in 1973[1] [1], energy supply has become a top priority issue, not only for industries, companies and governments, but also for social and ecological groups, as well as for consumers. The highly developed western societies, just like the rest of the world, are now in a desperate need of a cheap, easy-scalable, non-polluting and clean source of energy. Assuming the following facts:

- a run-out of fossil fuels is expected within the next decades,
- the effects of the global warming are becoming increasingly threatening, and
- the growth of the energy demand, not only in developed but also in developing countries is booming,

renewable energy sources seem to provide an optimal solution to the global energy problem. Amongst them, photovoltaics (PV) offers a reliable, clean and easy-scalable way for warmth- and electricity generation, transforming the energy received from the sun. PV also provides cost-effective solutions to the energy supply problem in developing countries by means of the so-called stand-alone systems, not only providing electricity for household applications but also for water pumping systems. It should not be forgotten that according to the United Nations Development Programme (UNDP) and the World Health Organization (WHO), in the year 2000, 2.2 billion people did not have access to electricity and 1.1 billion did not have access to drinking water [2].

Due to their sustainable nature, renewable energy technologies are capable of preserving resources, ensuring the security and diversity of the energy supply and providing energy services virtually without any environmental impact. The increasingly growing

---

[1] The world oil shock of 1973 began in earnest on October 17 1973, when Arab members of the Organization of Petroleum Exporting Countries (OPEC), in the midst of the Yom Kippur War, announced that they would no longer ship petroleum to nations that had supported Israel in its conflict with Egypt. The effects of the embargo were immediate. OPEC forced the oil companies to increase payments drastically. The price of oil quadrupled by 1974.

importance of the PV-market can be seen though some significant figures found in recent studies: according to the Annual World Solar Photovoltaic Industry report for 2007 [3], world solar PV market installations reached a record high of 2.8 GW in 2007, representing a growth of 62% over the previous year. Germany's PV market reached 1.3 GW in 2007 and accounts for 47% of the world market. Spain soared by over 480% to 640 MW, while the United States increased by 57% to 220 MW becoming the world's fourth largest market behind Japan (230 MW). These four countries account for 86% of the world market.

PV market is nowadays still strongly based on silicon technologies. Over 90% of the market share is based on first-generation photovoltaics, mostly due to:

- a well-established knowledge of silicon material science and engineering, knowledge that had a powerful puss-off thanks to the boom of microelectronics,
- an abundant supply of silicon raw material, since silicon makes up 25.7% of the earth's crust by weight,
- a uniform material quality,
- a technology involving no complex processing,
- a production that can be easily upgraded due to the modular structure of the production equipment, and
- the advantages of a low ecological impact with high efficiencies and good stability of the cells if they are properly encapsulated.

However, fabrication costs for crystalline silicon-based PV technologies are high, mainly because of the relatively high price of the crystalline silicon and the need for a large raw material consumption due to its low optical absorption, caused by the indirect nature of the semiconducting material. This is the reason why relatively thick substrates, which are cut from a Czochralsky ingot or from a cast block, are needed.

During the last decades, the main source of silicon for the PV market were the microelectronic companies, which sold the excesses that did not meet the given quality standards (much higher than those requested for PV applications). As the demand rapidly raised, these excesses were not sufficient to satisfy it, thus leading to an increase of the price of crystalline silicon. For this reason, PV is not a competitive energy source in places where conventionally generated power is available and great efforts have been made to try to minimize the fabrication costs. In fact, large cost reductions of nearly 70% were achieved in the decade between 1980 and 1990 [4].

The high cost of crystalline silicon wafers (up to 40-50% of the cost of a finished module) has led the industry to look for cheaper materials to produce solar cells. This second-generation materials have been developed to address energy requirements and production costs. Alternative manufacturing techniques such as vapour deposition or electroplating are advantageous since they reduce high temperature processing significantly. The most successful second generation materials are amorphous and micromorphous silicon, cadmium telluride (CdTe) and the chalcopyrite family Cu(In$_x$,Ga$_{1-x}$)(S$_y$,Se$_{1-y}$)$_2$. These materials are applied as a thin film onto a supporting substrate such as glass, ceramics, stainless steel, or even polyimide thus reducing material costs and final weight. Additionally, the pay-back time of Si-based solar cells is on the scale of 2-3 years, and therefore, 10% of the expected lifetime of a Si-solar module is lost [5]. Thin film solar cells are less demanding and have the potential to achieve payback times of one year [6].

Chalcopyrite-based thin film devices contain a so-called buffer layer, made of cadmium sulphide (CdS). Cadmium is highly toxic and therefore, alternative materials are being sough that can replace CdS without losses in its performance. The preparation and the performance of ZnS as an alternative to CdS will be studied throughout this work.

After a description of the basics of chacopyrite-based thin film solar cells and modules and current voltage characteristics in chapter 2, the chemical bath deposition (CBD) of nominal ZnS layers[2] will be described (Chapter 3). In this chapter the main nucleation processes (heterogeneous and homogeneous) in CBD will be explained before describing the standard CBD process used in this work for the deposition of nominal ZnS buffer layers. The use of a novel optical set-up to monitor the formation of particles in the solution during the deposition process is presented. A model aiming to explain the behaviour of the turbidity (or the transparency, defined in this case as the inverse of turbidity) of the chemical solution during the deposition process is discussed and the conclusions applied to study the effects of varying the CBD conditions (temperature, time, concentration of chemical precursors, etc.).

A morphological and structural study of nominal ZnS buffer layers deposited on CuInS$_2$ (CIS) and Cu(In,Ga)(S,Se)$_2$ (CIGSSe) chalcopyrite absorber materials as well as of the precipitates obtained during the deposition process follows in chapter 4 where important issues such as the deposition rate, the coverage of the underlying absorber layer and the crystalline structure of the buffer layer will be addressed, and correlated with the results previously extracted from the CBD analysis.

Further information about the microstructure of the buffer layer, obtained by means of photoelectron spectroscopy (XPS) is presented in chapter 5. The coverage of the absorber layer and the chemical composition of the buffer layer are discussed. As in the previous case, the correlation of the results found with those obtained from the analysis of the CBD will be highlighted.

In chapter 6 the results obtained by means of XPS are combined with those obtained by ultraviolet photoelectron spectroscopy (UPS) to investigate the band alignment at the CuInS$_2$/ZnS interface and the influence of a heat treatment on the valence band and conduction band offsets.

---

[2] The composition of the buffer layer is a priori considered to be ZnS but the actual composition will be investigated and determined in this work.

Additionally, the photovoltaic performance of ZnS-buffered $CuInS_2$ and $Cu(In,Ga)(S,Se)_2$ devices will be studied in chapter 7, including current-voltage characterization (also as a function of the temperature) in order to find out which are the dominating recombination mechanism that govern the performance of these devices, both under illumination and in the dark. The results obtained from this analysis will be used, together with the schematic band diagram estimated in chapter 6, to proposed a complete model regarding the band alignment in CIS/Zn(S,O)/ZnO solar cell devices, whose accuracy will be tested by simulating these conditions with the simulation software SCAPS 1D.

Finally, the steps followed towards the up-scaling of the studied process, together with the successful results obtained on pilot-line and production scale absorbers provided by the industry will be presented, before ending this work with the conclusions and a brief outlook.

Chapter 2

Basics of chalcopyrite-based thin-film photovoltaic devices

In this introductory chapter, the fundamental concepts of chalcopyrite-based thin-film PV devices are presented. The fabrication process of a thin film device is explained and the function of each of the layers in the device is depicted with emphasis put on the buffer layer. The reasons to replace the CdS layer used in state of the art chalcopyrite based thin film devices are discussed. Finally, the electrical parameters involved in the determination of the conversion efficiency are described.

2.1 Fabrication of chalcopyrite-based thin film PV devices

Chalcopyrite-based solar cells have demonstrated the highest energy conversion efficiency of thin film technologies, reaching 20% in laboratory scale Cu(In,Ga)Se_2 absorbers [7]. In general, these devices consist of a stacked layer sequence of various compounds, as shown in figure 2.1, with a total thickness (excluding the substrate) of a few microns ($\sim$ 2-4 μm).

Typically soda lime glass (SLG) is used as a **substrate** (see figure 2.1) but depending on the desired properties of the device, other substrates can be chosen, such as titanium foil [8] or polyimide films [9], which enable the fabrication of flexible solar cells. The substrate is then coated either by evaporation or by dc-sputtering with a $\sim$0.5 μm thick molybdenum film to provide the device **rear contact** (see figure 2.1).

On top of the rear conctact the **chalcopyrite absorber** (see figure 2.1) layer is deposited. The use of the Cu-chalcopyrite material $Cu(In_xGa_{1-x})(S_ySe_{1-y})_2$ allows the tailoring of the absorber's energy band gap by changing the x=Ga/(In+Ga) and y=S/(S+Se) ratios. Table 2.1 summarizes the various Cu-chalcopyrite materials used in thin film photovoltaics with their corresponding band gaps, which may range from 1.04 eV (for

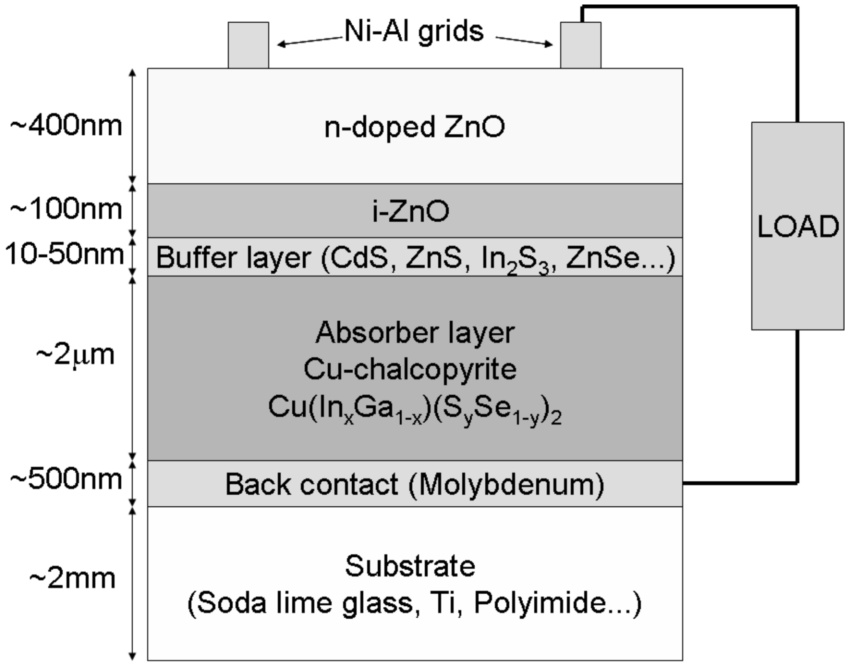

Figure 2.1: Schematic diagram of the layer sequence in a chalcopyrite-based thin film solar cell. The approximate thicknesses of the different layers are also indicated.

$CuInSe_2$) to 2.53 eV (for $CuGaS_2$).

Table 2.1: Different Cu-chalcopyrite materials and corresponding energy band gaps in eV at room temperature. Adapted from [10].

Material	Energy band gap E_g (eV)
$Cu(In_xGa_{1-x})Se_2$	1.04 (x=0) → 1.68 (x=1)
$Cu(In_xGa_{1-x})S_2$	1.51 (x=0) → 2.53 (x=1)
$CuIn(S_ySe_{1-y})_2$	1.04 (y=0) → 1.51 (y=1)
$CuGa(S_ySe_{1-y})_2$	1.68 (y=0) → 2.53 (y=1)

Copper vacancies V_{Cu} have been proposed by different authors as the dominant defect type in Cu-containing chalcopyrites, controlling its acceptor doping concentration (and consistently its p-type), as inferred from first principle calculations [11].

Within this work, $CuInS_2$ and $Cu(In,Ga)(S,Se)_2$ absorbers have been used, delivered respectively by Sulfurcell Solartechik GmbH [12] and AVANCIS GmbH & Co. KG [13]. The corresponding energy band gaps are approximately 1.5 and 1.1 eV respectively. The preparation of the absorber is different in either case. $Cu(In,Ga)(S,Se)_2$ absorbers are prepared in a SEL-RTP (stacked elemental layer, rapid thermal process) line [14]. $CuInS_2$ are prepared in an RTP line [15] by sulfurizing sputtered Cu and In precursors in H_2S atmosphere.

In cases where SLG is used as a substrate, the Na content of the glass plays an important role during the deposition of the $Cu(In,Ga)(S,Se)_2$ absorber, where the high temperatures activate Na-diffusion through the rear contact. It has been experimentally observed that Na has beneficial effects on both electronic and structural properties of $Cu(In,Ga)(S,Se)_2$ compounds, increasing the efficiency of final devices [16]. Na-precursors deposited on the Mo rear contact are also used in high efficiency devices, for a fine control of its incorporation in the absorber film [17]. On the other hand, the beneficial effects of Na are not noticeable in $CuInS_2$ absorbers formed with excess Cu [18] like the ones used for this work.

For Cu-rich grown chalcopyrite materials, like the case of $CuInS_2$, an additional etching step must be performed in order to remove the Cu_xS phase that is formed during the sulphurization of the Cu and In precursors (with a Cu/In ratio of 1.8, i.e., extremely copper rich [18]). This etching step by means of potassium cyanide (KCN) is very selective on Cu-S phases, where the etch rate is 5 orders of magnitude larger than for $CuInS_2$ [19].

A chemical bath deposition (CBD) follows, by which the so-called **buffer layer** is provided (see figure 2.1). Its general task is to minimize recombination of the generated electron-hole pairs around the absorber-window interface, and this is achieved in different ways:

- the buffer layer may influence the energy band alignment, thus achieving an increase in the open circuit voltage [20, 21],
- if the conductivity of the buffer layer is low, it may increase the parallel resistance of the device by insulating possible shorting paths [22, 23],
- the buffer layer may reduce the development of trap states at the absorber/window interface by positively influencing the alignment of the crystal structure [20, 21].

State of the art thin film devices contain a thin layer ($\sim$ 50 nm) of CdS deposited by chemical bath ($E_g(CdS)$=2.4 eV). The aim of this work is to evaluate the feasibility of CBD-ZnS as a buffer layer for Cd-free thin film devices. Other candidates (both in term of materials and deposition techniques) for replacing CdS in solar devices are Ion Layer Gas Reaction (ILGAR)-In_2S_3 [24], Physical Vapour Deposition (PVD)-In_2S_3 [25], or Atomic Layer Deposition(ALD)-Zn(S,O) [26].

The n^+ heterojunction partner is provided by ac-sputtering of a **double layer of ZnO** (a transparent conductive oxide -TCO-, see figure 2.1.) acting as a window, i.e. permitting the visible light to pass through with minor absorption losses and to reach the underlying absorber film ($E_g(ZnO)$=3.3 eV). This window layer typically consists of an intrinsically doped i-ZnO layer (net doping concentration of $N_D \sim 1 \cdot 10^{18}$ cm^{-3}) and a highly doped Al:ZnO layer (net doping concentration of $N_D \sim 1 \cdot 10^{20}$ cm^{-3}). The intrinsic layer prevents Al-diffusion into the buffer and reduces those losses associated to shunts in the p-n structure [27], whereas the high doping concentration of the Al:ZnO ensures that the band bending associated to the p-n- junction takes place to a large extent within the absorber for an optimal collection of photogenerated carriers.

In the case of single cells, the front contact of the device is provided in the form of a **metallic grid** (see figure 2.1) in order to minimize shadowing effects during device operation. A double layer of 10 nm Ni and 1 μm Al is evaporated on the window front surface. The thin Ni layer prevents the rapid oxidation of Al that would result from a direct contact with the ZnO layer, while the Al layer provides the actual ohmic contact of the device.

The simulated band diagram of a state-of-the-art CIGSe/CdS/i-ZnO/ZnO solar cell is shown in figure 2.2. Photons with energy $h\nu < E_g^{ZnO}$ (approx. 3.3 eV) will pass through the window layer. Some photons with energy $E_g^{CdS} < h\nu < E_g^{ZnO}$ (i.e. 2.4 eV $< h\nu <$ 3.3 eV) will be absorbed in the CdS buffer layer, but most of the light will reach the CIGSe layer and be strongly absorbed in the SCR.

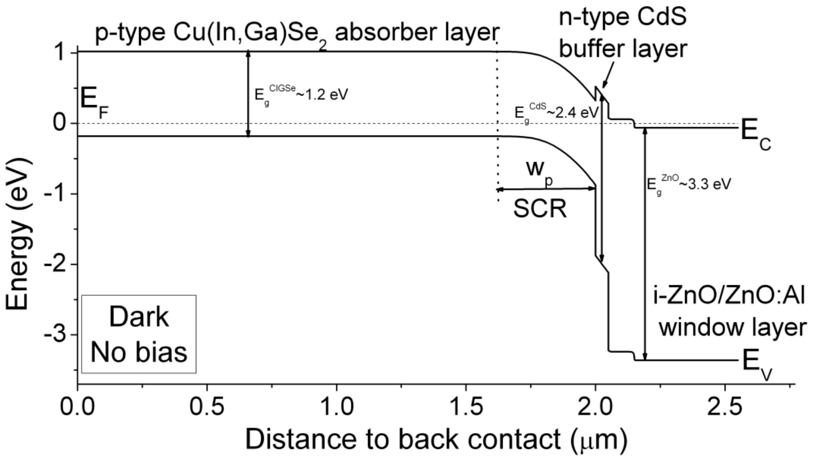

Figure 2.2: Simulated energy band diagram (in the dark and with no applied bias) including the conduction and the valence band of a Cu(In,Ga)Se$_2$/CdS/i-ZnO/ZnO:Al thin film solar cell.

The band alignment at the absorber/buffer interface plays an important role in the carrier transport and will be discussed in the case of wide band gap CuInS$_2$/Zn(S,O) devices in chapter 7.3. The presence of a spike-like conduction band offset up to 0.5 eV can be beneficial [29], whereas the formation of a cliff-like conduction band offset is undesirable, since it opens a recombination path with a lower energy at the interface [30].

The choice of dissimilar materials for the formation of the p-n junction (called in this case p-n heterojunction) is one of the solutions that solve the problem of photogenerating charge carriers outside the space charge region[1], since using an n-type material with an

---

[1] For an extensive overview of semiconductor devices, the reader is referred to [28].

enlarged band gap energy shifts the generation profile directly into the junction. The larger band gap of the window material thus prevents large photogeneration in the n-type region.

One of the benefits of replacing CdS by a material with a larger energy band gap can be clearly seen by analyzing the quantum efficiency of solar cells devices with different buffer layers. Quantum efficiency can be considered as a direct measurement of the performance for which a solar cell is designed, namely the transformation of light into electicity. The external quantum efficiency (EQE) of a solar cell is defined as the ratio of outgoing electrons to incoming photons under given working conditions:

$$EQE(\lambda, V) = \frac{J(\lambda, V)}{q \cdot \phi_{ph}(\lambda)} \tag{2.1}$$

where $J(\lambda, V)$ denotes the electric current density through the device as a function of the incident light wavelength and bias conditions and $\phi_{ph}(\lambda)$ is the illuminating photon flux.

Ideally, a device would show EQE values of unity reagardless of the wavelength of the photons. This would mean that an electron-hole pair is effectively separated for every impinging photon. In the real case, there is a number of factors that bring this number down from unity in all cases:

- A minimum photon energy is necessary to generate charge carriers in the absorber layer. This energy is related to the energy band gap of the material (see table 2.1), and although excitation of charge carriers may occur with photon excitation energies below the gap (e. g. in transitions starting from or ending at defect states within the gap), the probability of occurrence is several orders of magnitude lower than band to band transitions.

- Some of the photons with sufficient energy to generate charge pairs are reflected at the device's top surface. Additionally metal grids providing front contacts to the device constitute an unavoidable reflection source.

- Additional losses occur in processes which do generate electron-hole pairs but whose separation afterwards fail. This can be the result of absorbing photons in the window (or buffer) layer, region in which the minority carriers posses extremely brief lifetimes. A non-effective charge separation can also happen for charge pairs which have been generated within the absorber layer if the diffusion length of the minority carriers is low.

The external quantum efficiencies of a CdS-buffered and a ZnS-buffered $CuInS_2$-based device are shown in figure 2.3. The different loss mechanism previously described are also indicated. Due to the higher energy band gap of ZnS ($E_g(ZnS)$=3.7 eV $>$ $E_g(ZnS)$=2.4 eV) a net current gain of 1 mA/cm^2 is achieved by replacing the CdS by a nominal ZnS buffer layer.

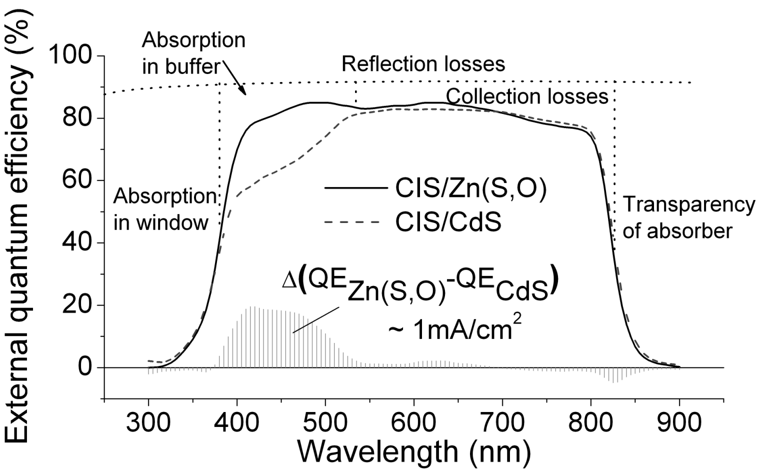

Figure 2.3: External quantum efficiency of a Mo/CuInS_2/CdS/ZnO and a Mo/CuInS_2/ZnS/ZnO device. Different types of losses are schematically shown. The difference in the curves is also plotted and corresponds to a current of approximately 1 mA/cm^2.

Thin film technologies allow for the monolithically integration of solar cells to form solar modules (with sizes of 10x10 and 30x30 cm^2 in this work). In order to achieve this, three additional patterning steps must be introduced in the production chain:

- P1: after the deposition of the Mo back contact, this layer is laser-scribed (e.g. by a Nd:YAG laser at 1064 nm).
- P2: after the deposition of the buffer layer a mechanical-patterning step must be included. P2 patterns both the absorber and the buffer layer.
- P3: after the deposition of the ZnO window layer, a new mechanical-patterning step is performed. P3 patterns the window, buffer and absorber layers.

The schematic representation of the cross section of a thin-film solar module consisting of three monolithically integrated cells is shown in figure 2.4, where the current path is also indicated. In such a configuration, the voltage delivered by each cell is added up to obtain the total output voltage.

The chemical bath deposition of ZnS buffer layers will be the main subject of study in chapter 3, while the characterization of the deposited buffer will be studied in chapters 4 and 5. The photovoltaic perfomance of single cells (0.5 cm^2) and monolithically integrated modules (10x10 and 30x30 cm^2) will be studied in chapters 7 and 8. In the next section, the basics of the photovoltaic characterization by current-voltage analysis will be presented.

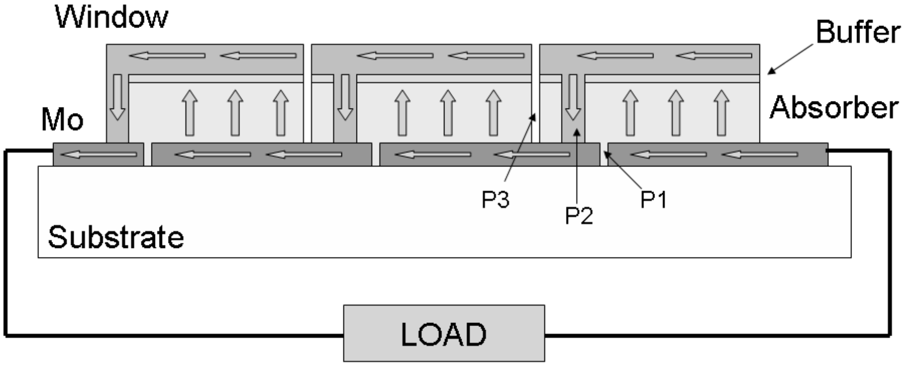

Figure 2.4: Schematic representation of the cross section of a chalcopyrite-based thin film module, consisting of three monolithically integrated cells. The path followed by the current is represented. The distances are not to scale.

2.2 Current-voltage characteristics

Current-voltage characteristics, referred to as I(V) or J(V), depending on whether they are related to the total current (expressed in [A]) or current density (expressed in [A$\cdot$cm^{-2}]) as a function of the applied voltage, are a standard characterization method of the performance of the electric devices in general and solar cells in particular.

J(V) measurements can be performed keeping the sample in darkness (dark I(V) -or J(V)- curves). This analysis provides information regarding the quality of the p-n junction and about losses due to the resistive components of the device. If the J(V) measurements are carried out under illumination, the performance of the solar cell device can be investigated. In particular, the characteristic parameters of the device (open circuit voltage (V_{oc}), short circuit current (J_{sc}) and fill factor (FF)) can be extracted from this analysis. Additionally, J(V) measurements as a function of the temperature and illuminating conditions -J(V,T)- constitute a powerful tool for the identification of the electronic transport mechanism governing the performance of the device under study.

2.2.1 Equivalent circuit. One diode model

Current-voltage analysis considers the solar cell as an electrical device, which can in turn be modeled by an equivalent circuit, with a number of linear (typically resistances) and non-linear (typically diodes and current sources) components. How complex this equivalent circuit can be depends on the performance of the device, but the design always pretends a maximum simplicity, in the sense that it will include the minimum number of components required to account for the performance. State of the art solar cells are commonly fitted using a single- or a double-diode equivalent circuit. The single diode model, which will be used in this work, is routinely used for the characterization of chalcopyrite-based solar cells [31, 32]. Figure 2.5 shows the typical single-diode equivalent circuit used to model the electrical behaviour of a chalcopyrite-based solar cell.

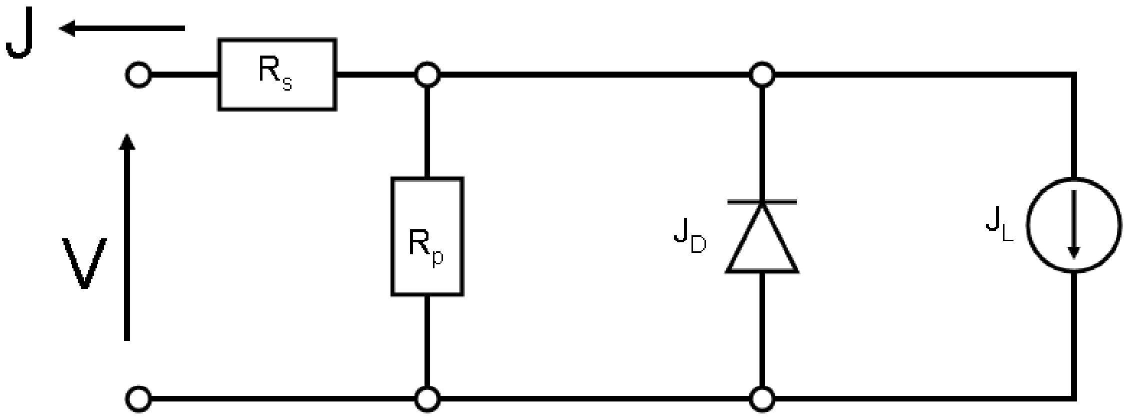

Figure 2.5: Single-diode equivalent circuit of a chalcopyrite based thin film solar cell. The voltage-current characteristic of such a device can be expressed as a function of the diode current density J_D, the current source accounting for the photogenerated current density J_L and two resistive elements; a series resistance R_s and a parallel resistance R_p.

The equivalent circuit accounting for the one diode model includes the following components:

- A diode which models the p-n heterojunction between the absorber layer (p-type) and the buffer-window system (n-type). The diode is characterized by the saturation current density J_0 and the ideality factor A. These will determine the diode current density (J_D) flowing as a function of the applied voltage.
- A current source, which accounts for the photogenerated current density (J$_L$). In certain cases it can be considered to be bias-independent, although this is not the usual case in thin film solar cells, where J_L=$J_L(V)$ (see discussion below). In the case of current voltage characteristics measured in the dark J_L=0.
- A series resistance (R_s), expressed in [Ω] or [Ω·cm^{-2}] depending on whether current (I[A]) or current density (J[A·cm^{-2}]) is considered in the analysis. This component accounts for a number of resistive effects on the electronic transport like contact resistance between the contact probes and the device (at the back and front contacts) and the intrinsic resistivity of the semiconducting layers which are found in the device.
- A parallel resistance (R_p or R_{sh}), expressed in [Ω] or [Ω·cm^{-2}] as in the previous case. This component accounts for all possible alternative electronic paths rather than the diode branch for charge transport. These can be, for example, shunts along grain boundaries or lateral currents at the sample's edge, which would result in effective electronic losses.

The analysis of J(V), and additionally J(V,T) curves, is done by fitting the experimentally obtained data with the circuit elements included in the equivalent circuit (see for example [33]), aiming to reproduce the J(V) characteristic with the right choice of parameters. The current voltage equation applicable to the circuit presented in figure 2.5 reads:

$$J(V) = \underbrace{J_0 \left[exp\left(\frac{q(V - R_s J(V))}{AkT} \right) - 1 \right]}_{1} + \underbrace{\frac{V - R_s J(V)}{R_p}}_{2} - \underbrace{J_L}_{3} \tag{2.2}$$

In the equation, term 1 represents the diode current density, corrected for a voltage drop due to the series resistance. Term 2 corresponds to the current density flowing through the parallel resistance, while term 3 accounts for the photogenerated current density. Figure 2.6 shows the semilogarithmic plot of the absolute value of the current density ($|J(V)|$) in the dark ($J_L = 0$) as a function of the applied voltage.

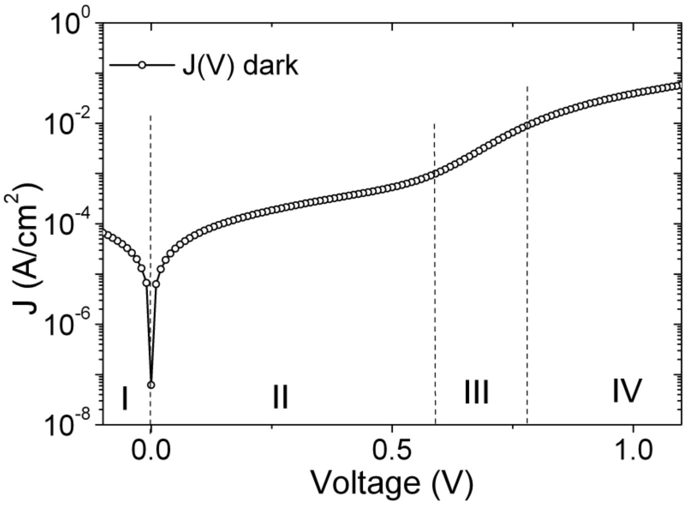

Figure 2.6: Semilogarithmic plot of the absolute value of the current density as a function of the applied bias measured in the dark at 300 K. The approximate domains (I to IV, see discussion in text) where different elements of the equivalent circuit govern the electronic transport are indicated.

The different parameters of equation (2.2) (namely A, J_0, R_s and R_p) control the behaviour of the J(V) in distinct bias ranges. In general, four regions can be distinguished:

- Region I: for applied voltages below 0 V (reverse bias range) and in the ideal case, the J(V) curve is controlled by the saturation current density of the diode, i.e. by thermal generation of free carriers. In the real case, however, the contribution of the parallel resistance also appears.

- Region II: in the low range of forward bias, the saturation current density of the diode and the parallel resistance still control the electronic transport, which is a result of recombination and leak currents.
- Region III: the characteristic exponential dependence of the current on the applied voltage predicts a linear range in the semilogarithmic plot when the electronic transport is governed by the main diode. From this region, information about the ideality factor can be extracted, as it controls the slope of the linear range according to equation (2.2).
- Region IV: above the linear range in the semilogarithmic plot, deviations from the ideal J(V) curve are expected as a result of the effects of the series resistance, which is recorded in the plot as a deviation from the characteristic linearity of region III.

The impact of the elements of the equivalent circuit on the J(V) curve can be seen in figure 2.7 where simulated J(V) curves using equation (2.2) with $J_L = 0$ are presented. The actual value of the parameters will depend on the specific electronic mechanisms governing the charge transport, as it is discussed in appendix B. As it can be seen and was previously described, each of the parameters affects the behaviour of the J(V) curve mainly in one of the four regions. The fitting of the experimental data to equation (2.2) is performed using the least squares method, since it is reported to provide the best parameter fit for the case of dark J(V) curves [34].

On the other hand, the analysis of the J(V) curves obtained illuminating the device could be carried out in the same way as in the case of dark J(V) curves just by adding the constant term J_L accounting for the photogenerated charge carriers. This implicitly assumes the validity of the superposition principle, which states that photogenerated carriers are effectively collected by the junction, regardless of the biasing conditions. This statement is ultimately incorrect, since the voltage applied to the device modifies the space charge region (SCR) width w at the junction and therefore will limit how far electron-hole pairs can be generated in the bulk of the absorber film in order to reach the space charge region and be collected by the junction before they recombine. Assuming that free carriers in the SCR are immediately swept away by the electric field without recombining, the limiting length is given by the so called effective diffusion length L_{eff}, defined as:

$$L_{eff} = w(V) + L_n \tag{2.3}$$

where w denotes the width of the SCR[2] and L_n the diffusion length of the minority carriers. Only in the case of extremely large values of L is $L_{eff} \sim L$ and the superposition principle can be called valid in a first approximation. This is definitely not the case in thin film solar cells, where the SCR width and the diffusion lengths show values within the same order of magnitude [36].

---

[2] the width of the space charge region can be expressed as $w = x_n + x_p = \sqrt{\frac{2\epsilon_0\epsilon_s V_{bi}}{q}\left(\frac{N_A+N_D}{N_A N_D}\right)}$. In the case of a pn$^+$ junction $w \sim x_p$.

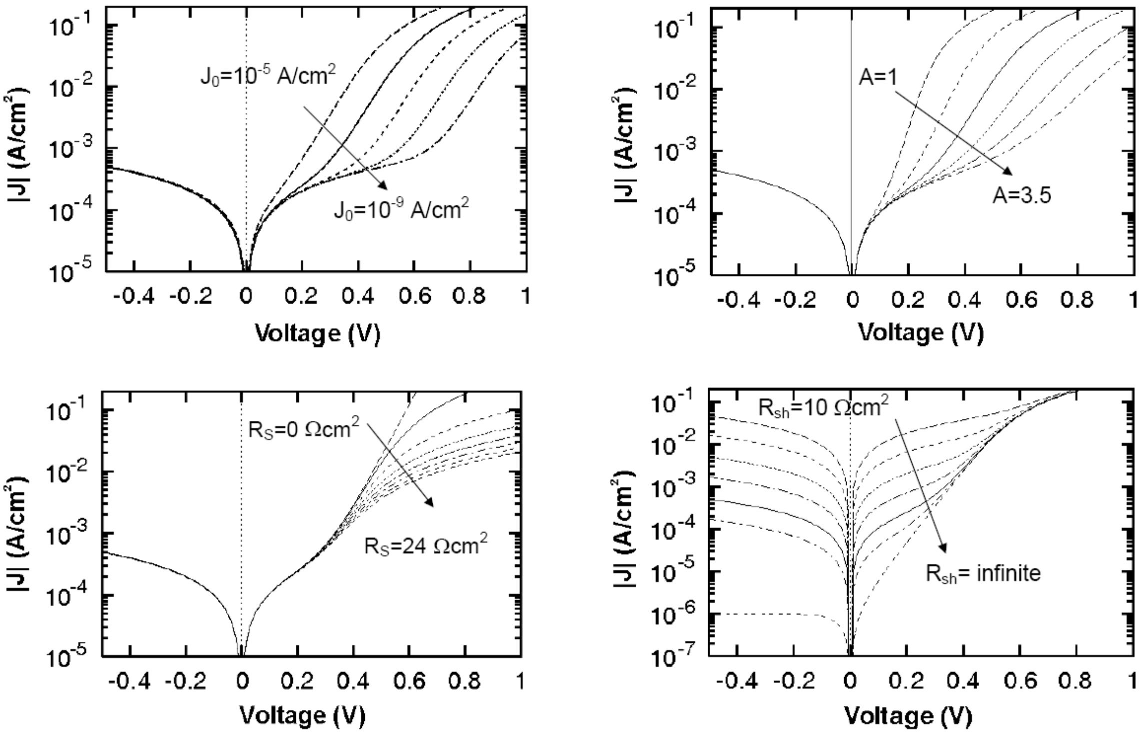

Figure 2.7: Simulated dark J(V) curves obtained from equation (2.2) with varying parameters: saturation current density J_0 (upper left), ideality factor A (upper right), series resistance R_s (lower left) and parallel resistance R_{sh} (lower right). Adapted from [35].

Figure 2.8 shows the dark characteristic of a $CuInS_2$/Zn(S,O) device together with the illuminated curve and that obtained by adding the short-circuit current density to the dark curve. The shadowed area represents the difference between the theoretical light characteristic applying the superposition principle and the real experimentally determined J(V) curve under illumination.

The output of a solar cell is measured as the ratio of the electrical power delivered by the device to an external load to the incoming power from the illumination source:

$$\eta = \frac{P_{out}}{P_{in}} \tag{2.4}$$

where η is referred to as the energy conversion efficiency (or just efficiency) of the solar cell. The power output can be directly obtained from the I(V) characteristic (see figure 2.9), according to:

$$P_{out} = V \cdot I \tag{2.5}$$

and it will be thus given at any operating point by the area of a rectangle enclosed by the corresponding point in the I-V curve and the axes. The power output will be maximum at one particular point, given by I_{MPP} and V_{MPP}, where the subindex denotes *maximum power point*.

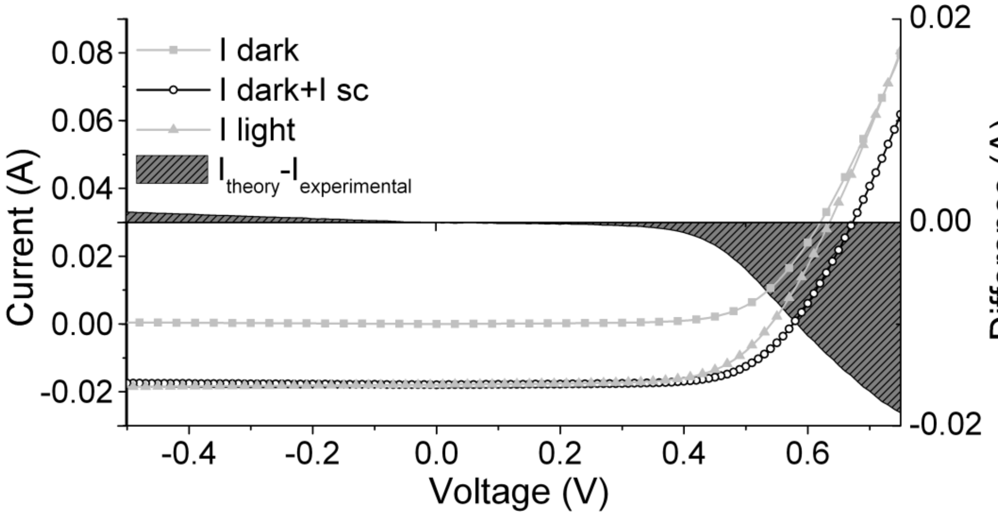

Figure 2.8: Dark and illuminated J(V) characteristic of a $CuInS_2$/Zn(S,O) solar cell, together with the curve resulting from applying the superposition principle, i.e. addition of the short-circuit current density to the dark characteristic. The shadowed area represents the difference between the theoretically calculated and the experimentally determined current density under illumination.

Three parameters are commonly used to characterize the performance of the solar cell under given illumination conditions (see for instance [37]):

- The short circuit current I_{sc} (current at zero bias) ideally represents the photocurrent contribution to the electronic transport. This is the current circulating through an external circuit connected to the metal contacts of the solar cell or module under short-circuit conditions.

- The open circuit voltage V_{oc} (voltage at which $I = 0$) is the maximum voltage obtainable from the device and, ideally, a measurement of the change in electrochemical potential of electrons and holes with respect to their equilibrium conditions in the darkness.

- The fill factor FF of the I(V) curve, defined as:

$$FF = \frac{V_{MPP} I_{MPP}}{V_{oc} I_{sc}} \tag{2.6}$$

  which can be understood as a measurement of the *squareness* of the I(V) characteristic. Equivalently it is the area ratio between the rectangle of maximal area enclosed by the axis and the experimental I(V) curve and that enclosed by the axis and the corresponding parallels at I_{sc} and V_{oc}.

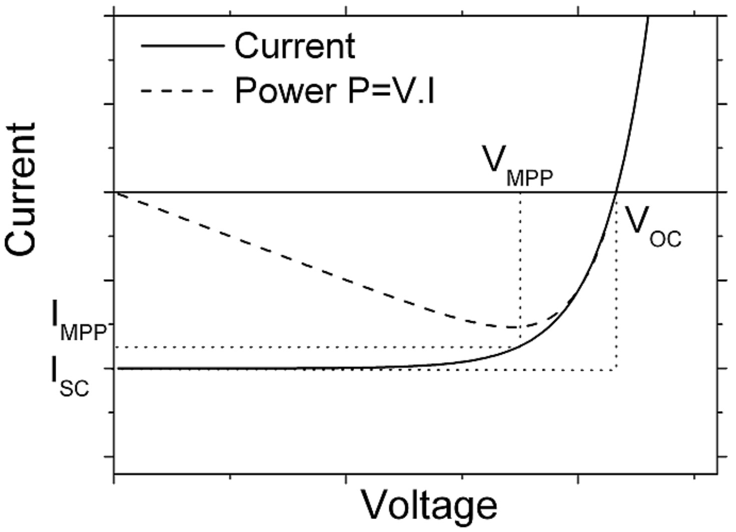

Figure 2.9: Schematic representation of the current-voltage and power-voltage (P=I·V) characteristic of a solar cell device. The voltage and current at the maximum power point (V_{MPP} and I_{MPP}) as well as the open circuit voltage (V_{OC}) and the short circuit current (I_{SC}) are indicated.

Finally, the energy conversion efficiency of the device can be written as:

$$\eta = \frac{I_{sc} V_{oc} FF}{P_{in}} \tag{2.7}$$

An authoritative summary of the current state of the art (January 2009) efficiencies including the highest confirmed efficiencies for a range of photovoltaic cell and module technologies (silicon, III-V, thin film chalcogenide, amorphous Si, photochemical, organic and multijunction devices) is found in reference [38]. In the case of chalcopyrite-based thin film solar devices, a conversion efficiency under standard test conditions of 20.0±0.6 % has been achieved by a Cu(In,Ga)Se_2 cell on a glass substrate (aperture area = 0.419 cm^2).

Chapter 3

Growth of ZnS buffer layers by chemical bath deposition

In the sections included in this chapter, the basic theory of chemical bath deposition (CBD) will be presented, including a short historical review, the definition of concepts such as homogeneous and heterogeneous nucleation and the explanation of how the crystallites formed by CBD may grow to form either a bigger crystal or an aggregate of crystallites. In section 3.1.2, the four deposition mechanisms of the chemical bath will be introduced including the simple and complex decomposition mechanisms (both of them divided into ion-by-ion and cluster-decomposition). Once the fundamental knowledge about CBD has been presented, the chemical bath deposition process developed and patented at the Helmholtz-Zentrum Berlin will be introduced and the influence of the different process parameters (e.g. process temperature, concentration of chemicals) will be analyzed. In order to do this analysis, a novel monitoring system has been developed. The transparency of the solution is measured in situ during the process and effects of the parameters on this curve will be discussed as the decrease of the turbidity is intimately related to the concentration of particles in the solution. A model describing the transparency curve as a function of time will be presented and used to compare the impact of the different process parameters on the formation of particles in the chemical solution.

3.1 Basics of chemical bath deposition

Chemical bath deposition is a technique that produces a solid film on a substrate on a single immersion through the control of the kinetics of formation of the solid. It is the aqueous analogue of chemical vapour deposition (CVD) [39], since both processes involve mass transport of reactants, adsorption, surface diffusion, reaction, desorption, nucleation and growth. The CBD process enables the deposition of thin films, generally chalcogenides (M_2X_m, X=O, OH, S, Se, Te), on substrates submerged in solutions containing metallic ions and a source of oxide, hydroxide, sulfide, selenide or telluride ions. In 1835

Liebig reported the first deposition of silver using a chemical solution technique [40]. The first reported CBD of a compound semiconductor film appears to be the formation of PbS, SbS and CuS on various metals from thiosulfate solutions of lead acetate, copper sulphate and antimony tartrate [41]. PbS was subject of much attention during the early studies of CBD. In 1884, deposition of PbS films by reaction between thiourea (TU) and lead tartrate was reported [42]. Infrared photoconductivity in chemical bath deposited PbS films was described in 1906 [43, 44] and this application can be considered as the central driving force for subsequent investigation in chemically deposited lead chalcogenide films to the point that CBD is the main technique used in making commercial PbS and PbSe infrared detectors [45, 46]. It was in 1961 when the deposition of CdS films by CBD was explicitly reported for the first time [47] and it is now the most widely studied material in CBD. The range of materials deposited by CBD was gradually extended and now includes sulphides and selenides of many metals [48, 49], some oxides [50], CdTe [51] and also many ternary compounds.[1] These ternary compounds contain either two metals [52], two chalcogenides [53] or have part of the chalcogenide substituted by a hydroxide group [54]. CBD received an important impetus after CdS films chemically deposited on CdTe [55] and $CuInSe_2$ [56] absorbers were shown to give superior photovoltaic cells compared with the previously evaporated CdS. Nowadays CBD is universally used to form the CdS layer on both CdTe and chalcopyrite thin film photovoltaic cells.

Chemical bath deposition has been used to deposit films of different semiconductors, since it is probably the simplest method available (at least in terms of necessary equipment and energy consumption) for this purpose. Despite the experimental simplicity (only a vessel containing an aqueous solution made up of few, usually common chemicals and the substrate onto which the layer will be deposited are needed), it is a complicated task to understand the mechanisms involved in the deposition process. In principle, CBD can be used to deposit any compound that satisfies the following four basic requirements [57]:

- It should be possible to create the compound by simple precipitation. This generally, although not exclusively, refers to the formation of a stoichiometric compound formed by ionic reaction.[2]
- The compound should be relatively (and preferably highly) insoluble in the solution used.
- The compound should be chemically stable in the solution.
- If the reaction proceeds via the free anion, then this anion should be slowly generated (to prevent sudden precipitation). If the reaction is of the complex-decomposition type, then decomposition of the metal complex should similarly occur slowly.

---

[1] For a extensive list of binary and ternary materials deposited by CBD, the reader is referred to the book entitled Chemical Solution Deposition of Semiconductor Films, [57].

[2] Ionic reactions are those in which ions do not change charge but simply change partners.

3.1.1 Nucleation and crystal growth

Film formation may take place from two distinct mechanisms. The first one is a growth mechanism involving the reaction of atomic species at the surface. It corresponds to an atom-by-atom process, also called "ion-by-ion" [58]. The second deposition mechanism is associated to the agglomeration of colloids formed in the solution. It can be considered a cluster-by-cluster growth. In practical situations both processes may interact, leading to films where colloids are included in the growing film [59, 60]. In other words, the formation of nuclei can occur by heterogeneous nucleation on the substrate or by homogeneous nucleation in the bulk solution respectively.

Homogeneous nucleation

Homogeneous nucleation can occur due to local fluctuations in the solution - whether in concentration, temperature or other variables. The first stage of the growth is collision between individual ions or molecules to form embryos[3]. These embryos grow by collecting individual species that collide with them. The adsorption of ions on the embryo seems to be the most probable growth mechanism. If the concentration of embryos in the solution is large, collisions between embryos can also play an important role. These embryos may redissolve in the solution before they have a chance to grow into stable particles, called nuclei. The critical radius, R_c, is the size where the embryo has a 50% chance of redissolving (i.e. a 50% chance of growing into a stable nucleus). It is determined by the balance between the surface energy required to form the embryo, $E_s = 4\pi R^2\sigma$ (where σ is the surface energy per unit area, defined as the excess energy at the surface of a material compared to the bulk) and the energy released when a spherical particle is formed, $E_r = 4\pi R^3\rho L/3$ (where ρ is the density of the solid and L [KJ/mol] is the heat of the solution). The resulting expression for R_c is $R_c = 3\sigma/(\rho L)$, and its typical size for ZnS is between 1 and 2 nm in diameter (around 100 molecules)[57].

Heterogeneous process

In the heterogeneous nucleation process, unstable embryos with radius smaller than R_c or even individual ions can adsorb onto the substrate. The energy required to form an interface between an embryo and the solid substrate will usually be less than the energy required for homogeneous nucleation, where no such interface exists, due to the catalytic function of the substrate. Therefore, heterogeneous nucleation is energetically preferred over homogeneous nucleation. These sub-critical nuclei can grow either by surface diffusion or by material addition from the solution.

---

[3] Embryos are defined as nuclei that are intrinsically unstable against re-dissolution.

Crystal growth

Once stable nuclei have been formed, there are several ways in which they can increase in size. An obvious one is a continuation of the process of embryo growth discussed above: adsorption of ionic species from the solution onto the nucleus. This type of crystal growth can be therefore considered a self assembling process. Another mechanism for crystal growth is known as the Ostwald ripening, which is an spontaneous process that occurs because larger particles are more energetically favored than smaller ones due to a reduction of the surface energy [62]. This stems from the fact that molecules on the surface of a particle are energetically less stable than the ones already well ordered and packed in the interior. Large particles with lower surface to volume ratio result in a lower energy state. As the system tries to lower its overall energy, molecules on the surface of a small, energetically unfavorable particle will tend to diffuse through the chemical solution and add to the surface of the larger particle. The result is that the larger crystals grow at the expense of the smaller ones.

Collision between particles can also play an important role in the crystal growth if the concentration of particles is high enough, since the probability of a collision between two particles increases with their concentration. This may result in either aggregation or coalescence. In the process of aggregation, when two particles approach each other under the presence of an attractive force (the most common one is the van der Waals force of attraction, due to an induced dipole-induced dipole interaction between particles) they will tend to stick together. The result is a large particle called aggregate. Grain boundaries are found between individual crystals in an aggregate. However, under certain conditions, surface diffusion may occur where two or more particles have aggregated, resulting in the formation of a neck. This process is called coalescence and may continue until one large particle is formed from the original aggregate.

3.1.2 Film growth in chemical bath deposition

Although chemical bath deposition of semiconductor compounds has been in use for a long time, most publications do not explain the growth mechanisms and they are often unclear. The reason is that there are several of them, which can be divided into four fundamentally different types: the simple ion-by-ion, the simple cluster, the complex decomposition ion-by-ion and the complex decomposition cluster mechanism.

In the ion-by-ion growth, for nucleation to occur homogeneously in a particle free solution, a high degree of supersaturation is needed. The presence of a surface (substrate or the walls of the reaction vessel) introduces a degree of heterogeneity that facilitates the nucleation. For this reason, deposition that proceeds via the ion-by-ion process tends to occur mainly on the substrate or other surfaces, rather than involving a large amount of precipitate (which is typical of the cluster mechanism). In this case, the surface can be considered a catalyst for the nucleation.

In the cluster mechanisms (also called hydroxide mechanisms) the nucleation of the chalcogenide is simpler, since a solid phase is already present and the process occurs by a substitution reaction on that solid phase. In this case, the initial step is the deposition and adhesion of the hydroxide onto the substrate. This hydroxide is then converted into the chalcogenide. At the same time, more hydroxide and, as the reaction goes on, more chalcogenide and partially converted hydroxide moves to the substrate, where it may stick, either to the uncovered substrate or to already deposited material, following essentially the same process as aggregation, which was previously described. In this case, since the initial nucleation of hydroxide occurs homogeneously in the solution, the chalcogenide is also formed in this way and therefore usually precipitates out of the solution to a large extent. Film formation occurs when high surface energy particles reach the substrate (or any other surface) before they precipitate.

One expected difference between ion-by-ion and cluster mechanism is that in the latter, since colloids from the solution stick to the substrate surface, the crystal size is not expected to change greatly with film thickness (the crystal size may increase since the colloids themselves can grow via ion-by-ion mechanism). For ion-by-ion growth, it is likely that crystal growth occurs on nuclei already present on the substrate, and therefore crystal size may increase with deposition time.

For the following discussion, and for all four previously named growth mechanisms, the sulphide ions are generated through the decomposition of thiourea ($SC(NH_2)_2$) in aqueous solution, according to the following reactions [63]:

$$SC(NH_2)_2 + OH^- \rightarrow SH^- + CH_2N_2 + H_2O \tag{3.1}$$

$$SH^- + OH^- \rightleftharpoons S^- + H_2O \tag{3.2}$$

which lead to the release of sulphide ions.

The presence of a cation that can precipitate an insoluble sulphide is necessary for the decomposition to proceed at a reasonable rate. In this case metal ions remove sulphide ions, which in turn drive the equilibrium continually to the right.

The simple ion-by-ion mechanism

The (chemically speaking) simplest mechanism is usually called the ion-by-ion mechanism, since it occurs by sequential ionic reactions. For the case of zinc complexed with ammonia (zinctetraamine) firstly there is a dissociation of the complex to release Zn^{2+} ions:

$$Zn(NH_3)_4^{2+} \rightleftharpoons Zn^{2+} + 4NH_3 \tag{3.3}$$

At the same time the sulphide ion is formed

$$SC(NH_2)_2 + 2OH^- \rightarrow S^{2-} + CH_2N_2 + 2H_2O \tag{3.4}$$

The ionic reaction of S^{2-} and Zn^{2+} forms the ZnS molecule.

$$Zn^{2+} + S^{2-} \rightarrow ZnS \tag{3.5}$$

If the ion product $[Zn^{2+}][S^{2-}]$ exceeds the solubility product K_{sp} of ZnS, then, neglecting kinetic problems of nucleation, ZnS will be formed as a solid phase. Since the reaction is normally carried out in alkaline solution, a complex is then needed to keep the metal ion in the solution and to prevent the hydroxide from precipitating. This chemical deposition mechanism is illustrated in figure 3.1 for ZnS.

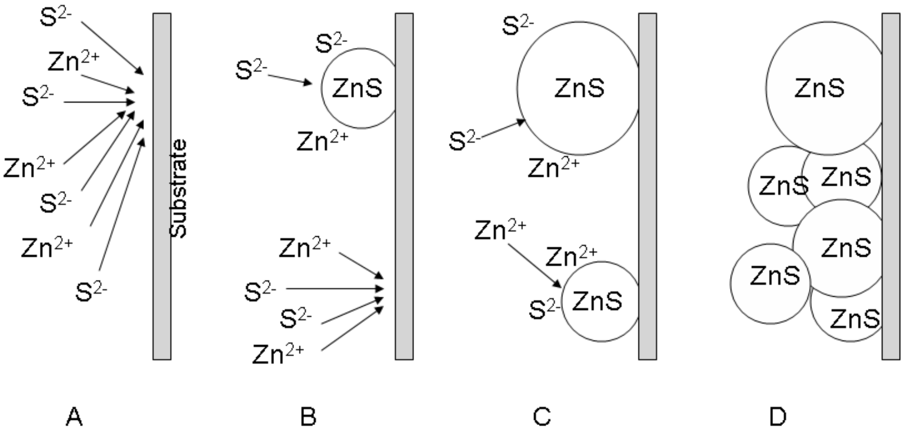

Figure 3.1: Schematic diagram showing the probable steps involved in the ion-by-ion mechanism for the case of ZnS. A: Diffusion of S and Zn ions onto the substrate. B: Formation of ZnS nuclei facilitated by the substrate. C: Growth of the ZnS nuclei by adsorption of Zn and S ions from the solution while new ZnS are nucleated. D: Growth of ZnS crystals which adhere to each other. Adapted from [57].

The simple cluster (hydroxide) mechanism

It was previously stated that complexation of zinc was necessary to prevent $Zn(OH)_2$ precipitation. However, metal hydroxides also play a role as reaction intermediates in the CBD process. If the complex concentration is not high enough to prevent completely the formation of $Zn(OH)_2$, a relatively small amount of this complex may be formed, not as a visible precipitate, but as a colloid. ZnS is then formed by reaction of slowly generated S^{2-} ions with $Zn(OH)_2$.

The first step is the formation of a zinc hydroxide cluster:

$$nZn^{2+} + 2nOH^{-} \rightarrow [Zn(OH)_2]_n \tag{3.6}$$

And then, the exchange reaction of the cluster with the sulphide ions generated according to reaction (3.4) forms the ZnS.

$$[Zn(OH)_2]_n + nS^{2-} \rightarrow nZnS + 2nOH^- \tag{3.7}$$

Reaction (3.7) occurs because the solubility product for ZnS (K_{sp}=3·10^{-25}) is much smaller than for Zn(OH)$_2$ (K_{sp} =10^{-16}). The hydroxide cluster mechanism is schematically described in figure 3.2.

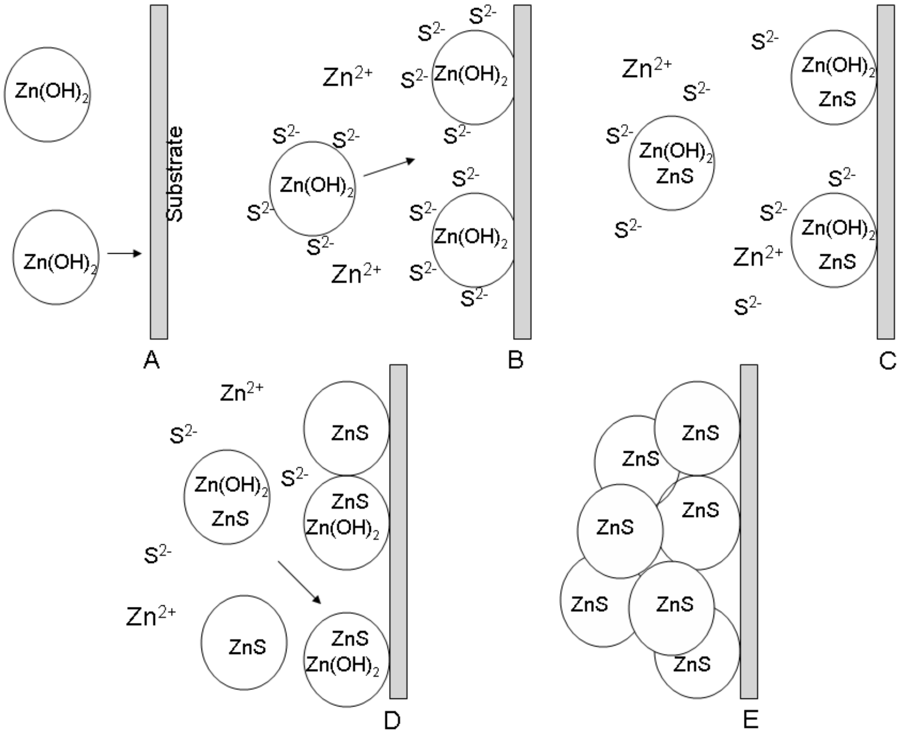

Figure 3.2: Schematic diagram describing the probable steps in the hydroxide mechanism for the case of ZnS. A: Diffusion of hydroxide colloids to the substrate. B: Adhesion to the substrate and reaction with sulphur ions. C: Exchange of the hydroxide by sulphide, probably starting at the surface of the colloids. D: Reaction continues until most of the hydroxide is converted to sulphide. E: ZnS particles adhere to each other and form an aggregated film. Non adsorbed particles will also aggregate and precipitate out of the solution. Adapted from [57]

The chalcogenide precursor (thiourea in this work) does not only form chalcogenide ions, but form also complexes with metal ions, which give raise to the complex-decomposition mechanisms (both ion-by-ion and cluster).

The complex decomposition ion-by-ion mechanism

Consider the complexation of a free Zn^{2+} ion by thiourea to give a Zn-thiourea complex ion:

$$(NH_2)_2CS + Zn^{2+} \rightleftharpoons [(NH_2)_2CS—Zn]^{2+} \tag{3.8}$$

This ion could, in principle, hydrolyze by breaking the S—C bond to form ZnS:

$$[(NH_2)_2CS—Zn]^{2+} + 2OH^- \rightarrow ZnS + CN_2H_2 + 2H_2O \tag{3.9}$$

If the Zn^{2+} ion is adsorbed on the substrate or on previously deposited ZnS, the same reaction would occur. If the ZnS so formed remains bound to the substrate, the result would be a film growth by an ion-by-ion complex-decomposition mechanism.

The complex decomposition cluster mechanism

The basis of this mechanism is that a solid phase is formed but, instead of reacting directly with the free anion, it forms an intermediate complex with the "anion-forming" reagent.

$$—Zn(OH)_2 + (NH_2)_2CS \rightleftharpoons Zn(OH)_2—S—C(NH_2)_2 \tag{3.10}$$

where —$Zn(OH)_2$ is one molecule in the solid phase $Zn(OH)_2$ cluster. This complex then decomposes to ZnS:

$$Zn(OH)_2—S—C(NH_2)_2 \rightarrow ZnS + CN_2H_2 + 2H_2O \tag{3.11}$$

which means that the S—C bond of the thiourea breaks, leaving the S bound to Zn.

The use of the thiourea-Zn ligand in Eq. (3.9) is for simplicity. In a general way, as long as a solid phase of $Zn(OH)_2$ is not present, the hydroxy-thiourea-Zn complexes involve an ion-by-ion mechanism. This will not be the case of the complex decomposition cluster mechanisms, where a solid phase of $Zn(OH)_2$ is present, as it is the case in equations (3.10) and (3.11). It can be therefore said that the presence or absence of hydroxide particles in the solution governs the transition between ion-by-ion and colloidal growth [59].

An schematic diagram of the complex decomposition mechanism is presented in figure 3.3

3.2 Chemical bath deposition of Zn(S,O)

Deposition of ZnS buffer layers as an alternative to CdS in thin film photovoltaic devices has been developed and tested by many groups, each using a different recipe and naming the resulting layer in different ways which, depending on the composition, can be as simple as CBD-ZnS [64], or Zn(S,OH) [65, 66, 67], ZnS(O,OH) [68, 69, 70] or even $ZnS_xO_yH_z$ [71]. In the following section, the chemical bath deposition process of a

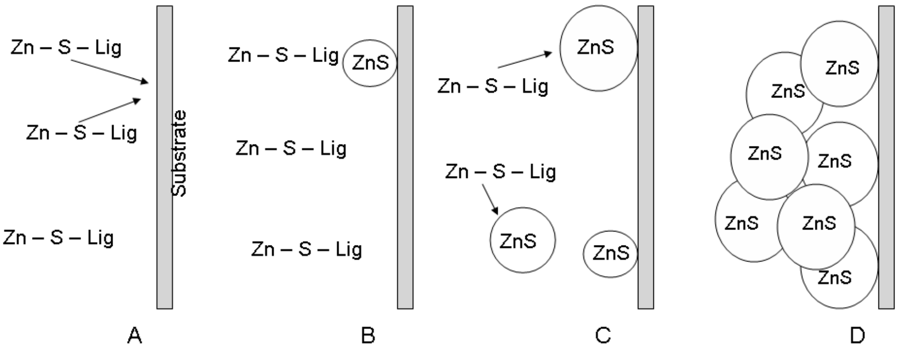

Figure 3.3: Schematic diagram showing the possible steps involved in the complex-decomposition mechanism for the case of ZnS. The complex Zn—S—Lig, where Lig is a ligand (or part of the S-forming species) decomposes to ZnS on the substrate and homogeneously in the solution (A, B). ZnS nuclei formed grow by adsorption and decomposition of more complex species (C) until a film of aggregated crystals is formed (D). Adapted from [57].

Zn(S,O) buffer layer will be described. This process has been developed [72], [73, 74]*[4]. and patented [75] at the Helmholtz-Zentrum Berlin für Materialien und Energie. The reason for these mixed ZnS, ZnO and $Zn(OH)_2$ phases in the composition is due to the difference between the solubility products of zinc hydroxides ($K_{sp} = 10^{-16}$) and zinc sulphide ($K_{sp} = 3 \cdot 10^{-25}$). Since hydroxide ions are present at much higher concentrations than sulphide, hydroxide formation and stability against sulphurization is likely to happen for Zn. Therefore, as ZnS is deposited under conditions where $Zn(OH)_2$ can be formed, there is usually no evidence of the absence of some zinc hydroxide or zinc-oxygen species, even if ZnS is identified (by XRD for example).

3.2.1 Standard deposition of Zn(S,O) buffer layers

Zn(S,O) thin films can be prepared by decomposition of thiourea in an alkaline solution containing a zinc salt and a suitable complexing agent which allows for obtaining a soluble species of Zn^{2+} in this medium.

The first step of the chemical bath deposition process consists in preparing the chemical solution. This takes place is various stages. Firstly, the whole amount of the zinc precursor ($ZnSO_4 \cdot 7H_2O$; [0.15 mol/l]) is added to the whole volume of de-ionized water heated up to a temperature of $50\,^{\circ}\mathrm{C}$. The zinc salt dissolves and acts as the source of Zn^{2+} ions, which are also present in a concentration of 0.15 M.

$$ZnSO_4 \rightarrow Zn^{2+} + SO_4^{2-} \tag{3.12}$$

Once the temperature of the solution reaches $70\,^{\circ}\mathrm{C}$, thiourea ($SC(NH_2)_2$; [0.6 mol/l])

---

[4] References marked with * have Rodrigo Sáez-Araoz as an author and show results related to this work.

is added under stirring. This leads to the formation of zinc-thiourea complexes, one of which is tris (thiourea) zinc sulphate (ZTS), a semi-organic material with molecular formula $Zn(NH_2CSNH_2)_3SO_4$ [76].

At this point Zn^{2+} ions are reacting with thiourea to form ZTS. This reaction is allowed to take place for approximately three minutes, when an excess of ammonia (NH_3; [4 mol/l]) is added to the solution, allowing the remaining Zn^{2+} ions (not bound to thiourea) to form zinc-ammonia complexes [77]:

$$Zn^{2+} + 4NH_3 \rightleftharpoons Zn(NH_3)_4^{2+} \qquad K = 10^{8.9} \tag{3.13}$$

The addition of ammonia causes in the first place a fast precipitation of $Zn(OH)_2$, as described by

$$Zn(OH)_2 \downarrow \rightleftharpoons Zn^{2+} + 2OH^- \qquad K = 10^{-16.9} \tag{3.14}$$

which is rapidly redissolved if enough ammonia is added, since the equilibrium reaction (3.14) will shift to the right in order to replace the Zn^{2+} ions that have been complexed with ammonia as described by the reaction (3.13) [77].

Since an alkaline pH is required to decompose the thiourea to sulphide (following equation (3.1) and (3.2)), a complexing agent is needed in order to prevent $Zn(OH)_2$ precipitation. Ammonia is also used as a complexant for Zn, which prevents the formation and precipitation of $Zn(OH)_2$.

At room temperature, for a pH of ∼11 ($[OH]^- \sim 10^{-3}$) and given the solubility product of $Zn(OH)_2$ ($K_{sp} \approx 10^{-17}$) it can be calculated that a Zn concentration above 10^{-11} M is enough to initiate $Zn(OH)_2$ formation. If more ammonia is added to a suspension of $Zn(OH)_2$, the $Zn(OH)_2$ will redissolve. The amount of ammonia can be calculated from the stability constant of the complex between ammonia and zinc. The equilibrium of this reaction to form the zinc tretraamine complex is given by reaction (3.13).

From this reaction, for a maximal zinc concentration of 0.15 M (no zinc ions complexed with thiourea), it can be found that a free ammonia concentration of ∼2.1 M will result in a free Zn^{2+} concentration of 10^{-11} M. After adding the amount of ammonia tied up by the complexation (4×0.15 M), the minimum NH_3 concentration required to prevent precipitation of $Zn(OH)_2$ is ∼2.7 M.

After the excess of ammonia has been added, samples are submerged in the solution. The initial induction time is determined by the rate of decomposition of thiourea and formation of ZnS particles in the solution. During the first stage of the CBD process, the concentration of ammonia is high enough to prevent the formation of $Zn(OH)_2$, and thus, an ion-by-ion mechanism is favoured. This can be either the simple ion-by-ion mechanism (described in figure 3.1), where the decomposition of the zinc tetraamine complex and/or ZTS release free Zn^{2+} ions that react with the S^{2-} ions originated by the decomposition of thiourea (equations (3.1) and (3.2)), or the complex decomposition ion-by-ion mechanism (see figure 3.3), where it is the reaction of the Zn-thiourea complex with hydroxide ions what forms the ZnS according to equations (3.10) and (3.11).

During this time, the temperature of the bath is kept above 70 °C, which in turn favours the evaporation of ammonia, thus reducing the pH and changing the conditions in the chemical bath. For a reduced ammonia concentration, formation of solid $Zn(OH)_2$ phases may happen, and the probability of film formation based on the cluster mechanisms (both simple and complex) increases. Furthermore, if a cation is complexed with ammonia and the ammonia is lost due to evaporation (if the heated solution is not closed, for example), the free-cation concentration will gradually increase as ammonia is lost, which will in turn, increase the particle formation rate.

Additionally, during the deposition time, the $Zn(OH)_2$ not forming ZnS converts to ZnO at bath temperatures above 50 degrees [78]. Therefore the expected composition of the layer is a Zn(S,O) layer. The ZnS/(ZnS+ZnO) ratio is a function of the deposition conditions. The morphology and the composition of the chemically-deposited buffer layer will be studied in chapters 4 and 5.

3.2.2 Post deposition treatments

After the deposition of the Zn(S,O) buffer layer, the sample undergoes additional treatments before the processing of the cell can be continued (e.g. by rf-sputtering the ZnO window layer, see figure 2.1). After removing the sample from the chemical bath, $Zn(OH)_2$ aggregates can be found on the surface of the sample, with sizes up to several mm^2. These remaining $Zn(OH)_2$ can be eliminated if, directly after the deposition, the sample is rinsed with ammonia in aqueous solution (2.5%). If the samples were rinsed with deionized water, uncontrollable precipitation of $Zn(OH)_2$ would occur. Since the sample still has residual Zn^{2+}-containing ammonia solution on its surface, rinsing it with water would drastically decrease the pH value and initiate the formation of more $Zn(OH)_2$, which in consequence would precipitate on the sample.

Once the sample is rinsed and dried using a N_2 gun, it undergoes a heat treatment in air. The samples are annealed at temperatures around 200 °C, for some minutes in order to eliminate remnants of water in the layer. This step may also help to convert any remaining $Zn(OH)_2$ into ZnO and has also an important impact on the crystallinity of the layers. Bigger crystallites are formed in the buffer layer by coalescence of individual particles.

3.3 Monitoring the CBD process

As it was stated earlier (see section 3.1), CBD is a very simple deposition technique in terms of experimental requirements. Nevertheless, in order to obtain high reproducibility, to study the influence of the many CBD parameters (e.g. temperature, concentrations, time) and to test the possible implementation of the process into an industrial pilot line, some modifications have been added to the basic set up consisting in the water jacket and the bath temperature controller. An schematic illustration of the set up used for the CBD process is shown in figure 3.4.

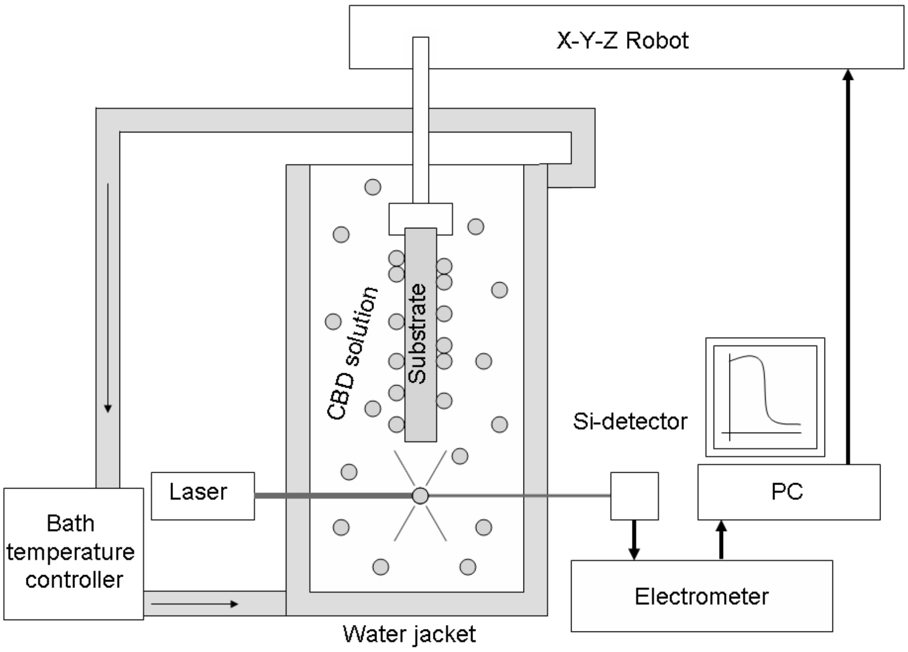

Figure 3.4: Schematic description of the CBD set up containing a bath temperature controller, a water jacket, the transparency measurement system consisting of a laser light source and an Si-detector, and the X-Y-Z robot for full process automatization.

The CBD is carried out in a water jacket attached to a bath temperature controller, which heats and pumps the water through the inner walls of the water jacket. During the process, the turbidity[5] of the solution is monitored by means of a laser light source (a LPM635-03C laser with a maximal power output of 3.0 mW and an operating wavelength of 635 nm) and a Si-detector. The response of the optical sensor is proportional to the intensity of the detected light, and the photocurrent delivered is sent to a computer program for analysis and display. Furthermore a programmable X-Y-Z robot may be used to make the process fully automatic. Two different end-conditions can trigger the end of the process. It can be either time-controlled or controlled by the in-situ turbidity (or transparency, defined as its complementary) measurement. In the latest case, once the bath has started, the program enters a *wait-while* loop with periodic accesses to the value of the

---

[5] Turbidity is an expression of the optical properties of a liquid that causes light rays to be scattered and absorbed rather than transmitted in straight lines through a sample. Turbidity, which can make a clear liquid to appear cloudy or muddy, is caused by the presence of suspended and dissolved matter [79]. While some suspended material will be heavy enough to settle to the bottom of the container if a liquid sample is left to stand -settleable solids-, very small particles will settle only very slowly or not at all if the sample is regularly agitated or the particles are colloidal.

transmitted intensity (converted in electric current) provided by the Si-detector. Once the transmitted intensity has reached a certain given value (which is programmable), the *while* condition is not longer valid and the program may continue with the following instructions, which usually consists in removing the sample from the bath and dipping it into a rinsing solution.

Since the actual value of the transmitted intensity depends on many factors such as the clearness of the water flowing through the inner part of the water jacket, the ambient light conditions, or even the position at which the laser light crosses the vessel and its geometry, a calibration measurement is needed to account for reproducibility. The calibration step takes place before adding the ammonia to the CBD solution, after the thiourea has completely dissolved in the chemical bath. The current delivered by the optical sensor is recorded during 10 seconds and the average value is obtained and saved as a 100% reference value I_{ref}. As the process is monitored and data is adquired, both the real (I) and the normalized (or relative, $I_{rel} = I/I_{ref}$) value of the trasmitted intensity can be displayed, both as real time and as a 5-point average values.

Another possible configuration consists in locating the sensor at an angle of $90\,^\circ$ with respect to the incident beam. In this way, not the transmitted but the scattered intensity is measured. This configuration is much more sensitive to minor changes (i.e. ambient light changes) than the former one, needing therefore to work either total darkness or with a lock-in amplifier.

Figure 3.5 shows the signals obtained with both configurations[6]. In the transmission configuration the detected intensity decreases as the turbidity of the solution increases. In the scattering configuration, the formation of particles with time contributes to the scattered intensity, which increases with time until saturation is reached. Since both configurations deliver the same information about the process, the transmission configuration, which is the simplest one in terms of necessary equipment, has been chosen for the following investigations.

The measured transparency (or turbidity) curve, gives also information about the different deposition mechanisms taking place at different times throughout the process. At the beginning of the CBD process, a flat plateau at around 100% relative intensity is usually found. Correlated XPS measurements (see chapter 5) show that buffer layer deposition is already taking place at this early stage, although no significant change in the transparency curve is seen, pointing therefore to an ion-by-ion deposition mechanism, by which Zn^{2+} ions released from the decomposition of the zinc tretraamine or the zinc-thiourea complexes react with the S^{2-} ions released from the decomposition of thiourea in aqueous solution following the simple and/or the complex-decomposition mechanism. After a certain time, which depends on the conditions of the chemical bath as it will be shown in the next sections, the transparency of the solution begins to drop due to the formation of particles in the solution. These are responsible for the scattering of the in-

---

[6] Another possible geometry includes the measurement of the backscattered light (detector at $30\,^\circ$ with respect to the incident beam) [80].

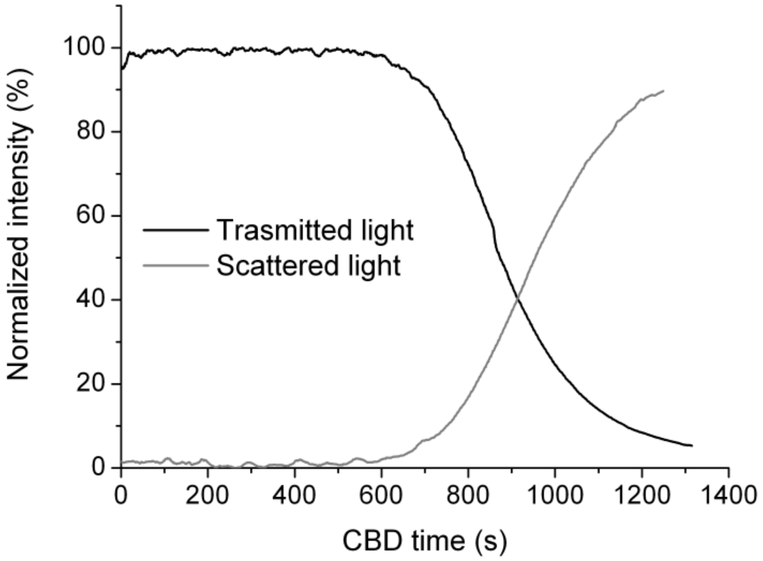

Figure 3.5: Normalized transmitted and scattered signal detected by the optical sensor located at an angle of 180 ° and 90 ° from the laser light source respectively. Signals are obtained from 2 different processes and are, therefore, not complementary.

coming light. These particles are mainly $Zn(OH)_2$, ZnO and ZnS aggregates and the main deposition mechanism at this stage is probably the hydroxide cluster mechanism (simple and/or complex).

The turbidity (or transparency) can be considered a signature of the formation of particles in the solution and it is therefore related to the kinetics of nucleation.

3.4 Kinetic study of nucleation

Studying the process of nucleation in the solution is important in order to understand the deposition of the film onto a substrate. If a chemical bath deposition process for a nominal ZnS layer is qualitatively considered, it can be seen that the kinetics of such a process is dominated by three stages [60]:

- Initiation (often called nucleation or incubation period): the initial step requiring a high activation energy in which reactive centers which catalyze the reaction are formed. During this stage, the chemical equilibra are established in the bath and an initial seed-acting layer of the metal chalcogenide is formed on the substrate.

- Growth: the main phase of the reaction, in which a number of reactive sites give rise to a lower activation energy pathway. This stage defines autocatalysis in a general sense, but the growth of the nuclei in an heterogeneous reaction. The initial monolayer of the semiconductor formed on the substrate acts as a catalytic surface for the condensation of metal and chalcogenide ions and clusters resulting in film growth.

- Termination: stage at which the reagent becomes depleted and the reaction begins to slow down and eventually stops.

The kinetics of typical CBD processes appears to follow a sigmoidal profile similar to those observed for autocatalytic reactions. This sigmoidal profile is also found in the transparency measurements performed during this work (see figure 3.5). In the case of the transparency measurements, the first two stages correlate with the corresponding nucleation processes described earlier (heterogeneous and homogenerous, see section 3.1.1. In the case of the third stage, there is also a saturation of the signal, but this does not necessarily have to be uniquely related to the depletion of the reagent. The influence of an additional signal in form of ambient light and of the geometry of the chemical bath reactor are determinant on this last stage.

The analysis of the transparency of the CBD solution, considered in this case as a signature of the crystallization process during the chemical bath, will be used in this work to compare the effects of the changes in CBD parameters. The light intensity that reaches the detector can be generally expressed in the following way:

$$I(t) \propto I_0 \cdot e^{-\alpha(t) \cdot d} \tag{3.15}$$

where I is the measured intensity, I_0 is the initial intensity, d is the length of the optical path and $\alpha(t)$ depends on the size and density of the particles in the reactor and on the scattering cross section[7]. Therefore, if d is kept constant, a comparative analysis of $\alpha(t)$ is possible from the evaluation of $I(t)/I_0$.

The kinetics of CBD has been usually analyzed by means of the Avrami model [60, 81, 82]. The model proposed by Melvin Avrami [83, 84, 85] describes originally the kinetics of phase transitions and has been applied to a wide range of other problems such as crystallinization of lipids [86] or even cosmology [87]. According to Avrami [83]:

> *"The theory of the kinetics of phase change is developed with the experimentally supported assumptions that the new phase is nucleated by germ nuclei which already exist in the old phase, and whose number can be altered by previous treatment. The density of germ nuclei diminishes through activation of some of them to become growth nuclei for grains of the new phase, and ingestion of others by this growing grains".*

---

[7] Sub band gap illumination is considered. For cluster sizes of approximately 2 nm and a light wavelength of 635 nm, Rayleigh scattering is assumed.

The time evolution of the volume fraction f of transformed volume is predicted from the Avrami model (also called Kolmogorov-Johnson-Mehl-Avrami -KJMA-) as:

$$f(t) = a \cdot (1 - exp(-k \cdot t^n)) \tag{3.16}$$

where a is the value of $f(t)$ as t approaches infinity, k is a time constant related to nucleation and growth rate [88] which depends primarily on the crystallization temperature and n is the Avrami exponent, (also called Kolmogorov exponent), which is a combined function of the time dependence of nucleation and the number of dimensions d in which the growth takes place (film $[d = 2]$ or volume $[d = 3]$ growth). In general n can be expressed as:

$$n = 1 + d + \beta \tag{3.17}$$

where β is related to the nucleation velocity. For the ideal case with an steady state nucleation rate $\beta = 0$ [89]. Sometimes a fourth parameter is added to the Avrami model to account for an induction time t_i (the nucleation start at a time $t_i \neq 0$. The equation then becomes:

$$f(t) = a \cdot (1 - exp(-k \cdot (t - t_i)^n)) \tag{3.18}$$

Applying this model to the turbidity curves (defined as the complement of transparency, in the sense that *turbidity+transparency* = 1) gives reasonable results (R^2 ≥0.99). This can be seen in figure 3.6, where the turbidity monitored during a standard CBD process is fitted to the Avrami model using the additional variable for the induction time, as described in equation (3.18).

The value of the extracted Avrami exponent is $\sim$ 3, which would account for a growth in 2 dimensions, according to equation (3.17) for the case of $\beta = 0$. This could be interpreted as the growing particles covering a volume that projects on an area (that defined by the silicon detector). In the fit, deviations greater than 3% can be found in certain regions. The quality of the model should therefore be improved.

An improved model based on the work by Foubert *et al.* [90] on crystallization of fats has been applied to the transparency measurements during the chemical bath deposition of ZnS buffer layers. The model is written in the form of a differential equation, in contrast to other growth models also applied such as the Avrami and the Gompertz models[8].

The use of a differential equation has various advantages since it is often easier to interpret the equation mechanistically and it also enables the inclusion of minor changes in the equation as a result of acquired knowledge. The algebraic solution, on the other hand, can be easily evaluated by means of any software package capable of analyzing

---

[8] A Gompertz curve or Gompertz function, named after Benjamin Gompertz, is a sigmoid function. It is a type of mathematical model for a time series, where growth is slowest at the start and end of a time period. It is used, among other things, to study the population in a confined space, as birth rates first increase and then slow as resource limits are reached. An analytical expression of a Gompertz curve is $y(t) = ae^{be^{ct}}$, where a is the upper asymptote, $c < 0$ is the growth rate and b is a negative constant.

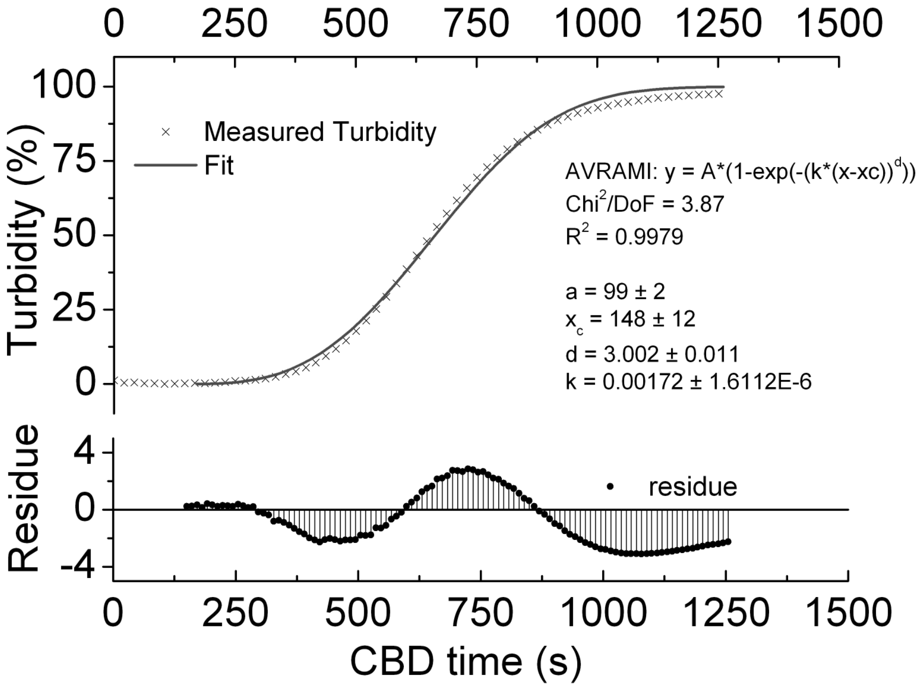

Figure 3.6: Top: Turbidity measured during a standard CBD process together with the fit using the Avrami model. The value of the fitting parameters are also given. Bottom: Residues extracted from the fitting process.

non-linear regression of algebraic equations. Therefore, both the differential equation and its algebraic solution will be presented.

The model is originally built using an approach suggested by Wünderlich [91], who stated that processes such as crystallization can be written in the form of a chemical reaction:

$$\text{A(solution)} \rightleftharpoons \text{B(precipitate)}$$

and that for the thermodynamic and kinetic description of these processes, the same equations as for chemical reactions can be used. Furthermore, he states that all transitions between the solution and the crystalline phase are usually assumed to be first order transitions. In this work, the nucleation process is represented as a combination of a first order forward reaction and a reverse reaction of order n[9] with rate constants k_i [time^{-1}] for each of the chemical reactions.

---

[9] The order of reaction, in chemical kinetics, with respect to a certain reactant, is defined as the power to which its concentration term in the rate equation is raised. For example, given a chemical reaction A + B → C with a rate equation $r \propto [A]^x [B]^y$ the reaction order with respect to A would be x and with respect

The value of the turbidity of the solution $g(t)$ is linked to the value of the transparency $h(t)$ by

$$h(t) = 1 - g(t) \tag{3.19}$$

In contrast to $g(t)$ which increases as the process goes on, $h(t)$ decreases in a sigmoidal way with time.

The dynamics of h can then mathematically be written as:

$$\frac{dh}{dt} = k_n \cdot h^n - k_1 \cdot h \tag{3.20}$$

The detailed nature of the reverse reaction is yet unclear, but might be related to the re-dissolution of some crystals during the process.

One simplification of the model, based on extensive parameter estimation studies [90], is that $k_1 \approx k_n = k$, since the difference between both rate constants is around $1 \cdot 10^{-5}$. This results in:

$$\frac{dh}{dt} = k \cdot (h^n - h) \tag{3.21}$$

To calculate the values of $h(t)$ according to Eq.(3.21), the initial value of h, $h(0)$ needs to be specified. $h(0) = 1 - g(0)$ where $g(0)$ is related to the initial presence of potential nuclei. The parameters of this model are therefore three: $h(0)$, k and n and the influence of the parameters on the model is shown in figure 3.7.

Figure 3.7 A) shows the influence of the reaction rate k (s^{-1}) on $h(t)$ (for $h(0)$=0.9999 and n=2). The rate of crystallization increases with k. The higher the value of k is, the sooner and faster the crystallization process takes place. In figure 3.7 B), the curves for different values of k are displayed on a shifted time-scale so that for all curves, the time t_a for which $h(t_a)$=0.5 is the same. In figure 3.7 C) the influence of $h(0)$ on the model is shown [for k=0.01 s^{-1} and n=2]. $h(0)$ is clearly related to the induction time, qualitatively defined as the time for which the decrease in the transparency is detectable. The closer the value is to 1, the longer it takes to form detectable particles that reduce the value of the transparency. If k and n are kept constant, the changes induced by $h(0)$ are just a shift in the time scale, as it can be seen in figure 3.7 D). The influence of the parameter n on the model is shown in figure 3.7 E). n has also an influence on the time needed to reach a detectable amount of particles. The higher the value of n (i.e. the order of the reverse reaction), the faster the term $k \cdot h^n$ will become negligible and the faster a relevant amount of particles will be formed. Additionally, n is linked to the asymmetry of the curve. When $n = 2$ the sigmoid is perfectly symmetric. If n is larger than 2, the beginning of the crystallization process is faster than the end. The more n exceeds 2, the larger the difference between the rates of the beginning and the end stages. On the

---

to B would be y, the total reaction order would be $x + y$. It is not necessary that the order of a reaction is a whole number - zero and fractional values of order are possible.

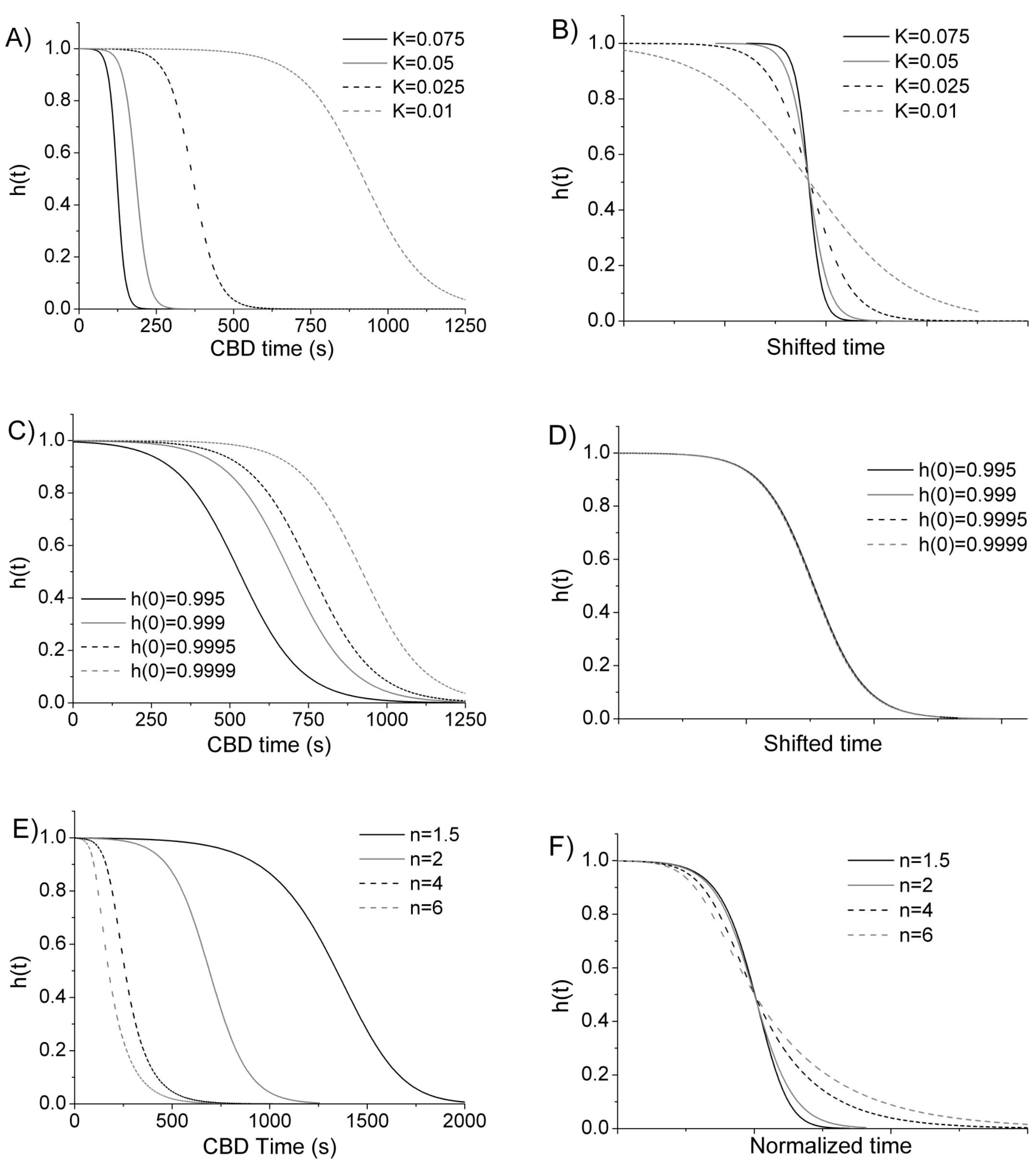

Figure 3.7: A), C) and E): influence of the fitting parameters k (reaction rate), n (order of reaction) and $h(0)$ on $h(t)$. B) and D): representation of A) and C) with shifted times. F): representation of E) with normalized time. For more details see text.

other hand, if the value is smaller than 2, the beginning of the process is slower than the end. The influence of the parameter n on the asymmetry of the curve is seen in figure 3.7 F), where the time-axis has been normalized in such a way that all curves intersect at a transparency value of 0.5.

To simplify the estimation of the parameters, the differential equation can be converted to its algebraic solution. To solve equation (3.21), it can be rewritten as:

$$h^{-n}\frac{dh}{dt} + k \cdot h^{1-n} - k = 0 \tag{3.22}$$

If h^{1-n} is substituted by y, the following first order differential equation is obtained:

$$\frac{1}{1-n}\frac{dy}{dt} + k \cdot y = k \tag{3.23}$$

The solution of which is:

$$y(t) = 1 + (y(0) - 1) \cdot e^{-(1-n)\cdot k \cdot t} \tag{3.24}$$

Now the original variable h has to be re-substituted:

$$h(t) = \left[1 + \left(h(0)^{1-n} - 1\right) \cdot e^{-(1-n)\cdot k \cdot t}\right]^{\frac{1}{1-n}} \tag{3.25}$$

This will be the equation used to fit the transparency curves and to evaluate the fitting parameters $h(0)$, k and n. As an example of a fit using the proposed model, figure 3.8 shows the transparency curve obtained monitoring a standard CBD process together with the fitted curve and the respective residues. In this case, the fit is more accurate that the one obtained using the Avrami model (see figure 3.6), as it can be seen by comparing the R^2 values (0.9999 and 0.9979 respectively), and the residues (deviations $\leq 1.1\%$).

In the next section, the transparency curves obtained by monitoring the CBD process in situ will be compared by fitting the curves using the model proposed above (equation (3.25)) and by extracting the characteristic parameters of the model ($h(0)$, n and k) from the fitted curves. This will help to clarify the role of the different CBD parameters on the particle formation rate (i.e. on the transparecy or the transmitted intensity).

3.4.1 Influence of CBD parameters on the transparency

Varying the chemical and/or physical conditions of the chemical bath has a direct impact on the growth mechanisms and therefore on the behaviour of the transparency curves. A systematic study aiming to clarify the influence of the different CBD conditions on the particle formation has been carried out by measuring, fitting and comparing the transparency curves of CBD processes. The reference bath consisted in a standard 200 ml CBD, with the technical and chemical specifications described in section 3.2 in page 26. In each set of experiments one of the variables was varied while all remaining variables were kept constant. Transparency graphs were recorded using the optical set up describe above (see figure 3.4). The obtained graphs were analyzed in terms of $h(0)$ and k and n.

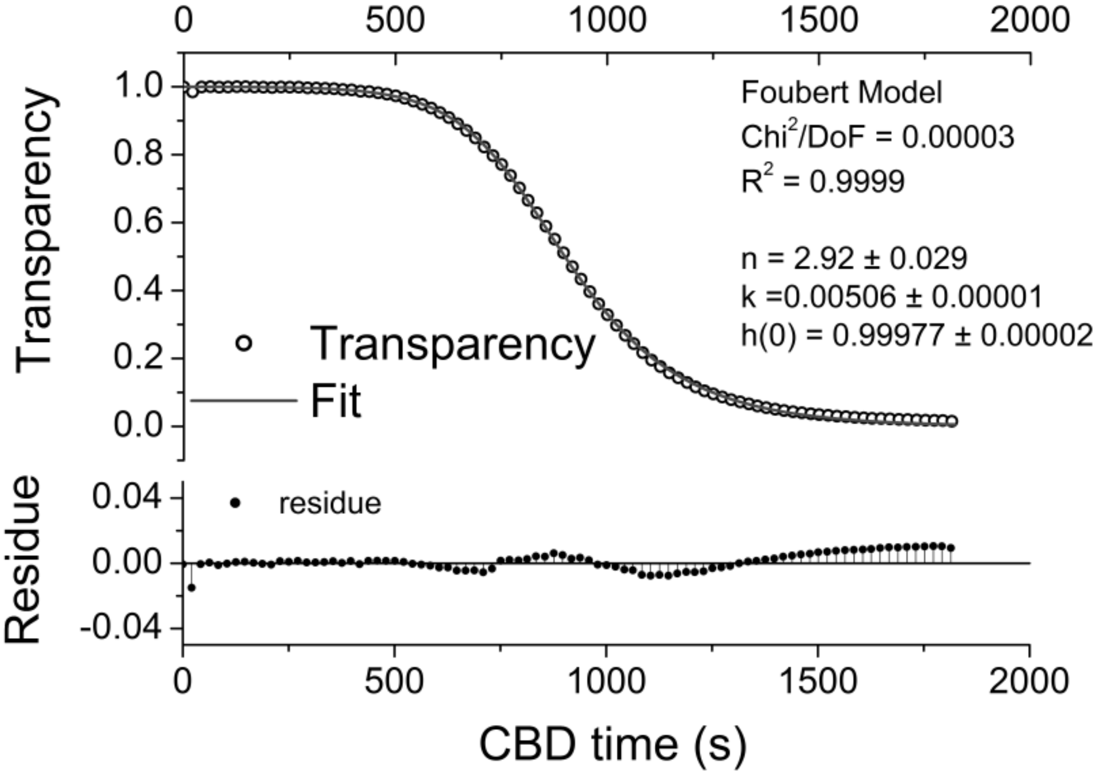

Figure 3.8: Top: Transparency measured during a standard CBD process together with the fit using the proposed model. The value of the fitting parameters n, k and $h(0)$ are also given. Bottom: Residues extracted from the fitting process. Deviations are kept below 1.1 % during the whole process.

Bath control temperature

This set of experiments was carried out setting the bath temperature controller at different temperatures while keeping all other conditions constant. The actual value of the temperature inside the bath does not reach the control temperature due to the thermal losses in the water circuit. The temperature of the chemical bath was controlled every 60 seconds.

The dissociation of the zinc-complexes (with ammonia and with thiourea) and of the anion depends greatly on the temperature [92]. At higher temperatures, the decomposition of thiourea will be faster setting more S^{2-} ions free, according to reactions (3.1) and (3.2). Additionally, the zinc-complex dissociation is greater and gives a higher concentrations of free Zn^{2+} in the solution, which in turn results in higher deposition rates or, in other words, and for a constant buffer layer thickness, in shorter deposition times. Figure 3.9 shows the transparency (normalized transmission intensity) graphs and temperature measured for different bath control temperatures. The values of the fitting parameters as well as the value of R^2 (used as a verification of the quality of the fit) are listed in table 3.1.

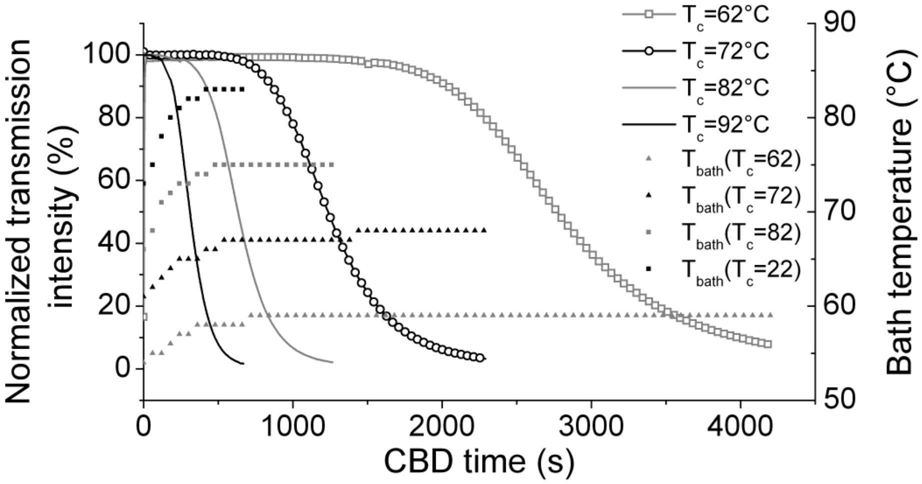

Figure 3.9: Normalized transmission intensity (transparency) and temperatures measured in the chemical bath for different control temperatures ranging from 62 °C to 92 °C. The standard CBD is carried out using a control temperature of 82 °C (grey line).

A raise of the temperature during the first minutes of the process is clearly seen on the graphs. This is due to fact that after the addition of ammonia (which is at room temperature), the temperature in the bath decrases before it starts increasing again.

The overall reaction time is reduced with increasing temperatures. Additionally, the reaction rate is faster for higher temperatures, as deduced from the parameter k. Higher temperatures accelerate the thermal decomposition of the Zn-thiourea and the Zn-ammonia complexes, setting more Zn^{2+} free. It also increases the rate of ammonia evaporation, which in turns lowers the pH of the solution, favouring the formation of $Zn(OH)_2$ clusters, thus decreasing the transparency of the chemical solution. The reduction of $h(0)$ with increasing temperatures indicates the earlier formation of particles when

Table 3.1: Parameters obtained by fitting the normalized transparency curves measured at different control temperatures. k -rate constant- is given in s^{-1} while $h(0)$ and n -order of reaction- are dimensionless. Additionally the value of R^2 is given as a verification of the quality of the fit.

Cont. Temp.	$h(0)$	n	k [s^{-1}]	R^2
62 °C	0.99997 $\pm 1 \cdot 10^{-5}$	3.9 ±0.1	$1.4 \cdot 10^{-3} \pm 10^{-4}$	0.99991
72 °C	0.99981 $\pm 1 \cdot 10^{-5}$	3.6 ±0.1	$2.9 \cdot 10^{-3} \pm 10^{-4}$	0.99993
82 °C	0.99932 $\pm 1 \cdot 10^{-5}$	3.1 ±0.1	$5.9 \cdot 10^{-3} \pm 10^{-4}$	0.99992
92 °C	0.99812 $\pm 1 \cdot 10^{-5}$	3.1 ±0.1	$1.0 \cdot 10^{-2} \pm 10^{-4}$	0.99992

the temperature is higher.

This qualitative behaviour has also been observed by Yamaguchi *et al.* [93] on ZnS nucleation in chemical baths containing zinc acetate and thioacetamine. More precipitate was collected from the solution with higher deposition temperature (and for identical deposition time), thus indicating a larger homogeneous precipitation (see 3.1.1).

Regarding the growth of the layer on a substrate, Chaparro *et al.* [78] showed for chemical bath deposited Zn(Se,O) that increasing the temperature of the solution (with all other variables kept constant) reduces the induction time (i.e. the time at which crystallization begins) and increases the growth rate, which would be translated in the model as a decreasing value of $h(0)$ and an increasing value of k for increasing process temperatures. This is corroborated by the extracted fitting parameters.

Concentration of precursors

For this experiment, different concentrations of precursors were added to the chemical bath, keeping all other parameters constant. In all cases, the [$ZnSO_4$]:[TU] ratio was kept 1:4 as explained in section 3.2.

Increasing the concentration of the precursors accelerates the reaction and reduces the deposition time. If the concentration of zinc is increased, more ammonia is needed to avoid the formation of $Zn(OH)_2$ and the excess of ammonia added is less than in the standard case. This excess of ammonia evaporates sooner and the homogeneous precipitation starts earlier. The growth of the particles in the bath is faster as it can be deduced from the shape of the transparency curves shown in figure 3.10 and from the analysis of the corresponding fitting parameters, which are in summarized in table 3.2. In analogy to the case of the different control temperatures, increasing the concentration of the precursors reduces the length of the initial plateau and accelerates the particle formation rate, modeled primarily by $h(0)$ and k respectively.

Table 3.2: Parameters obtained by fitting the normalized transparency curves obtained with different concentration of precursors, given in the table (eel. conc) as a fraction of the standard concentration of zinc salt and thiourea (0.15 M and 0.6 M respectively). k -reaction rate- is given in s^{-1} while $h(0)$ and n -order of reaction- are dimensionless. Additionally the value of R^2 is given as a verification of the quality of the fit.

Rel. conc.	$h(0)$	n	k [s^{-1}]	R^2
0.5	$0.99983 \pm 1 \cdot 10^{-5}$	2.8 ± 0.1	$2.7 \cdot 10^{-3} \pm 10^{-4}$	0.99979
1	$0.99957 \pm 1 \cdot 10^{-5}$	3.3 ± 0.1	$4.7 \cdot 10^{-3} \pm 10^{-4}$	0.99978
1.5	$0.99766 \pm 1 \cdot 10^{-5}$	3.5 ± 0.1	$6.7 \cdot 10^{-3} \pm 10^{-4}$	0.99987

As in the example with varying control temperatures, this behaviour was also observed by Yamaguchi *et al.* [93]; more precipitate was collected from baths containing a

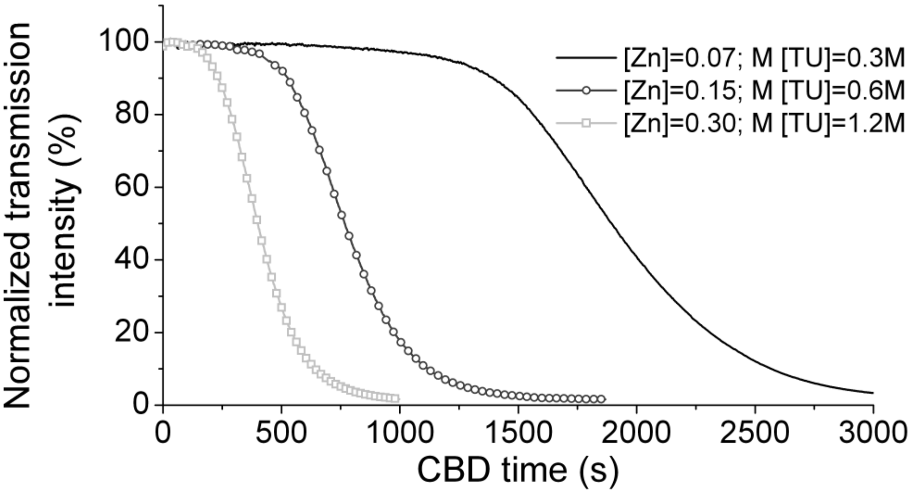

Figure 3.10: Normalized transmission intensity (transparency) and temperature measurements obtained by monitoring chemical baths with different precursor's concentration. The standard process is carried out with [$ZnSO_4$]=0.15M and [TU]=0.6M (grey circles).

higher concentration of precursors (here again for the same deposition time).

According to the theory of the CBD described earlier, it is the release of S^{2-} by the hydrolysis of thiourea the process that limits the formation of ZnS. This can be seen by monitoring different CBD processes with different concentration of thiourea, while all other variables (temperature, concentration of Zn^{2+}, concentration of ammonia, etc.) are kept constant.

The transparency curves obtained by changing the concentration of thiourea are shown in figure 3.11 and the fitting parameters obtained from the curves are summarized in table 3.3.

Table 3.3: Parameters obtained by fitting the normalized transparency curves obtained with different concentration of thiourea [TU]. k -reaction rate- is given in s^{-1} while $h(0)$ and n -order of reaction- are dimensionless. Additionally the value of R^2 is given as a verification of the quality of the fit.

[TU]	$h(0)$	n	k [s^{-1}]	R^2
0.3 M	$1 \pm 1 \cdot 10^{-6}$	2.8 ± 0.1	$3.9 \cdot 10^{-3} \pm 10^{-4}$	0.99994
0.45 M	$0.99999 \pm 1 \cdot 10^{-5}$	2.9 ± 0.1	$4.4 \cdot 10^{-3} \pm 10^{-4}$	0.99991
0.6 M	$0.99977 \pm 1 \cdot 10^{-5}$	2.9 ± 0.1	$5.1 \cdot 10^{-3} \pm 10^{-4}$	0.99985
0.9 M	$0.99764 \pm 1 \cdot 10^{-5}$	3.5 ± 0.1	$6.7 \cdot 10^{-3} \pm 10^{-4}$	0.99987

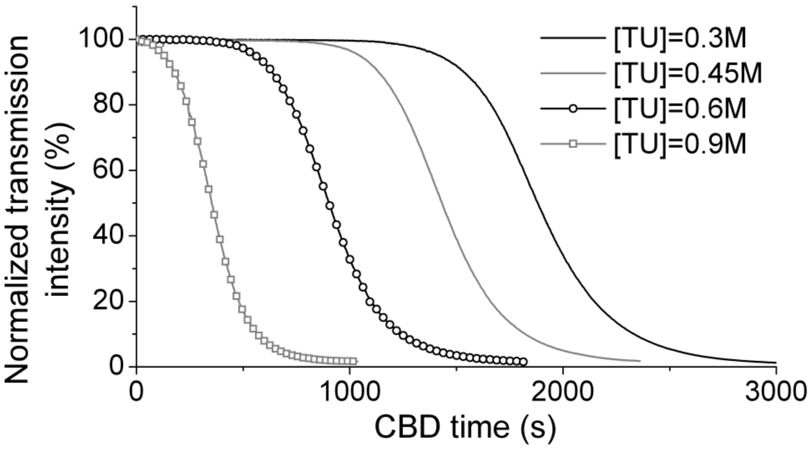

Figure 3.11: Normalized transmission intensity (transparency) graphs obtained monitoring CBD processes with different concentrations of thiourea.

When the concentration of thiourea is increased, its hydrolysis is accelerated, S^{2-} ions are released sooner, and ZnS particles are formed earlier, as it can be seen in the graph (figure 3.11). The decrease of the values of $h(0)$ with time is a clear indication that the formation of particles occur earlier when the ratio [TU]/[Zn salt] is increased. A faster reaction when the concentration of thiourea is increased is also confirmed by the higher values of k. Both of these factors reduce the overall process time.

Zinc-thiourea reaction time

One of the chemical bath parameters that has been also a subject of study is the waiting time between the addition of the thiourea and the incorporation of ammonia. During this time, zinc sulphate and thiourea react to form ZTS and other zinc thiourea complexes. In the standard case this time is set to 3 minutes. After the addition of ammonia, the free zinc ions that have not reacted with thiourea, react with ammonia to form zinc tetraamine among other zinc-ammonia complexes (see equation (3.13)). This zinc-thiourea reaction time controls therefore the ratio between zinc-thiourea complexes and zinc-ammonia complexes in the solution.

Figure 3.12 shows the transparency curves and the measured temperature for four different CBD processes. The respective zinc thiourea reaction times between (time between the addition of thiourea and ammonia) are 0 (thiourea and ammonia added at the same time), 1.5 minutes, 3 minutes (standard process) and 30 minutes. The corresponding fitting parameters are summarized in table 3.4

From the curves and the corresponding fitting parameters it is clear that the presence of the zinc thiourea complex reduces the time needed for the particles to stabilize

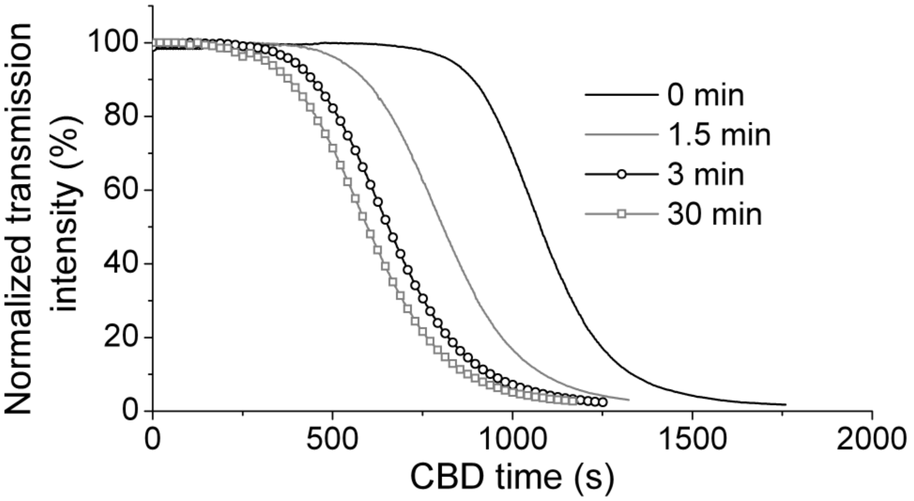

Figure 3.12: Normalized transmission intensity (transparency) and measured process temperatures recorded for different zinc-thiourea reaction times, defined as the time between the addition of thiourea and ammonia. The standard process is represented by the black circles.

Table 3.4: Parameters obtained by fitting the normalized transparency curves obtained with different concentration of thiourea (given in the table as a fraction of the standard concentration of thiourea (0.6 M). k -reaction rate- is given in s^{-1} while $h(0)$ and n -order of reaction- are dimensionless. Additionally the value of R^2 is given as a verification of the quality of the fit.

Reaction time	$h(0)$	n	k [s^{-1}]	R^2
0 min	$1 \pm 1 \cdot 10^{-6}$	3.1 ± 0.1	$6.6 \cdot 10^{-3} \pm 10^{-4}$	0.99969
1.5 min	$0.99988 \pm 1 \cdot 10^{-5}$	2.9 ± 0.1	$6.3 \cdot 10^{-3} \pm 10^{-4}$	0.99994
3 min	$0.99955 \pm 1 \cdot 10^{-5}$	3.1 ± 0.1	$6.1 \cdot 10^{-3} \pm 10^{-4}$	0.99992
30 min	$0.99846 \pm 1 \cdot 10^{-5}$	2.9 ± 0.1	$6.2 \cdot 10^{-3} \pm 10^{-4}$	0.99989

in the solution. The thermal decomposition of the zinc-thiourea complexes is therefore dominant when compared to the decomposition of the zinc-ammonia complexes. The zinc-thiourea complex starts to form as soon as thiourea is added to the solution and the reaction rate of the crystallinization process not substantially influenced by the waiting time, at least for times above 90 seconds. This can be seen in table 3.4, where the parameter $h(0)$ and k are presented. It can be observed that for 0 minutes the particle formation begins rather late, indicating that the thermal decomposition of the zinc-ammonia complexes is slower than that of zinc-thiourea complexes. Increasing the waiting time allows the formation of zinc-thiourea complexes and a reduction of $h(0)$ due to the faster release of Zn^{2+} ions. The complexation of zinc with thiourea is a rather fast reaction. Waiting 30 minutes has hardly any influence on the transparency measurements when compared to the standard curve obtained with a waiting time of three minutes. On the other hand, the crystallization rate k and n stay approximately constant. This means that increasing the waiting time merely shifts the curve to shorter times, affecting only the values of $h(0)$. The bath is therefore optimized to be as short as possible, finding a compromise between the waiting time and the deposition time. Furthermore, the fact that increasing the waiting time has hardly any influence on the transparency curves enables the preparation of the zinc-thiourea solution in advance without fearing any impact on the deposition of the buffer layer. This may be of significant importance when transferring the CBD process of Zn(S,O) buffer layers to an industrial pilot line (see discussion in chapter 8 for more details).

Concentration of ammonia

Following the description of the CBD stated in section 3.2, it is the evaporation of ammonia the fact that triggers the homogeneous precipitation of $Zn(OH)_2$ in the chemical solution. The higher the ammonia concentration is, the longer it will take to evaporate enough ammonia in order to start with the formation of $Zn(OH)_2$. In general, if the concentration of OH^- in the solution is higher, the metal ion concentration [Zn^{2+}] will be lower and thus the reaction will be slower [92]. In figure 3.13 transparency curves obtained using the standard process, and processes with reduced ammonia concentrations are shown, while the obtained parameters are summarized in table 3.5. It can be seen that the reduction of [NH_3] reduces the overall process time. It is also obvious that the first stage at which the transparency stays constant at around 100% of the inicial value is not present when working with low ammonia concentrations. The homogeneous nucleation takes place already from the beginning of the deposition process. The behaviour of the curve measured under standard CBD conditions during the first seconds of the process is an artifact explained by the formation of bubbles in the walls of the bath reactor and is not correlated to any feature of the deposition process.

Table 3.5: Parameters obtained by fitting the normalized transparency curves obtained with different concentration of ammonia (given in the table as a fraction of the standard concentration (4 M). k -reaction rate- is given in s^{-1} while $h(0)$ and n -order of reaction- are dimensionless. Additionally the value of R^2 is given as a verification of the quality of the fit.

Rel. [NH_3]	$h(0)$	n	k [s^{-1}]	R^2
1	$0.99997 \pm 1 \cdot 10^{-6}$	3.6 ± 0.1	$3.9 \cdot 10^{-3} \pm 10^{-4}$	0.99969
0.5	$0.99476 \pm 1 \cdot 10^{-5}$	1.3 ± 0.1	$2.1 \cdot 10^{-2} \pm 10^{-4}$	0.99973
0.42	$0.98431 \pm 1 \cdot 10^{-5}$	2.4 ± 0.1	$9.7 \cdot 10^{-3} \pm 10^{-4}$	0.99977
0.33	$0.99616 \pm 1 \cdot 10^{-5}$	7.8 ± 0.1	$1.6 \cdot 10^{-2} \pm 10^{-4}$	0.99947

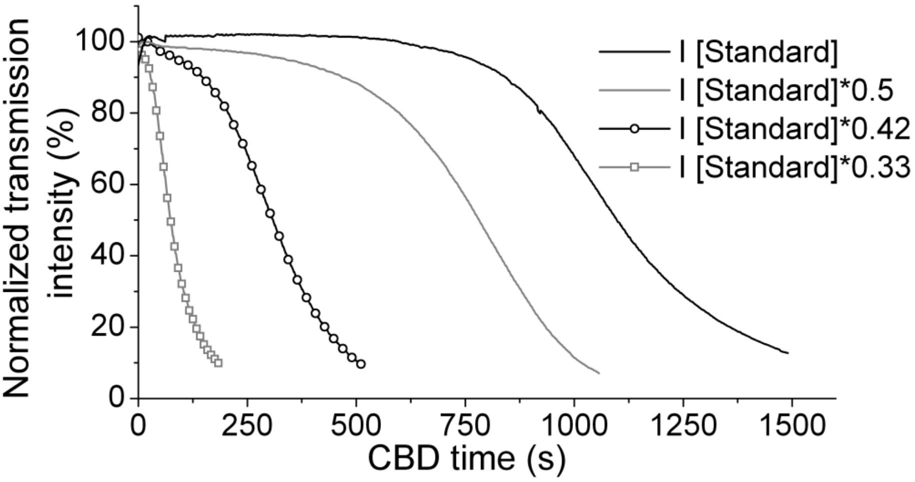

Figure 3.13: Normalized transmission intensity (transparency) and temperature measurements for different concentrations of ammonia, expressed as a fraction of the standard concentration (4 M).

Previous studies on ZnS layers deposited on HF-etched silicon substrates using zinc carbonate as a source of zinc ions, and different concentrations of ammonia, thiourea and hydrazine (N_2H_4) [94] showed that there is a strong influence of the pH value (determined mainly by the concentration of ammonia) on the composition of the deposited films and that the ratio between ZnS and Zn-oxygen compounds can be controlled by regulating the pH value, which is in turn achieved by changing the concentration of ammonia.

3.4.2 Particle formation

In the introduction of CBD (section 3.1.1, page 21), the basics of the formation of particles in the chemical bath were described. While heterogeneous nucleation starts mainly due to the catalytic effect of the substrate, the homogeneous precipitation begins when the formed embryos reach the critical radius and have a 50% chance of not redissolving (as explained in section 3.1.1). It would be logical to expect that if some ZnS and/or $Zn(OH)_2$ particles are introduced in the bath, the formation of aggregates will take place in a shorter time. The released Zn^{2+} and S^{2-} ions will be adsorbed at the already stable particles and precipitation will occur sooner. For the experimental observation of this phenomenom, a standard CBD process was performed and the remaining solution was filtered, centrifuged and washed in ethanol in order to obtain the remaining precipitate. This precipitate was left to dry at 50 °C for some hours until a dried powder was obtained. 10 mg of this powder were mixed with 5 ml water and were added to a second standard CBD process one minute after having added the ammonia. An schematic diagram of the steps followed for this experiement is shown in figure 3.14 a). The results of the optical monitoring of both

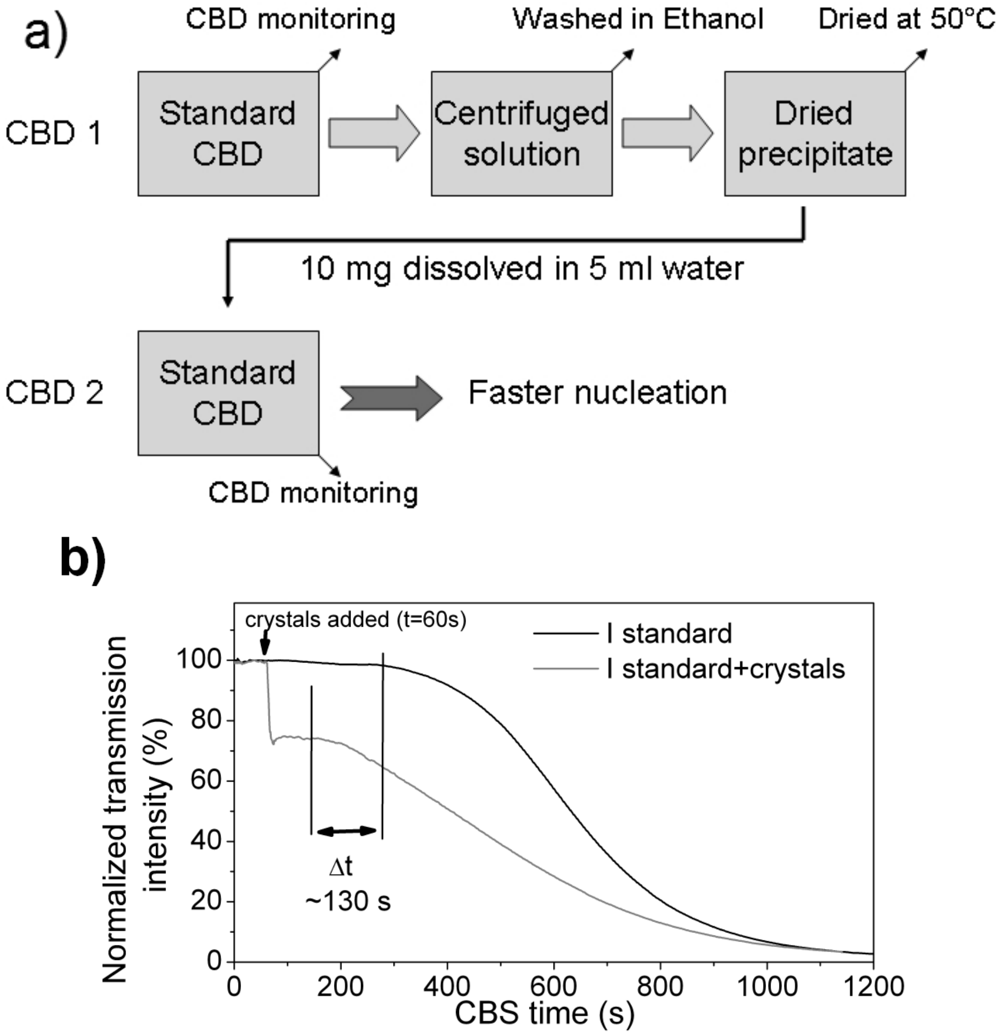

Figure 3.14: a) schematic diagram showing the steps followed to obtain the Zn-containing precipitate and how it was used in the second CBD process. b) normalized transmission intensity (transparency) measurements of a standard CBD process and of a similar process including the addition of crystals that act as growth seeds. In the figure it is indicated the point at which the crystals were added, as well as the difference between the start of the homogeneous precipitation for both solutions.

chemical baths can be found in figure 3.14 b). After adding the 10 mg of the precipitate, the transparency of the solution drops to 75% and soon thereafter begins to decrease. This decrease of the transparency occurs earlier in the case of the second solution, since the already formed Zn-containing crystals from the precipitate obtained from the first bath act as seeds for the growth of larger particles in the second. In this experiment, the homogeneous precipitation occured approximately 2 minutes earlier than in the standard CBD used as a reference (60% faster).

3.4.3 Use of additives

In the deposition of nominal ZnS layer by chemical bath at basic pH, in processes in which the zinc salt is firstly mixed with the ammonia and then the thiourea solution is added, it is common to see an improvement of the deposition if a second ligand is present [95]. Many groups have reported the use of a second ligand in the CBD of ZnS, being hydrazine (N_2H_4) [66, 67] and triethanolamine (TEA)[96] two of the most popular choices. Lincot and Ortega-Borges [97] reported that the use of ammonia and thiourea without hydrazine results in films that are neither homogeneous nor adherent. In a related observation, Doña and Herrero [77] suggested that although the presence of hydrazine is not strictly necessary for the growth of ZnS layer, it indeed improved the homogeneity, the specularity and the growth rate of the films. Increasing the hydrazine concentration from 1M to 3M increased in turn the growth rate from 0.6 nm/min to 1.8 nm/min approximately. A later work by Neve et al. [94] suggested that the presence of hydrazine in the solution is essential for film growth to take place. Layers grown without hydrazine showed a reduced area density of zinc (0.7 ± 0.1 Zn[at/cm^2]x10^{15}), 20-fold lower than for the corresponding experiment with hydrazine.

A possible reason for this effect is that the stability of the zinc-hydrazine complex $Zn(NH_2\text{-}NH_2)_3^{2+}$ is lower when compared to the zinc-amine complex $Zn(NH_3)_4^{2+}$. Additionally the presence of hydrazine accelerates the hydrolysis of thiourea, supplying necessary OH^- ions for the S^{2-} ion formation, which in turn form the ZnS film [98, 95, 99].

In the case under study, the main difference is that the zinc salt is not completely reacting with ammonia, as in the previously cited examples [98, 95, 99]. The main ligand in this case is thiourea, and it is the zinc-thiourea and not the zinc-ammonia complex the one that plays the most important role. X-ray absorption fine structure (XAFS) experiments have shown the presence of zinc-thiourea complexes as soon as both chemicals are mixed [100] even at room temperature. The spectrum does not significantly change when ammonia is added. This is supported by the transparency measurements shown in figure 3.12, where the waiting time between the addition of thiourea and ammonia was varied, and thus the ratio Zn-amine/Zn-thiourea. The larger the presence of Zn-thiourea complexes is, the faster the reaction takes place. This is a further advantage of the chemical bath deposition process for ZnS layer patented at the Helmholtz-Zentrum Berlin, since it avoids the use of the toxic reactant hydrazine while maintaining an acceptable growth rate and homogeneity of the deposited layer.

Table 3.6 shows the deposition parameters of the alternative chemical bath processes used for the preparation of Zn(S,O) layers described in this work, together with the deposition parameters of chemical baths developed earlier which include either hydrazine or TEA [101]*. The conditions for the deposition of CdS, which is the standard buffer layer in commercial devices, are also included for comparison.

It is true, however, that the deposition times of Zn(S,O) buffer layers takes usually longer than that of CdS (see table 3.6), which is deposited in less than 10 minutes [102]. In order to further increase the deposition rate of the Zn(S,O) layer during the CBD, the

Table 3.6: Conditions of the various CBD processes used for the deposition of Zn(S,O) buffer layers on chalcopyrite based thin film solar cells. The conditions for the deposition of CdS are also included for comparison.

Process Description Material	No additive Zn(S,O)	hydrazine Zn(S,O)	TEA Zn(S,O)	Standard CdS
Zinc sulfate·$7H_2O$	0.15 M	0.04 M	0.055 M	/
Cadmium sulfate	/	/	/	0.012 M
Ammonia	4.0 M	1.33 M	1.33 M	1.1 M
Hydrazine hydrate 25%	/	1.5 M	/	/
TEA	/	/	$\sim$ 3 ml	/
Thiourea	0.6 M	0.1 M	0.1 M	0.22 M
Deposition time	15-20 min	15 min	20 min	7 min
Bath temperature	$73 - 78\,°C$	$73\,°C$	$73\,°C$	$60\,°C$
References	This work	[66, 67]	[96]	

inclusion of additives (preferably non toxic and low cost) can be a reasonable strategy, as long as the efficiencies are maintained. Since both hydrazine and TEA do not fulfill these requirements, another compound should be found in order to reduce the deposition rate.

Figure 3.15 (left) shows the transparency graphs obtained performing the standard CBD described in this section and the ones obtained with the inclusion of H_2O_2 at very low concentration, ranging from 0.09 % to 0.48% of the total volume of the chemical solution [103]*. The corresponding values of the fitting parameters are shown in table 3.7. The use of this additive, even at extremely low concentrations, has a great impact on the CBD. On one hand, the formation of detectable particles in the solution is triggered much sooner than in the standard case (black line, figure 3.15). On the other, this formation of particles is much faster than in the standard case, as it can be seen from the values of k obtained from the measured curves (table 3.7). The reduction of the particle formation rate is enormous when 0.09% of additive is included compared to the standard CBD (with no additive), but does not decrease significantly if this concentration is increased.

The concentration of H_2O_2 also regulates to some extend the duration of the first plateau, which does not completely disappear, as it happens when, for example, the concentration of ammonia is reduced (see figure 3.13 in page 46). The duration of the initial plateau is however much shorter than in the case of the standard CBD without additive. One way of manipulating the chemical bath to obtain longer plateaus would be as easy as to delay the inclusion of the additive to the chemical bath. In this case one has to bear in mind that for temperatues above 75 °C there is a risk of causing a so-called boiling liquid expanding vapour explosion (BLEVE) when pouring the additive.

The qualitative effects of the inclusion of H_2O_2 in the chemical bath are analytically corroborated by the decrease of $h(0)$ and the increase of the reaction rate k for increasing additive concentration, as shown in table 3.7.

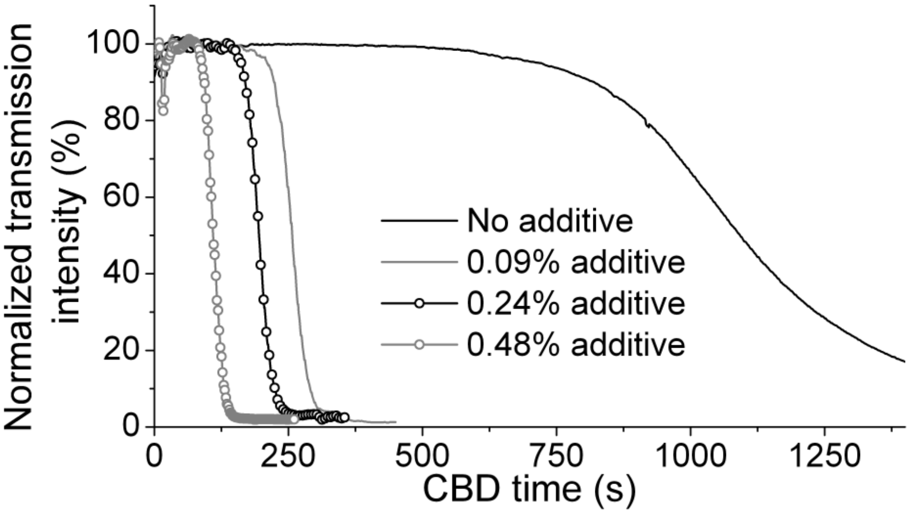

Figure 3.15: Transparency graphs obtained monitoring a standard CBD and three processes containing a very low concentrations of additive, ranging from 0.09% to 0.48% of the total volume of the solution.

Table 3.7: Parameters obtained by fitting the normalized transparency curves obtained with different concentration of additive (given in the table as a percentage of the total volume of the solution (200 ml). k -reaction rate- is given in s^{-1} while $h(0)$ and n -order of reaction- are dimensionless. Additionally the value of R^2 is given as a verification of the quality of the fit.

[Additive]	$h(0)$	n	k [s^{-1}]	R^2
0 %	$1 \pm 1 \cdot 10^{-6}$	3.5 ± 0.1	$3.9 \cdot 10^{-3} \pm 10^{-4}$	0.99960
0.09 %	$0.99988 \pm 1 \cdot 10^{-5}$	2.1 ± 0.1	$6.2 \cdot 10^{-3} \pm 10^{-4}$	0.99919
0.24 %	$0.99955 \pm 1 \cdot 10^{-5}$	2.8 ± 0.1	$6.5 \cdot 10^{-3} \pm 10^{-4}$	0.99901
0.48 %	$0.99846 \pm 1 \cdot 10^{-5}$	2.9 ± 0.1	$7.7 \cdot 10^{-3} \pm 10^{-4}$	0.99905

Experiments performed in the laboratory have identified a reaction between thiourea and the H_2O_2. This may accelerate the hydrolysis of thiourea, setting more S^{2-} ions free and thus increasing the formation rate of ZnS. If this increase of the ZnS production rate is translated into an enhanced growth rate on the absorber and what impact the use of the additive has on the buffer layer composition are questions that will be addressed in the following chapters.

3.5 Summary

The basics of chemical bath deposition process have been presented and applied to explain the deposition of a nominal ZnS film. The use of an optical set up which detects the light intensity transmitted through the chemical solution has been described. This normalized transmission intensity (related to the transparency -or the turbidity- of the solution) has been used to monitor the deposition process as a function of the parameters that control the CBD, namely temperature, concentration of precursors and reaction times. Two different stages can be distinguished. In the first one, the chemical solution stays clear. During this stage, the main growth mechanims (if any) is supposed to be based on the ion-by-ion process. In the second stage, detectable particles are formed. These particles scatter the incoming light thus reducing the detected light intensity (in the case of the configuration used). According to the theory of chemical bath deposition, these particles are $Zn(OH)_2$ and/or ZnS aggregates. The dominant growth mechanism in this stage is supposed to be the cluster mechanism, although the formed crystallites may still grow by ion-by-ion processes. Furthermore, the use of an additive has been tested in order to increase the reaction rate in the solution. The use of H_2O_2 is a feasible strategy to increase the reaction rate without the use of any toxic material. Whether this increase in the particle's formation rate is translated in a larger deposition rate on the absorber will be clarified in the future chapters.

Chapter 4

Growth and structure studied by electron microscopy

Once the kinetics of particle formation in the solution has been studied by means of the optical measurements described in section 3.3, it is now time to investigate if there is a correlation between the formation of particles as a precipitate in the chemical solution and the film deposited on a Cu-chalcopyrite absorber ($\mathrm{CuInS_2}$ and $\mathrm{Cu(In,Ga)(S,Se)_2}$) which will constitute the buffer layer in a photovoltaic device (see figure 2.1). The growth of the deposited Zn(S,O) films and their thickness-resolved composition are studied in this chapter by means of scanning- and transmission- electron microscopy (SEM and TEM respectively) for both the standard CBD recipe (as described in section 3.2) and the modified CBD including the additive (see section 3.4.3). Additionally, the precipitate (particles in the solution that are not deposited on the substrate) formed during the chemical bath deposition using both recipes is collected and analyzed and the results are compared to those obtained for the deposited films, in order to clarify the growth mechanisms during the deposition.

4.1 Theoretical aspects of the electron microscope

The main goal of the electron microscope is to overcome the limitations imposed to the image resolution in optical microscopy, which uses visible light as probe. The origin of the electron microscope can be tracked back to the de Broglie's statement on the wave-particle duality [104]. This means that the principles of optical microscopy can be applied to entities traditionally conceived as particles, such as electrons. As the wavelength associated to a particle decreases with increasing velocity, it is clear that accelerated electrons are a convenient probe for replacing visible light in high resolution microscopy. For this case, the conventional optical lenses used in optical microscopes have to be replaced by their electromagnetic equivalents, which focus the electron beam by means of electromagnetic fields. From the expression of the kinetic energy E_{kin} of a particle with momentum

$\mathbf{p}$ as a function of the associated wavelength ($\lambda = h/p$), including relativistic corrections:

$$E_{kin} = \frac{p^2}{2m_e} = \frac{4\pi\hbar^2}{2m_e} \cdot \frac{1}{\lambda^2} \tag{4.1}$$

from where it follows that, in principle, wavelengths below 0.005 nm can be obtained with electrons accelerated by 60 kV.

The first electron microscope was based on the pioneering work of Ruska in electromagnetic lenses [105].

4.1.1 Scanning electron microscope

Scanning electron microscopes (SEM) are based on the detection of secondary electrons, which are those inner-shell electrons ejected from the interaction volume[1] when the impinging electrons ionize the sample atom. The image is created by scanning the focused electron beam in a raster pattern across the area of the sample. Secondary electrons are then collected by a detector, generating a signal which is displayed in a monitor. The most common imaging mode collects low-energy (<50 eV) secondary electrons that are ejected from the specimen atoms by inelastic scattering interactions with beam electrons. Due to their low energy, these electrons originate within a few nanometers from the sample surface [106]. The brightness of the signal depends on the number of secondary electrons reaching the detector. If the beam enters the sample perpendicular to the surface, then the activated region is uniform about the axis of the beam and a certain number of electrons "escape" from within the sample. As the angle of incidence increases, "the escape" distance of one side of the beam will decrease, and more secondary electrons will be emitted. Thus steep surfaces and edges tend to be brighter than flat surfaces, which results in images with a well-defined, three-dimensional appearance. A general introduction to SEM principles can be found in reference [106]. SEM studies in this work were performed with a LEO440 microprocessor-controlled scanning electron microscope with acceleration voltages up to 40 kV, with a resolution of 4 nm at 25 kV.

4.1.2 Transmission electron microscope

Transmission electron microscopy (TEM) is a microscopy technique where a beam of electrons is transmitted through an ultra thin specimen, interacting with it as they pass through. An image is formed from the interaction of the electrons transmitted through the

---

[1] Teardrop-shaped volume of the specimen which extends from less than 100 nm to around 5 μm into the surface. The size of the interaction volume depends on the electron's landing energy, the atomic number of the specimen and the specimen's density. In this volume the electrons lose energy by repeated random scattering and absorption, giving raise to the reflection of high-energy electrons by elastic scattering, emission of secondary electrons by inelastic scattering and the emission of electromagnetic radiation, each of which can be detected by specialized equipment.

specimen, which is magnified and focused onto an imaging device. Transmission electron microscopes detect the electrons transmitted through samples with a thickness below the mean free path of the electron travelling through the sample (in the order of tens of nanometers). In order to prepare the samples for TEM-analysis, pieces of the chalcopyrite/Zn(S,O) sample under study are cut and glued face to face in pairs with conductive epoxy, in order to avoid sample charging during the measurement. This method provides an even sample hardness distribution for the subsequent thinning step, as otherwise those softer compounds in the multilayer structure (glass, molybdenum, absorber, buffer) could be preferentially removed during the processing. Additionally, the total area that can be investigated with a single preparation is doubled, thus increasing the chances of finding an adequate area for TEM analysis across the sample. The preparation proceeds with the thinning of the sample by polishing with a diamond abrasive wheel and alumina paste, and a final milling stage with Ar^+ ions [107].

For the case of the TEM analysis of the particles precipitated in the solution, the sample preparation is easier than in the previous case. After finishing the deposition, part of the solution is collected, washed several times with ethanol and water, centrifuged and finally dried. A small quantity of the obtained powder is mixed again with ethanol and a drop of this mixture is placed on a Cu/C grid, which is afterwards analyzed in the TEM.

A commercial Philips CM12 transmission electron microscope with an operating voltage of 120 kV and a LaB_6 cathode and a ZEISS LIBRA 200 EF transmission electron microscope were used for this work. The theoretical resolution predicted by equation (4.1) (below 0.004 nm and 0.003 nm respectively) are not reached due to limitation imposed by the aberration of the electromagnetic lenses. The mode of operation is the bright field imaging mode. In this mode the contrast formation, when considered classically, is formed directly by occlusion and absorption of electrons in the sample. Thicker regions of the sample, or regions with a higher atomic number will appear dark, whilst regions with no sample in the beam path will appear bright, hence the term “bright field”.

4.2 Growth of Zn(S,O) buffer layers on chalcopyrite substrates

An example of a CIGSSe absorber film covered by a chemically deposited Zn(S,O) buffer layer can be seen in figure 4.1. The figure shows the tilted cross-section (taken at an angle of 30 °) of a Mo/$Cu(In,Ga)(S,Se)_2$/Zn(S,O) structure by means of a scanning electron microscope. The $Cu(In,Ga)(S,Se)_2$ absorber has been produced at an industrial pilot line by AVANCIS GmbH & Co. KG [13] and the buffer layer has been deposited under the same conditions used for processing photovoltaic devices. In the bottom part of the image, the top of the molybdenum back contact layer can be seen. The layer above the molybdenum is the absorber layer ($Cu(In,Ga)(S,Se)_2$ in this case). Despite the roughness of the absorber layer, its thickness can be estimated to be aproximatelly 1.5 μm. The $Cu(In,Ga)(S,Se)_2$

layer is polycrystalline showing crystal sizes that vary with the thickness. On the upper part of the absorber, close to the absorber/buffer interface, large crystals (with sizes in the order of 1 μm) can be observed. In the lower part of the absorber, close to the absorber/Mo interface, the size of the crystals found is drastically reduced showing in some parts a nanocrystalline structure. On top of the Cu(In,Ga)(S,Se)$_2$ absorber layer, the Zn(S,O) buffer layer is visible and covers the layer underneath with a thickness that cannot be estimated from this graph. Transmission electron micrographs of Cu(In,Ga)(S,Se)$_2$ samples buffered with Zn(S,O) have shown thicknesses of $\sim$ 20nm [108]*[2]. In the figure, the contrast differences are generated by the different composition of the various layers and by the orientation of each of the surfaces of the sample under study relative to the impigning electron beam.

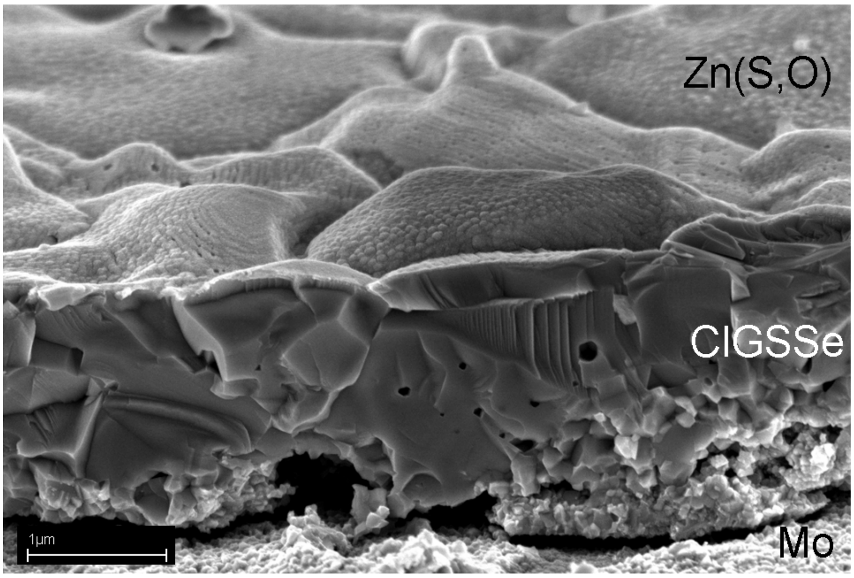

Figure 4.1: SEM-micrograph of a tilted (30 °) cross section of a Mo/Cu(In,Ga)(S,Se)$_2$/Zn(S,O) structure.

Figure 4.2 shows a CuInS$_2$ substrate buffered with a Zn(S,O) buffer layer using the standard CBD recipe and with the sputtered ZnO window layer on top. In the figure, a grain boundary between two CuInS$_2$ crystals can be seen, covered by the Zn(S,O) buffer layer. CBD enables the deposition of the Zn(S,O) layer even at hardly accesible regions such as grain boundaries, where other deposition processes, such as physical vapour deposition (PVD[3]), would fail.

The growth of the buffer layer can be investigated by analyzing with SEM, chalcopyrite substrated buffered during different deposition times. Measuring the transparency of

---

[2] References marked with * have Rodrigo Sáez-Araoz as an author and show results related to this work.

[3] Vacuum deposition process based on the condensation of a vaporized form of the material to be deposited. This material is placed in an energetic environment, so that particles may escape the surface. Facing this source there is a cooler surface which draws energy from the particles as they arrive after a ballistic flight, allowing them to form a solid layer.

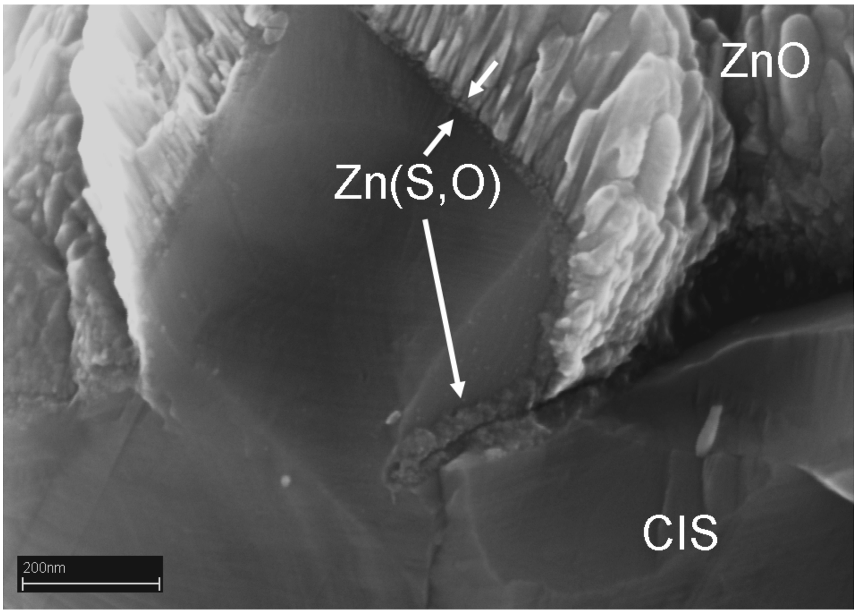

Figure 4.2: SEM cross sectional view of a CIS/Zn(S,O)/ZnO heterojunction showing the buffer layer covering the absorber even at the grain boundary between two $CuInS_2$ crystals.

the solution during the deposition enables a correlation of the different stages of the CBD (a first stage where no optically detectable particles are formed and a second stage where particles precipitate in the solution) with the growth of the buffer layer onto the chalcopyrite substrate. This is shown in figure 4.3 (a-c). The Zn(S,O) buffer layer is deposited using the modified CBD including additive (0.8 % of the total solution volume). The corresponding normalized transmission intensity (transparency) is also included in the graph. Figure 4.3 a) shows a SEM micrograph (top view) of a KCN-etched $CuInS_2$ absorber. Despite its roughness, CBD enables the coverage of the $CuInS_2$ absorber by a closed buffer layer after 250 seconds deposition time (transparency of the chemical solution $\sim 2\%$), as it can be seen in figure 4.3 c), where the contrast difference (on a given surface) is due to the presence of different materials. The SEM image of the $CuInS_2$ sample buffered during 120 seconds is shown in figure 4.3 b). The normalized transmission intensity at that point is $> 90\%$, indicating that the nucleation of detectable particles in chemical solution has just began. It can be seen that the Zn(S,O) layer is not totally closed and the $CuInS_2$ absorber can still be observed in certain regions (marked in the graph).

From this study, it can be concluded that the growth of the buffer starts when no particles are detected in the solution by the optical monitoring system. The growth begins at defined areas (islands) which grow laterally until the whole absorber is covered. Also, hardly accesible regions such as grain boundaries can be covered by the chemically deposited layer. More detailes about the closure of the buffer layer will be presented in chapter 5.

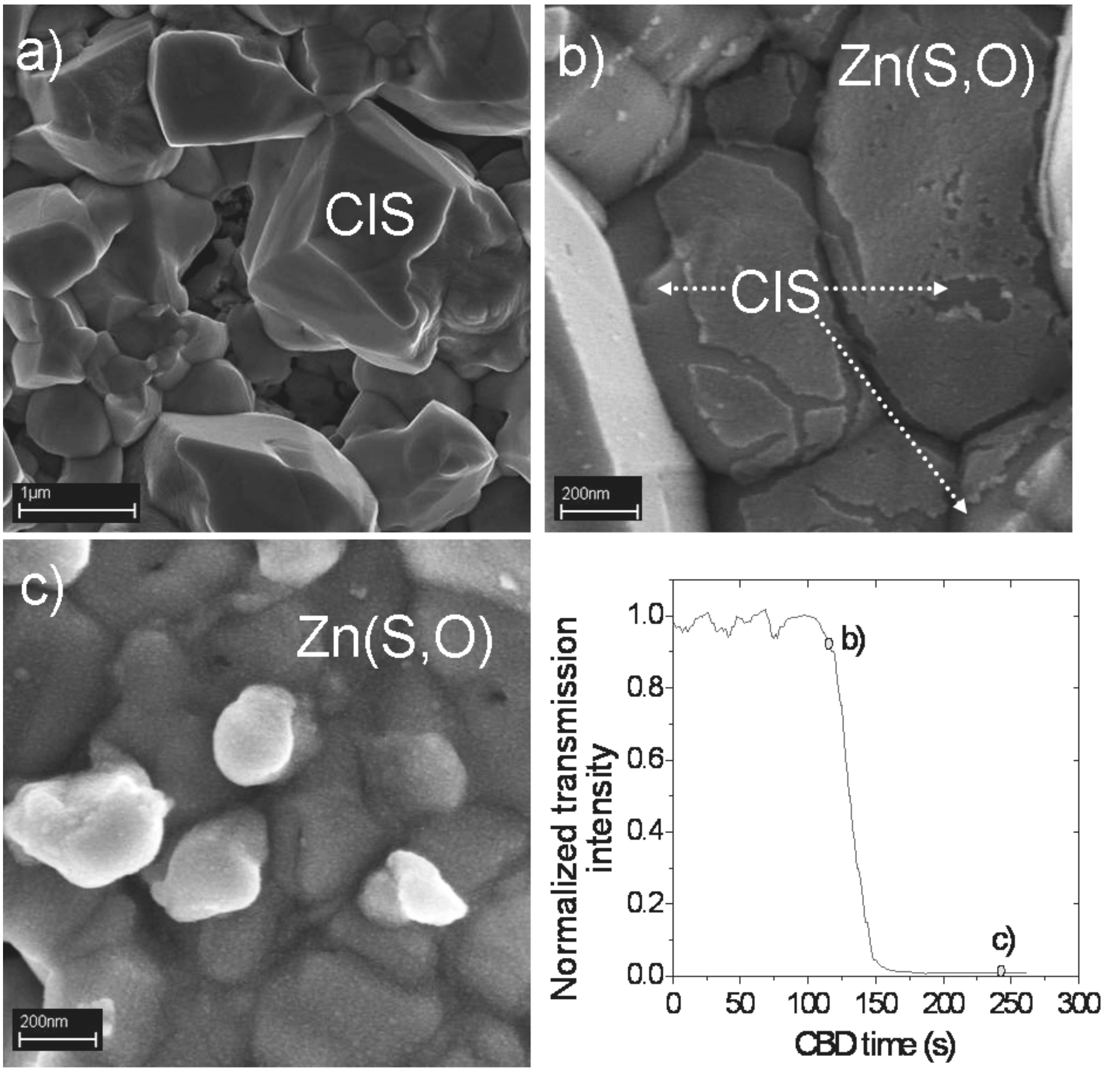

Figure 4.3: a) SEM top view of a KCN-etched $CuInS_2$ absorber. b) $Zn(S,O)/CuInS_2$ heterojunction after 2 minutes buffer deposition time. $CuInS_2$ is still visible under the growing buffer layer. c) $Zn(S,O)/CuInS_2$ structure after 4 minutes deposition time. The buffer layer covers conformally the absorber. Bottom right: transparency curve (normalized transmission intensity versus deposition time) obtained during the buffering of the $CuInS_2$ samples. Grey dots indicate the time and transparency values at which samples b) and c) were removed. These values are 120s and 90% for b) and 240 and 2% for c).

4.3 Morphology of Zn(S,O) buffer layers

In order to investigate the morphology and crystalline structure of the chemically deposited buffer layer on chalcopyrite absorbers, high resolution TEM images of chalcopyrite/Zn(S,O) heterojunctions have been analyzed. The results are correlated to the transparency of the chemical solution measured during the deposition of the buffer layer. Any changes in the structure of the buffer layer can be then related to the different stages identified by measuring the transparency of the solution. Furthermore, the crystalline structure of the buffer layer can be compared to that of the precipitate remaining in the chemical solution after the deposition process.

The lattice plane distances will be used to identify the nature of the crystallites forming the buffer layer. These distances are obtained either by direct inspection of the HR-TEM images or by the evaluation of the Fourier transform of the real image. If the samples are crystalline, diffraction of the impigning electrons may happen. This leads to the formation of diffraction patterns on the focal plane if Bragg's law is fulfilled [109]:

$$2d_{hkl} \cdot sin\Theta = \lambda \tag{4.2}$$

where d_{hkl} represents the distance between lattice planes, which are described by the Miller indexes h, k and l [110]. Θ represents the angle between the impinging electron beam and the lattice plane and λ is the wavelength of the probe electrons. From these diffraction patterns, the distance between lattice planes can be extracted by determining the transformed distance from the diffraction point (or ring in the case of polycrystalline samples) to the center (000) and performing the inverse transform to obtain the real distance. In order to identify the reflections appearing in the patterns (i. e. to find out to which lattice planes they correspond), additional information about the composition and crystal structure is often needed, since lattice planes with different hkl indexes are often separated by similar distances. The accuracy associated to the determination of lattice planes distances is mainly due to errors in the formation of the images and to temperature variations inside the transmission electron microscope [110]. In this work, the error is considered to be 0.2 $\AA$.

For this analysis, it is assumed that ZnS crystals are grown during the chemical bath deposition following the reactions discussed in section 3.1. Additionally, in CBD-grown nominal ZnS layers, other zinc-containing compounds, such as ZnO, have been identified (see chapter 5). ZnS crystals grow in both cubic and hexagonal structures, while ZnO crystals show a hexagonal structure. In the case of the precipitate obtained in the chemical solution by adding an insufficient amount of ammonia to the solution (see section 3.2), formation of $Zn(OH)_2$ particles is expected.

A literature enquire has been performed to compare those values obtained during the investigations carried out in this work and those found in the literature. Table 4.1 shows the d_{hkl} values found in the literature (d_{Lit}) with their corresponding Miller indexes (hkl). Presented are the three most intense reflections for the corresponding compound. The data for $Zn(OH)_2$, which crystallizes in orthorombic [111, 112], hexagonal [113, 114] and tetragonal [115, 116] structures, with intense lines at d_{hkl} values ranging from 0.759 nm (orthorombic (110), intensity = 53 [112]) to 0.182 nm (tetragonal (325), intensity = 33 [116]) is not included, since it is expected that $Zn(OH)_2$ transforms to ZnO during the drying step.

Figure 4.4 shows HR-TEM images of CIS/Zn(S,O) structures buffered using the stan-

Table 4.1: Values found in the literature of lattice plane distances d_{hkl} with their corresponding lattice planes (hkl) for ZnS (both cubic and hexagonal structures) and ZnO (hexagonal structure) within the region of interest. Additionally, the three most intense reflections of $CuInS_2$ are included for comparison. (*fcc* stands for face-centered cubic, *hex* stands for hexagonal and *tetra* stands for tetragonal).

Structure	$d_{Lit}[\mathring{A}]$	Intensity	(hkl)
ZnS, *fcc* [117] ICSD 067790	3.12	100	(111)
	2.67	63	(200)
	1.90	50	(220)
ZnS, *hex* [117] ICSD 067777	3.27	100	(100)
	3.09	61	(002)
	2.89	95	(101)
ZnO, *hex* [118] ICSD 082029	2.81	57	(100)
	2.60	42	(002)
	2.48	100	(101)
$CuInS_2$ *tetr* [119] ICSD 082029	3.18	100	(112)
	1.95	35	(204)
	1.66	23	(312)

dard CBD process (figure 4.4 a)) and with the modified process including the additive (figure 4.4 b)). The buffer deposition times are 20 minutes for the standard CBD and 5 minutes for the modified one.

The straight-away conclusion is that the deposition rate is highly enhanced when the additive is included in the chemical bath. The increased particle formation speed detected during the analysis of the transparency curves of the chemical solution (see figure 3.15 in section 3.4.3) is indeed translated into a higher depostion rate on the absorber. When average growth rates are calculated, 2 nm/min is obtained for the modified CBD, a rate eight times higher than the 0.25 nm/min obtained in the case of the standard CBD.

The inset in figure 4.4 a) shows a close-up view of the absorber/buffer interface at the indicated position. The lattice plane distances are $\sim$ 3.2 $\mathring{A}$. In the case of the $CuInS_2$ absorber the value of d_{112} is 3.195 $\mathring{A}$. The crystallites forming the buffer layer can be ascribed to either hexagonal ZnS (111), (102) or (0010) or to cubic ZnS (111) (see table 4.1). The match of the lattice constants on either size of the junction enables the deposition of an epitaxial layer. This is considered as the result of the ion-by-ion growth that takes place during the early stage of the chemical deposition process, in which no particles are detected in the chemical solution. This situation can be seen at different positions of the absorber/buffer interface, but it cannot be concluded that this epitaxial layer is closed.

In the case of the samples process with the additive (figure 4.4 b)) the situation is different. At the interface between the absorber layer and the nanocrystalline buffer layer the perfect continuation of lattice planes is not obvious and the existance of position at the

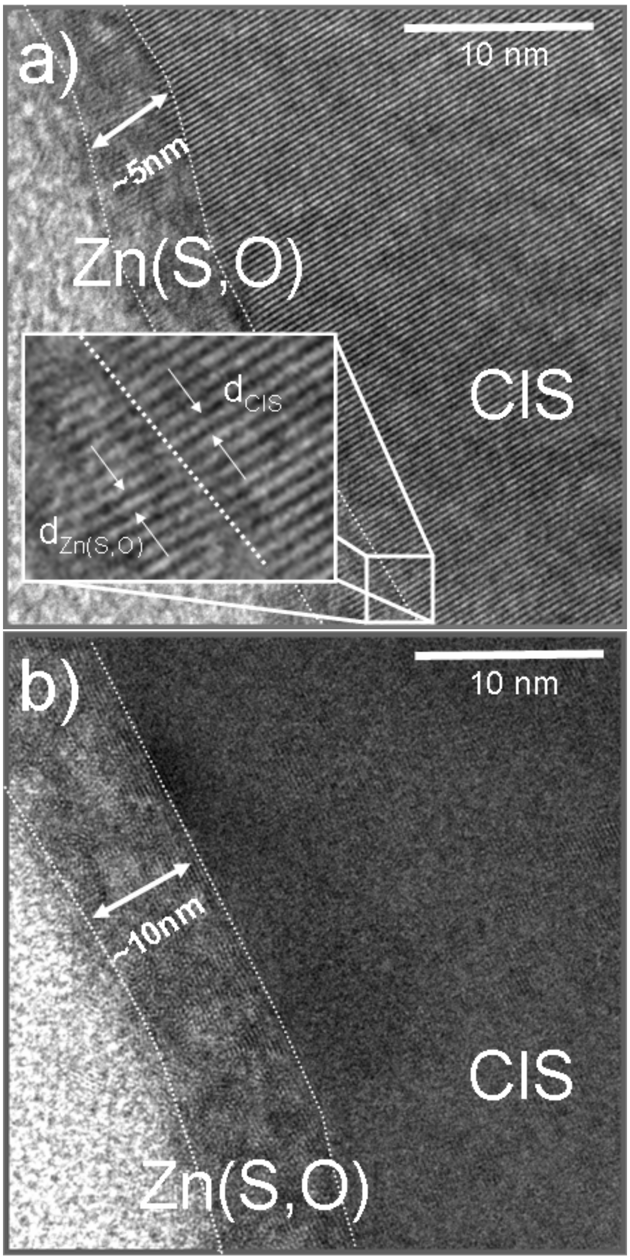

Figure 4.4: HR-TEM images of Zn(S,O) buffered CIS samples. a) Sample buffered using the standard CBD process during 20 minutes, including an inset with a close view of the CIS/Zn(S,O) interface and lattice plane distances. b) Sample buffered using the modified CBD during 5 minutes. The buffer layer is highlighted bewteen dotted lines. The bright areas (bottom right in both figures) correspond to the conductive epoxy glue.

interface where epitaxial growth is present cannot be concluded. This behaviour is correlated to the transparency graphs (figure 3.15) shown in section 3.4.3. The initial plateau, in which the catalytic action of the absorber enhaces the heterogeneous deposition of ZnS in an ion-by-ion process, is greatly reduced when the additive is included. The homogeneous nucleation begins rapidly and the buffer layer mainly consists of nanocrystallites formed in the bulk of the solution and deposited onto the absorber layer. The distances between lattice planes of individual crystals can be estimated from the HR-TEM images, and are in both cases (standard CBD and CBD with additive) between 3.25 and 3.05 $\mathring{A}$, again corresponding to ZnS in cubic or hexagonal structures. The sizes of the individual crystallites is approximately 3-4 nm.

Further TEM investigations have been performed on Cu(In,Ga)$(S,Se)_2$/Zn(S,O) heterojunctions where the buffer layer is deposited using the standard CBD with a deposition time of approximately 20 minutes [120]*. A HR-TEM image of such a device is shown in figure 4.5 a). The buffer layer has a thickness of approximately 20 nm and two different regions can be identified. Directly on the absorber, a intermediate layer with a thickness of 3-5 nm can be observed. The continuation of the absorber lattice planes by those of the buffer layer is here again an indication of a probable ion-by-ion growth mechanism by heterogeneous reaction promoted by the catalytic activity of the absorber. On top of this region, a polycrystalline layer is found. The average diameter of the crystallites is 3-4 nm and no size distribution is found as a function of the thickness. The fact that the crystallite size remains constant regardless of the thickness (i.e. the deposition time) is a clear indication of deposition occurring during the homogeneous nucleation, as it is expected from the second deposition stage, where the turbidity of the solution increases due to the formation of particles in the solution. Additionally, energy filtered TEM (EF-TEM) [4] has been performed on the cross section of the Cu(In,Ga)$(S,Se)_2$/Zn(S,O) heterojunction. The aim is to obtain a mapping of the sulphur distribution accross the interface. This is shown in figure 4.5 b), where the brighter areas indicate a sulphur enrichment. In order to quantify this phenomenon, twenty individual sulphur profiles were measured from the region highlighted in a grey box shown in 4.5 b). The average of the twenty individual profiles is displayed in figure 4.5 c) as a function of the position (0 in the distance-axis corresponds to the surface of the buffer layer). Regarding the results obtained, it can be seen that there is a sulphur enrichment in the first 4 nm of the buffer layer, close to the absorber layer (between 18 and 22 nm apart from the buffer surface). This region corresponds to the region depicted previously (4.5 a) and b)), where an epitaxial growth of the buffer layer is expected by an ion-by-ion mechanism. As the buffer layer thickness increases, there is a gradual reduction of the sulphur content, pointing to a thickness dependent buffer layer composition.

These results can be compared to those obtained analyzing the precipitate collected after the deposition process. Figure 4.6 shows a TEM image of the edge of cluster precipitated in the solution during the deposition process, together with its corresponding diffraction pattern. The precipitate is collected from a standard CBD process. The TEM

---

[4] In energy filtered TEM, electrons which have lost a certain amount of energy in inelastic scattering processes are selected in order to create an image with those electrons. Since the energy loss spectrum of a material contains a signature of all the chemical species present, one can actually “tune in” to a certain element and obtain an elemental map.

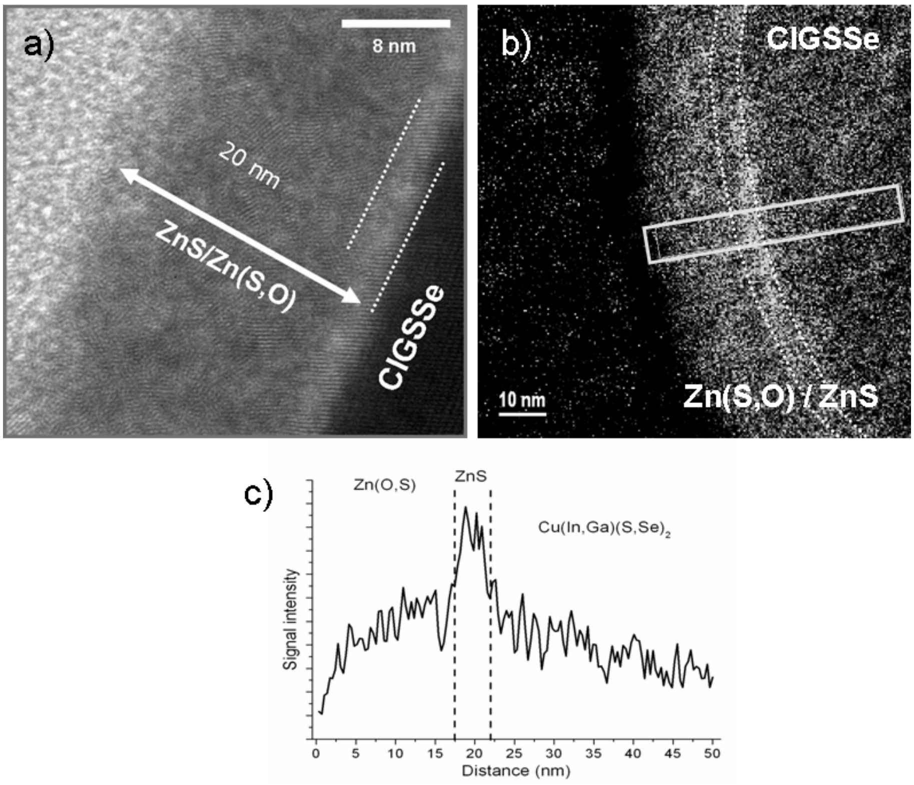

Figure 4.5: TEM investigation of Cu(In,Ga)(S,Se)$_2$/Zn(S,O) structures. a) HR-TEM image of the Zn(S,O)/Cu(In,Ga)(S,Se)$_2$ interface, indicating the presence two distinct layers in the buffer. b) Energy filtered TEM sulphur distribution map of the same interface at a different position, showing an enhanced sulphur signal in the intermediate layer (brighter region). c) Sulphur distribution profile extracted from the region highlighted (white box) in figure 4.5 b), representing the average of 20 individual profiles.

image (figure 4.6a)) reveals a nanocrystalline structure similar to that observed in the buffer layer (see figure 4.4 and 4.5). The diameters of the nanocrystals are below 5 nm. Differences in the brightness are due to different thickness of the sample under analysis. The region highlighted by a black box in figure 4.6 a) has been Fourier-transformed in order to obtain its diffraction pattern, which is shown in figure 4.6 b). Since the area selected for the analysis includes only a few crystals, points in the diffraction pattern are present. The distances between lattice planes obtained from the analysis of both the whole HR-TEM image and for the detailed study of the selected transformed area are approximately 0.31 nm. According to the literature data presented in table 4.1, the crystallites analyzed can be ascribed to hexagonal or cubic ZnS.

Figure 4.7 shows both the TEM image (a) and the corresponding diffraction pattern (b) of the edge of a cluster precipitated in the solution during the CBD process including additive. The crystalline structure of the particle is similar to that of the previous example (figure 4.6). The particle is also polycrystalline (as confirmed by the the presence of a

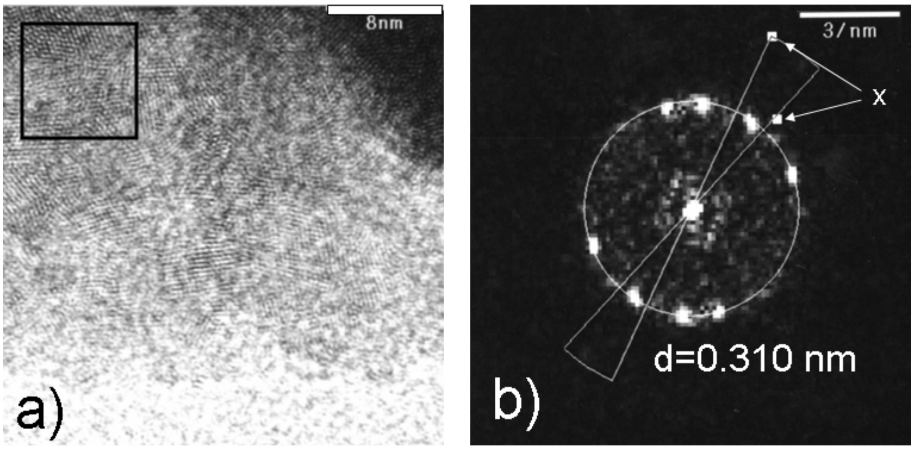

Figure 4.6: a) HR-TEM of a particle precipitated during a standard CBD process. b) Electron diffraction pattern obtained by Fourier transforming the area highlighted by a black bok in a). Points indicated with an *x* are artifacts originated by the analysis software.

ring in the diffraction pattern) and consists of nanocrystallites with sizes below 5 nm in diameter. It is formed by agglomeration of the individual crystallites nucleated during the deposition process. By analyzing the diffraction pattern obtained by Fourier-transforming the real image (figure 4.7 a)) the distance between lattice planes can be extracted. The diffraction pattern shows clearly one ring at a (transformed) distance of 0.31 nm. Here again, and according to the literature data presented in table 4.1, the crystallites analyzed can be ascribed to hexagonal or cubic ZnS.

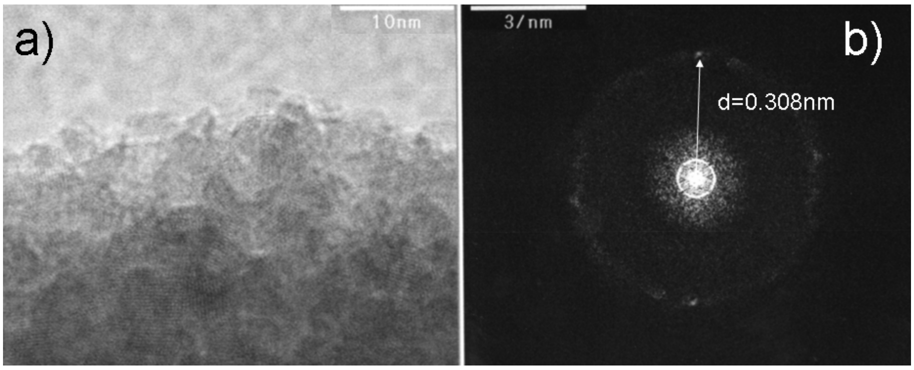

Figure 4.7: a) HR-TEM of a particle precipitated during a CBD process including additive. b) Corresponding electron diffraction pattern obtained by Fourier transforming the HR-TEM image (a).

Further analysis of different regions of the particles under investigation show different d_{hkl} values ranging from 3.07 to 3.25 $\AA$. Although these values lie within the error of $\pm 0.2\AA$, there is clear evidence that there are at least two different d_{hkl}. In the analysis of some images (both for the standard and the modified CBD process), two distict reflections, corresponding to two different d_{hkl}, can be observed. An example of this situation is shown in figure 4.8. The Fourier transform corresponding to the area highlighted in a black box in the HR-TEM image is shown in the inset. The guiding white circle helps to distinguish the two d_{hkl}. Some of the reflections appear outside the circle, with a corresponding d_{hkl} of approximately 0.31 nm. Some other reflections appear inside the circle, with a larger d_{hkl} of 0.33 nm. Since we are working in a transformed space, the distances are inverted so the reflections closer to the center, show larger values of d_{hkl}.

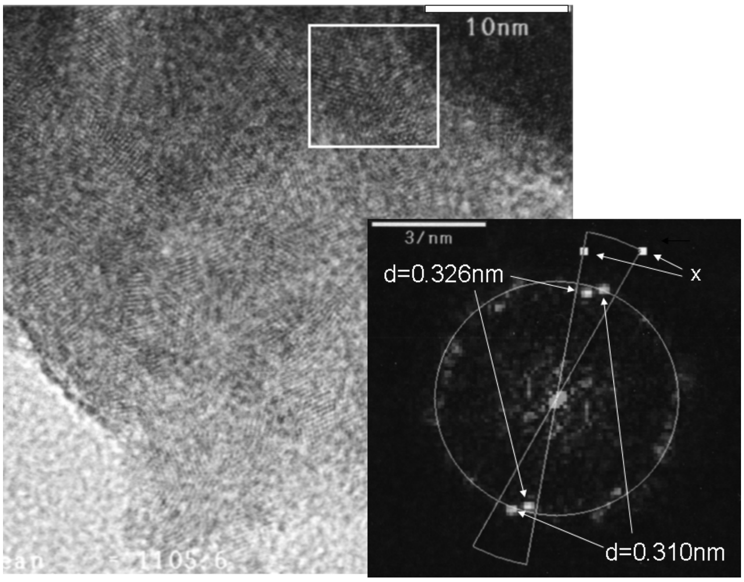

Figure 4.8: HR-TEM of a particle formed during the CBD in the bulk of the solution with the corresponding diffraction pattern obtained from the Fourier transform of the area highlighted in a white box. Two distinct reflections with different d_{hkl} (0.31 and 0.33 nm) can be seen. Points indicated with an *x* are artifacts originated by the analysis software.

It was mentioned in the previous chapter (section 3.2.1 in page 27) that if not enough ammonia is added, the $Zn(OH)_2$ formed does not redissolve and the solution becomes turbid. The precipitate formed in this way has been also analyzed by means of TEM and the corresponding electron diffraction patterns. In order to obtain this precipitate, a few drops of ammonia are added to the solution containing zinc salt and thiourea. A few seconds later, the solution is completely opaque, showing a white coloration. In all images analyzed, the inferred d_{hkl} showed values between 0.26 and 0.29 nm. The crystal structure of the particle was also nanocrystalline, although the sizes of the individual crystals were in some cases slightly larger (6-8 nm) than in cases where the precipitate was obtained from the standard or the modified (with additive) CBD. According to the literature data presented in table 4.1, the crystallites analyzed can be ascribed to hexagonal ZnO.

4.4 Summary

From these morphology and structure studies of both deposited buffer layer and precipitates formed in the solution, the conclusions obtained from the kinetic studies presented in the previous chapter have been corroborated and extended:

- There is a correlation between the formation of a turbid solution in the chemical bath and the deposition of material on the substrate. The growth of the buffer layers begins at locally-determined regions (islands) during the first stage of the deposition process, while the chemical solution stays clear. The resulting epitaxial layer (with a thickness up to 3-4 nanometers) is not closed and an enhancement of the sulphur concentration is found within this layer. Once the precipitation begins in the solution (homogeneous nucleation), the regions of the absober's surface not yet covered by the thin ZnS layer, will be covered by a nanocrystalline layer resulting from the deposition of the homogeneously nucleated crystallites. These nanocrystallites show sizes up to 4 nm. The deposition takes place during the second stage of the CBD process, where homogeneous nucleation is dominant. The sizes of the crystallites found in the buffer layer and in the particles from the precipitate are approximately equal. This supports the idea of a deposition process based on homogeneous nucleation -cluster mechanism-, since a continuous ion-by-ion growth would result in larger crystals.

- In the case of the modified CBD proccess (with the additive), the increased particle formation rate identified with the optical monitoring tool is indeed translated into a higher deposition rate. In this case, the pateau in the transparency measurement found during the first stage of the deposition process is greatly reduced and the homogeneous nucleation begins earlier. The epitaxial deposition taking place during the first stage is not found in samples buffered using the modified CBD process.

- The crystalline structure found by TEM analysis on buffered chalcopyrite samples correspond to ZnS crystallites either in hexagonal structure alone or with the inclusion of some cubic ZnS crystallites. The same crystalline structure is found in the precipitates obtained after the deposition process for both the standard CBD and the modified CBD with additive. There is no presence of ZnS crystallites in the precipitate formed after the addition of ammonia if sufficient NH_3 concentration is not reached. Zn-O compounds are most probable according to the analysis of the diffraction patterns. The presence of ZnO in the buffer layer has not been confirmed. Therefore, photoelectron spectroscopy investigation of the microstructure of Zn(S,O) are performed on Zn(S,O)-buffered $CuInS_2$ samples.

Chapter 5

Microstructure of Zn(S,O) buffer layers studied by photoelectron spectroscopy

The expected buffer layer composition predicted by the theoretical studies of the chemical bath deposition presented in chapter 3 was only partially corroborated by the growth and morphology studies carried out in chapter 4. Therefore, the study of the microstructure of chemically deposited buffer layers by photoelectron spectroscopy will be discussed.

Fundamental issues such as the deposition rate and the composition of the buffer layer can be investigated by using X-ray photoelectron spectroscopy (XPS) and X-ray excited Auger electron spectroscopy (XAES). XPS analysis, also referred to as ESCA (electron spectroscopy for chemical analysis), and XAES are used to acquire information about the chemically-deposited buffer layer composition as a function of the film depth.

After a short description of the theoretical aspects of photoelectron spectroscopy, the results obtained by investigating buffered samples by this technique will be explained. Information about the buffer layer composition for samples buffered using the standard chemical bath deposition process and the deposition process with additive, together with the band aligment determined for the latter case are presented.

5.1 Theoretical aspects of photoelectron spectroscopy

Photoelectron spectroscopy (PES) is a surface characterization technique based on the photoelectric effect [121] by which a sample that is irradiated with light of sufficient energy emits electrons. The absorption of a photon with a given energy $h\nu$ by the sample induces an electronic transition described by:

$$h\nu = E_f - E_i \tag{5.1}$$

where E_f and E_i are the energy of the final and initial electronic states respectively. After the absorption of the photon, the electron, which originally occupied a bound state of the discrete spectrum, is promoted either to the unoccupied part of the discrete spectrum or to the continuum of states above the vacuum level. The electrons that are promoted above the vacuum level are characterized by their kinetic energy (E_{kin}), which is related to the binding energy of the initial state (E_B), to the energy of the incoming photon ($h\nu$) and to the work function (Φ) of the electron analyzer by the following expression:

$$E_{kin} = h\nu - E_B - \Phi \tag{5.2}$$

Since it was first developed in the 1950's [122] photoemission has become one of the most widely used characterization techniques for material surfaces, in any of its versions: X-ray photoelectron spectroscopy (XPS), ultraviolet photoelectron spectroscopy (UPS) and X-ray excited Auger Spectroscopy (XAES).

5.1.1 X-ray photoelectron spectroscopy (XPS)

In core level XPS, the intensity of those photoelectrons emitted by the sample (see figure 5.1 a)) is measured as a function of their kinetic energy[1]. Photoemission peaks are labelled according to the quantum numbers of the corresponding original levels, following the standard spectroscopic notation (orbital momentum l = 0, 1, 2. . . denoted as s, p, $d\ldots$). All levels with $l \geq 1$ show the corresponding spin-orbit splitting, appearing in the spectrum as a doublet with a characteristic energy separation.

The typical probing depth of the XPS lies below 10 nm, depending on the kinetic energy of the photoelectron. A property of photoelectrons which defines the surface sensitivity of the XPS method is the mean free path. Here the electron energy lies typically between 10 and 2000 eV and for these kinetic energies, the mean free path is approximately 0.5-3 nm, resulting in an extremely sensitive method for surface characterization.

The position of the peaks in an XPS spectrum that is recorded from a specific sample can be used to identify the constituent elements by comparison with reference data available from the literature [123, 124, 125]. Quantitative analysis is also possible as the peak intensity is directly related to the concentration of atoms. Furthermore, the chemical environment of the elements present in the sample can be studied by means of XPS. The characteristic binding energies of photoelectrons do not merely depend on the specific element, but also on the chemical state of the corresponding atom. Chemical shifts are recorded as a displacement (typically in the range of 0 to 3 eV) in binding energies of photoelectrons excited from atoms in a compound compared to the energies of the corresponding pure substance. Binding energies, for example, increase with the oxidation state of a substance, since part of the electronic density is transferred to the oxydizing species, leaving the remaining electronic density unbalanced against the positive nuclear charge. It is therefore possible to deconvolute a core level peak into its different contributing parts for different oxidation states and/or partial changes of electron density and the resulting

---

[1] And typically plotted as a function of the electron binding energy according to equation (5.2).

peak areas can be related to the concentration of atoms in the individual states [123].

5.1.2 X-ray excited Auger spectroscopy (XAES)

In addition to the characteristic peaks corresponding to discrete levels at characteristic energies E_B, the XPS spectrum contains additional peaks, the so-called Auger peaks, which arise from the relaxation of photoionized atoms by Auger transitions [126].

Once a photoelectron is emitted from a deeper atomic shell (figure 5.1 b)), the energy released when an electron from an upper shell relaxes into the lower energy state can cause the emission of either an Auger electron or a characteristic X-ray, as shown in figure 5.1 b) and c) respectively. In an Auger process the energy primarily released in the form of an X-ray photon is re-absorbed by the same atom and an Auger electron is emitted from an upper shell. Auger electrons have characteristic kinetic energies corresponding to the spectrum of the specific species under study and these energies are independent of the exciting energy. The notation of Auger transitions follows the X-ray level nomenclature (levels denoted as K, L, M, N$\cdots$, and sublevels denoted as numerical subindexes). In this accepted nomenclature, for example, a KLL Auger process describes the situation where the initial ionization occurs in the K shell, an electron from the L shell fills this state and the "internal X-ray" is used to eject an electron from the L shell. Valence states are denoted by V (e.g. MVV).

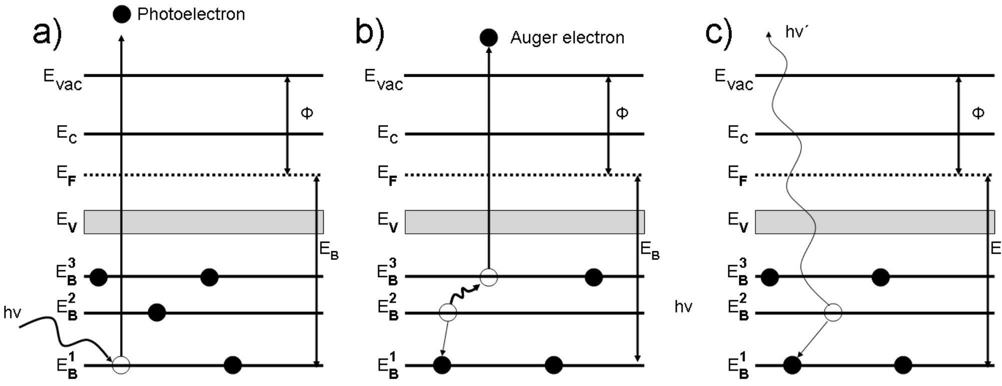

Figure 5.1: Schematic diagram showing the photoelectric effect a). The excited atom relaxes by filling the core level with an electron from a higher energy level. The released energy is either used to emit a second electron, the Auger electron b) or emitted as an X-ray photon c).

5.2 XPS analysis of Zn(S,O) buffer layers

Photoelectron spectroscopy is a useful tool to characterize the surface of the sample under study. Both the coverage of the underlying absorber layer by the buffer layer and the buffer layer composition can be investigated by means of XPS. The correlation of the results obtained from the photoemission data with the transparency data obtained using the monitoring system during the deposition of the buffer layer (section 3.3) can help to clarify the influence of the growth mechanisms on the composition of the buffer layer.

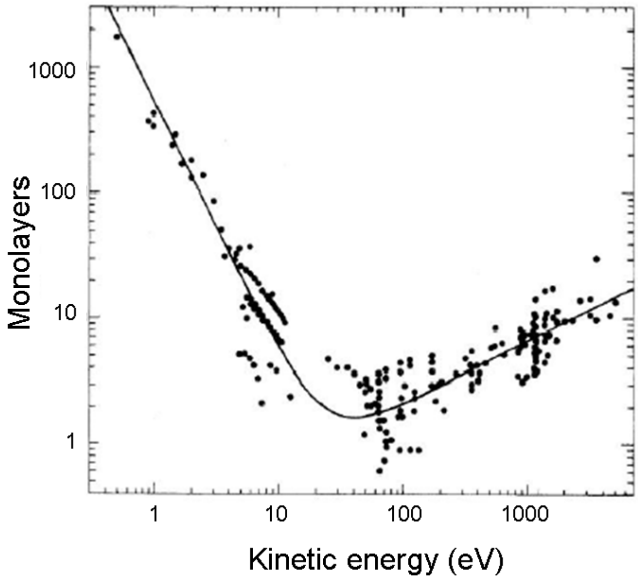

Figure 5.2: Universal curve for the mean free path (λ) of electrons as a function of their kinetic energy. Adapted from [123].

XPS spectra can be analyzed cuantitatively. The intensity of a core level line depends on various parameters. It is proportional to the photoionization cross section σ which depends on the element (Z), the core level (a_L) and the exciting energy ($h\nu$). Furthermore, it should be taken into account that apart from the electrons originated at the uppermost atomic layer, unscattered electrons from deeper layers of the sample will be detected. These electrons are attenuated by their inelastic free mean path. If the sample is sufficiently thick ($d>10$nm), the free mean path $\lambda(E_{kin})$ appears as a proportionality factor for the line intensity [127]. Figure 5.2 shows the so-called universal curve for the mean free path (λ) of electrons as a function of their kinetic energy [123]. Additionally, the line intensity I is proportional to the concentration of the element $c(Z)$ and to an analyzer transmission function $T(E_{kin})$ which depends of the kinetic energy of the electrons. Therefore, the expression describing the intensity of a core level line reads:

$$I \propto \sigma(Z, a_L, h\nu) \cdot c(Z) \cdot \lambda(E_{kin}) \cdot T(E_{kin}) \tag{5.3}$$

Since some of the parameters in equation (5.3) (specially the transmission function of the analyzer) are either not known or only rough approximations are available, the composition of the sample under study can only be approximately determined. The following considerations are taken into account:

- $T(E_{kin}) \propto E_{kin}^{-1/2}$ [123, 127].
- $\lambda(E_{kin}) \propto E_{kin}^{1/2}$ for E_{kin} >30 eV.
- values of σ(Z, a_L, hν), which actually depend on the chemical bond, the condition of the sample and the surface contamination are considered to be those found in the literature [128].

With these approximations, the expression for the concentration of an element at the sample's surface reads:

$$c(Z) \propto \frac{I}{\sigma(Z, a_L, h\nu)} \tag{5.4}$$

The photoionization cross sections given in reference [128] show an inaccuracy around 25% [129].

In order to correlate the transparency data obtained by using the monitoring system with the respective surface composition of the buffer layer at different deposition times (i.e. thicknesses), a complete set of samples (Glass/Mo/CIS) buffered during different deposition times is characterized using X-ray photoelectron spectroscopy (XPS) and X-ray excited Auger electron spectroscopy (XAES). In this way, the time-resolved deposition of the nominal[2] ZnS buffer layer by CBD leads to a thickness-resolved study of the coverage of the absorber and the composition of the buffer layer. A sample series consisting of $CuInS_2$ absorbers buffered during different deposition times is characterized using a Mg Kα x-ray source with an energy of 1253.6 eV. To minimize contamination from ambient air, the samples are sealed in a polyethylene bag filled with N_2 immediately after the deposition. The samples are then transferred from the chemical laboratory into the analysis chamber of a combined ultrahigh vacuum preparation and spectroscopy system ("CISSY"[130]) at a base pressure $\leq 1 \cdot 10^{-9}$ mbar via an attached N_2 filled glove box. A CLAM4 electron spectrometer from Thermo VG Scientific is used for electron detection. The electron spectrometer is calibrated using XPS and Auger line positions of different metals (Cu $3p$, Au $4f_{7/2}$, Cu L_3MM and Cu $2p_{3/2}$) according to reference [131].

In order to evaluate the results quantitatively, the photoemission signals are fitted by Voigt functions[3] after subtracting a background.

The thickness of the buffer layer can be estimated by using the attenuation of the $CuInS_2$ signals by the increasingly thick buffer layer, following:

$$I = I_0 \cdot e^{-d/\lambda} \tag{5.5}$$

where I is the intensity of the respective attenuated photoemission signal, I_0 is the unattenuated signal intensity of the bare (KCN-etched) $CuInS_2$ substrate, λ is the inelastic free

---

[2] Until the composition of the buffer layer is determined, it will be considered to be ZnS.

[3] Without loss of generality, if only centered profiles peaked at zero are considered, the Voigt profile is a convolution of a Lorentz profile and a Gaussian profile.

mean path (IFMP) of the corresponding photoelectrons, and d is the thickness of the attenuating buffer layer. λ can be calculated by the TPP-2 formula [132] using the QUAES code written by Tougaard, which provides values with an assumed uncertainty of $\sim 20\%$ [133].

In the following sections the results obtained analyzing the sample series buffered using the standard CBD process and the CBD process including a small concentration of additive by means of XPS and XAES will be discussed. Differences observed in composition and growth rate will be also shown.

5.2.1 Standard CBD process

For the study of the nominal ZnS buffer layer by XPS, a sample series consisting of 5 samples is prepared. The substrates to be buffered (all but one, which is used as a CIS reference) are introduced at the same time in the chemical bath solution described in section 3.2.1 (page 27) and removed after 180, 360, 540 and 810 seconds (3, 6, 9 and 13.5 minutes respectively). The surface characterization of this set of samples by means of XPS and XAES is considered to reveal a “time-resolved” (and thus “thickness-resolved”) view of the layer composition prepared in the chemical bath.

In addition, and according to the expected compounds formed during the chemical bath deposition of nominal ZnS layers, references of ZnO, $Zn(OH)_2$ and ZnS are also prepared and investigated for comparison:

- A thin ($\sim$ 100 nm) ZnO layer deposited on a CIS absorber by rf-magnetron sputtering is used as a ZnO reference.
- Storing a similar sample in ambient air for several days opens the route for H_2O adsorption at the ZnO surface, which leads to the formation of a surface $Zn(OH)_2$ layer [135]. This naturally generated hydroxide is used as a $Zn(OH)_2$ reference.
- The ZnS reference is prepared by the spray-ILGAR (ion layer gas reaction) technique [24].

The measured survey spectra of the buffer/$CuInS_2$ sample series can be seen in figure 5.3. The nominal ZnS buffer layer was deposited during 180 (b), 360 (c), 540 (d) and 810 seconds (e). Additionally the spectrum of an uncovered KCN-etched $CuInS_2$ sample is included (a). A summary of the binding energies of the core levels under study can be found in appendix A.

For the bare KCN-etched $CuInS_2$ sample, all detected photoelectron and Auger electron signals can be ascribed either to absorber's components or to adventitious carbon and oxygen, the latter probably being a remainder (adsorbed water) from the wet chemical removal of the Cu_xS surface phase by KCN etching. Regarding the spectra of the ZnS-buffered $CuInS_2$ samples, an intensity decrease of indium and copper XPS and XAES signals can be observed with increasing buffer deposition time. For the case of the remaining

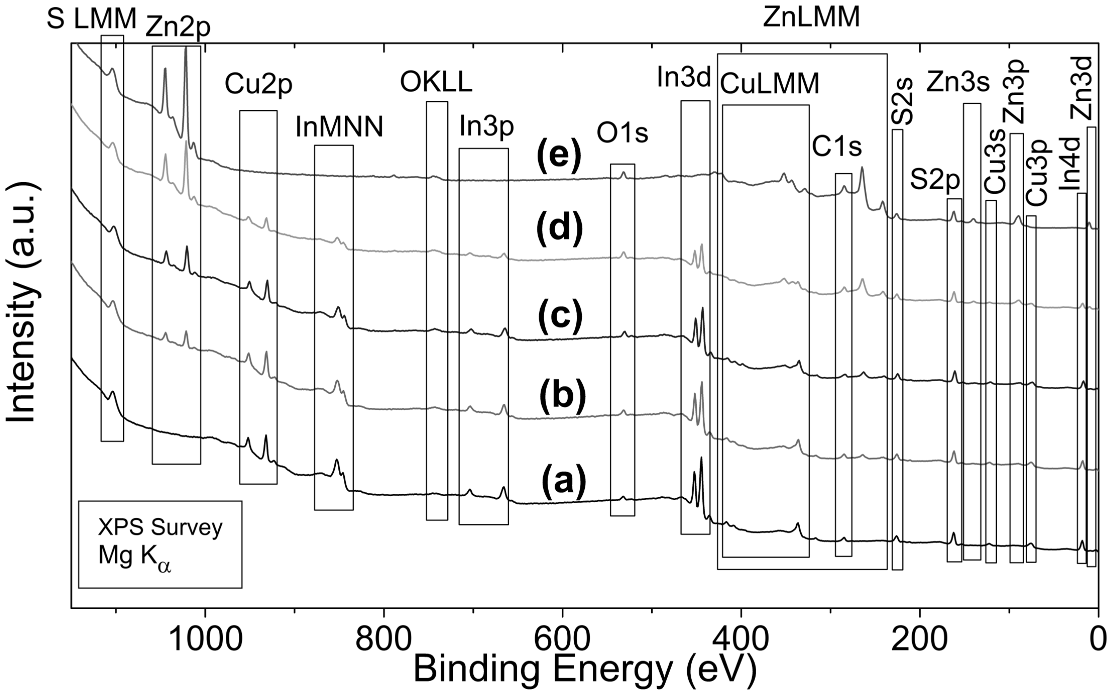

Figure 5.3: XPS survey spectra of the buffer/CuInS$_2$ sample series. The nominal ZnS buffer layer was deposited with different deposition times: (b) 3 minutes, (c) 6 minutes, (d) 9 minutes and (e) 13.5 minutes. Additionally the corresponding spectrum of a KCN-etched CuInS$_2$ sample (uncovered) is presented (a). The binding energies of the photoemission signals under study are summarized in appendix A.

CIS-attributed signals (peaks corresponding to sulphur), no decrease is observed, mainly because the nominal ZnS buffer layer also contains this element. Additionally, an increase of the Zn-related photoelectron and Auger electron signals can be noticed. The presence of zinc containing compounds on the surface of the samples is visible after already 3 minutes deposition time (see for instance the Zn2p core level in figure 5.3(b)).

For the ZnS/CuInS$_2$ sample where the nominal ZnS layer has been deposited for 13.5 minutes, no signal attributed to copper or indium can be observed anymore. This means that the buffer layer deposited within 13.5 minutes (810 seconds) completely covers the CuInS$_2$ absorber with a minimal thickness that exceed the XPS information depth. This energy dependent information depth is considered to be at least three times the inelastic free mean path (λ) of the respective photoelectrons (accounting for an attenuation of 95% of the initial intensity) [131]. Assuming that, e.g., the In$3d_{5/2}$ photoelectrons (with a binding energy E$_B$ $\approx$444 eV) are exclusively attenuated by a pure ZnS layer covering the absorber homogeneously, the thickness of the buffer layer can be estimated to be $\geq 5.4 \pm 1.1$ nm (based on the λ taken from reference [133] and equation (5.5)).

In order to have a more accurate information about the composition of the deposited layer on CuInS$_2$, the Zn$L_3M_{45}M_{45}$ XAES spectrum can be evaluated. The reason for choosing this particular signal ($E_{kin} \sim 988$ eV) is that it is more sensitive with respect to chemical shifts when compared to most Zn photoemission lines (i.e. Zn3d -$E_B \sim 11$ eV- or Zn2p -$E_B \sim 1022$ eV-) [124]. Figure 5.4 shows the XAES detailed spectra of the $CuInS_2$/ZnS sample series under study.

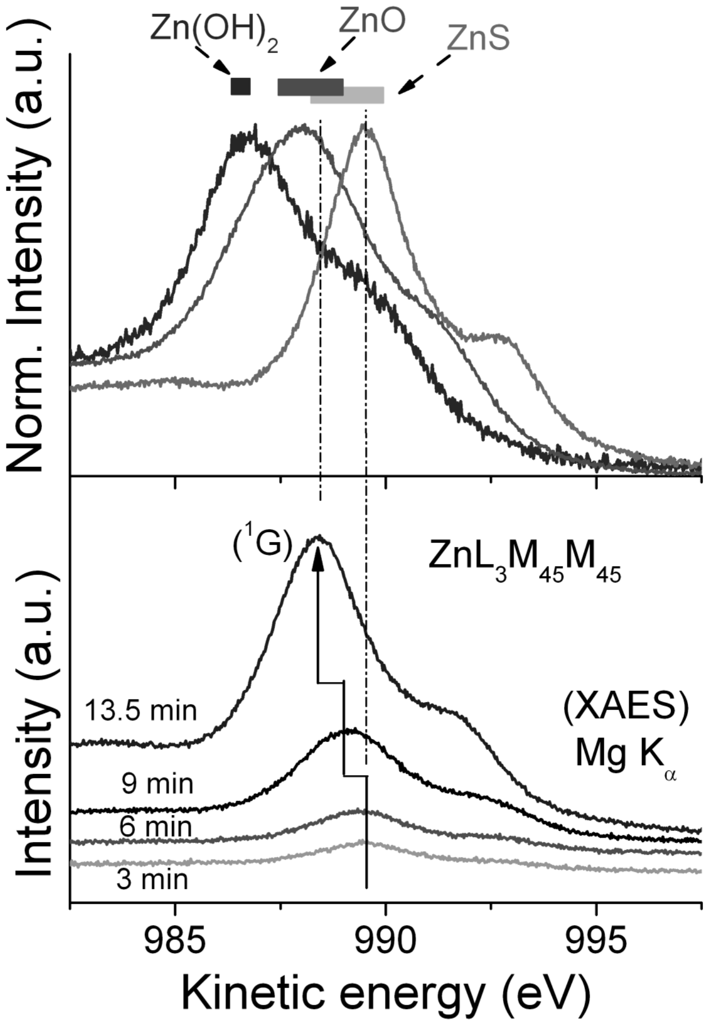

Figure 5.4: XAES detailed spectra of the ZnS/$CuInS_2$ sample series. In the bottom graph the Zn$L_3M_{45}M_{45}$ peaks are shown for various deposition times. In the top graph, the measured ZnO, ZnS and $ZnOH_2$ reference Zn$L_3M_{45}M_{45}$ peaks are shown together with bars representing the data found in the literature for those compounds. Adapted from [134]*.

Two different phenomena can be identified by looking at figure 5.4. On one hand the intensity of the Zn$L_3M_{45}M_{45}$ XAES signal increases with increasing deposition time due to the increasingly thick buffer layer. This effect is more pronounced specially for the samples where the deposition was stopped in the second half of the CBD (deposition time $\geq$ 9 minutes). This is also supported by the increase of the Zn-related photoemission signals as well as by the attenuation of the copper and indium related peaks (see figure 5.3). According to the intensity variation of the core level signals, the growth rate in the early stages of the deposition (time $\leq$ 6 minutes) is apparently much slower compared to that of deposition times above 9 minutes. This fact points to a deposition-time dependent growth mechanism of the nominal ZnS buffer layer.

Additionally a shift of the Zn$L_3M_{45}M_{45}$ Auger peak can be observed, from a kinetic energy E$_{kin}$ of 989.5$\pm$0.1 eV for a deposition time of 3 minutes, to 988.4$\pm$0.1 eV for the 13.5 minutes buffer/CuInS$_2$ sample. It should be noted that this energetic shift is not caused by an interface formation-induced band bending, since the modified Auger parameters [136] calculated as $\alpha_1 = E_{kin}[ZnL_3M_{45}M_{45}(^1G) + E_B[Zn2p_{3/2}]$ and $\alpha_2 = E_{kin}[ZnL_3M_{45}M_{45}(^1G) + E_B[Zn3d]$ also decrease with deposition time, as it is shown in table 5.4. This fact, together with the behaviour of the oxygen related XPS and XAES signals (see figure 5.3) which increase specially for the samples buffered during 9 and 13.5 minutes, points to a deposition time- (and thus thickness-) dependent change in the composition of the nominal ZnS buffer layer.

A literature enquiry [125, 137] for reference positions of the Zn$L_3M_{45}M_{45}$ Auger peak of Zn compounds possibly formed in the chemical bath, such as zinc oxide (ZnO), zinc sulphide (ZnS) and zinc hydroxide (Zn(OH)$_2$), provides different values for the same material, which are summarized in table 5.1. These results are also shown in figure 5.4 (top) as bars. Note that the width of the bars does not necessarily represent the uncertainty of the values, since for Zn(OH)$_2$ only very few values have been published.

The comparison of the position of the Zn$L_3M_{45}M_{45}(^1G)$ Auger line of the measured XAES spectra from the nominal ZnS/CuInS$_2$ sample series (989.5 to 988.4 eV) with the measured reference spectra, as well as with the data extracted from the literature, suggests that for the thickest buffer layer (13.5 minutes), a Zn(S,O)-like surface composition is most probable, since the energetic position of its Zn$L_3M_{45}M_{45}(^1G)$ Auger peak (988.4$\pm$0.1 eV) can be found between that of ZnO [experiment: 988.0$\pm$0.1 eV; literature: 987.4 to 988.9 eV] and ZnS [experiment: 989.5$\pm$0.1 eV); literature: 988.2 to 989.9 eV]. The hydroxide-poor composition is in contrast to several other publications reporting on Zn compounds deposited by CBD [64, 69, 70], but can be explained by the rinsing step in an aqueous ammonia-containing solution after the material deposition in the chemical bath, avoiding an uncontrolled precipitation of Zn(OH)$_2$ on the sample. The position of the Zn$L_3M_{45}M_{45}(^1G)$ Auger peak of the samples prepared by shorter deposition times shifts to higher kinetic energies with decreasing deposition times, until it actually agrees (for the samples buffered during 3 and 6 minutes) with the energetic position of the Zn$L_3M_{45}M_{45}(^1G)$ Auger peak of the ZnS reference as well as with the literature data. From this fact, it can be concluded that the material deposition in the chemical bath described in section 3.2.1 takes place in two steps. In the initial stage of the deposition, primarily a thin ZnS layer is formed on the CuInS$_2$ substrate. If this pure ZnS layer is conformally covering the absorber it cannot be determined by XPS. Since there is

Table 5.1: Energetic positions of the Zn$L_3M_{45}M_{45}(^1G)$ Auger line as found for the buffer/CuInS$_2$ sample series and some Zn-compound references as Zn(OH)$_2$, ZnO and ZnS compared to the corresponding literature data. All experimentally determined values have an error of ± 0.1 eV. In cases where only a single literature value is reported, an error of ± 0.2 was assumed to represent its uncertainty [124].

	Experimental Zn$L_3M_{45}M_{45}(^1G)$ E$_{kin}$ (eV)	Literature Zn$L_3M_{45}M_{45}(^1G)$ E$_{kin}$ (eV)
Buffer/CIS		
3 minutes	989.5	/
6 minutes	989.5	/
9 minutes	989.2	/
13.5 minutes	988.4	/
References		
Zn(OH)$_2$	986.7	986.2±0.2 [137]
ZnO	988.0	987.4-988.9 [138, 139]
ZnS	989.5	988.2-989.9 [139, 140]

a presence of In- and Cu- related signals for the samples buffered during 3 and 6 minutes (see figure 5.3) it can happen that either the layer is not closed or that it is closed but does not exceed the XPS information depth. However, according to the SEM investigations of layers deposited in short times (see figure 4.3 in section 4.2) the presence of a non-closed layer during this early stage is most probable. Then, in the second stage of the deposition process, the growth rate is greatly increased compared to that of the initial stages, and a Zn(S,O) compound is deposited.

Although the Zn$2p_{3/2}$ and the Zn$3d$ core level signals are not as sensitive to chemical changes as the corresponding Zn$L_3M_{45}M_{45}$ Auger spectra, shifts of 0.7 and 0.8 eV can be identified in the XPS spectra of ZnO and ZnS references respectively (table 5.2).

Table 5.2: Measured energetic positions of Zn$2p_{3/2}$ and Zn$3d$ photoemission signals of sputtered-ZnO and ILGAR-ZnS references, together with their difference and the values obtained from the literature [125].

XPS Signal	Reference ZnO (eV)	Reference ZnS (eV)	Diff. (eV)	Literature ZnO (eV)	Literature ZnS (eV)
Zn$2p_{3/2}$	1022.4±0.1	1021.7±0.1	0.7±0.2	1021.2-1022.5	1021.7-1022.0
Zn$3d$	10.9±0.1	10.1±0.1	0.8±0.2	10.3-10.8	9.8-10.7

The Zn$2p_{3/2}$ and Zn$3d$ core level lines of the buffered CuInS$_2$ samples show a behaviour similar to that observed for the Zn$L_3M_{45}M_{45}$ Auger signal, i.e., a shift with increasing deposition time from a binding energy that correlates (within the error bars) with the energetic position of the respective peaks for the ZnS reference (for short deposition times ≤ 6 minutes), to higher binding energies, towards the energetic position of the Zn$2p_{3/2}$ and Zn$3d$ XPS signals of the ZnO reference (for larger deposition times, i.e., thicker buffer layer). This is shown in figure 5.5, where the valence band XPS spectra (including the In4d and Zn3d core levels) of the ZnS/CuInS$_2$ sample series is presented. The shift of the Zn3d core level towards higher binding energies is evident.

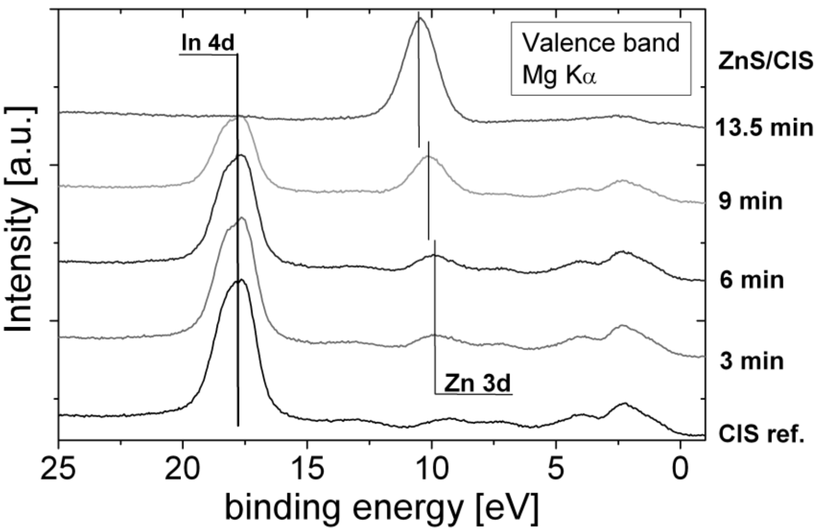

Figure 5.5: Valence band spectra of the ZnS/CuInS$_2$ sample series, including the Zn3d and In4d core levels.

These shifts in the Zn$2p_{3/2}$ and the Zn$3d$ lines (see figure 5.5), support the previous conclusion, by which a thickness dependant composition is expected, starting from a pure ZnS layer and ending with a Zn(S,O)-like composition. Therefore, it is considered that the Zn$2p_{3/2}$ and Zn$3d$ spectra of the buffer/CuInS$_2$ samples are composed of two contributions, namely ZnS and ZnO. In consequence, the measured Zn$2p_{3/2}$ spectrum can be in principle fitted using two Voigt functions, as shown in figure 5.6. For this fitting process, the full width at half maximum (FWHM) values of the photoemission signals of ZnS and ZnO references (1.7 and 1.9 eV respectively for the Zn$2p_{3/2}$ signal) are kept constant during the fit of the Zn$2p_{3/2}$ spectra of the buffer/CuInS$_2$ sample series. For the sample buffered during 3 minutes, a satisfactory fit of the signal was only achieved if just a contribution from ZnS was assumed, thus supporting the conclusion that a ZnS compound is formed directly onto the CuInS$_2$ substrate. Taking the error bars into account, the determined energetic positions of both contributions (ZnS and ZnO), $E_B^{Zn2p_{3/2}}[I] = 1021.6 - 1022.1$ eV, $E_B^{Zn2p_{3/2}}[II] = 1022.3 - 1022.8$ eV, agree with the energetic positions of the ZnO and ZnS references as well as with corresponding literature data (see table 5.4).

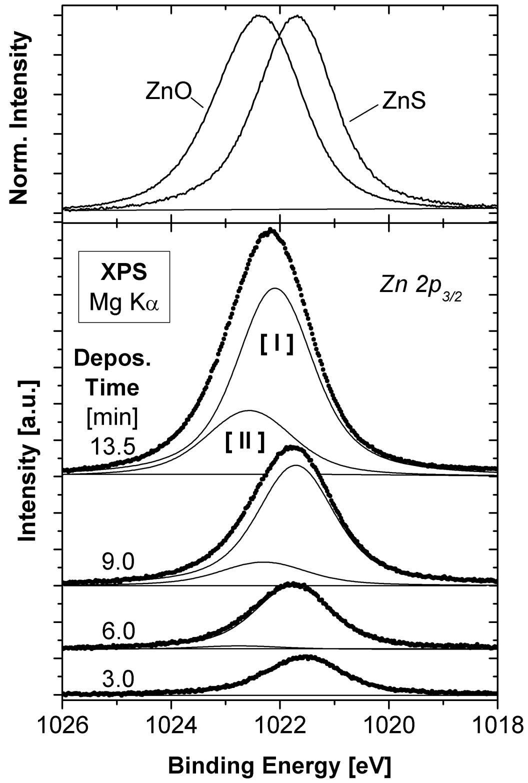

Figure 5.6: Zn$2p_{3/2}$ core level of the CIS/Zn(S,O) sample series, fitted using two contributions (shown on top), accounting for ZnS [I] and ZnO [II].

By using the areas below the Voigt profiles, which describe both contributions (ZnS and ZnO) to the Zn$2p_{3/2}$ spectra of the buffer/CuInS_2 samples series, the ZnS/(ZnS+ZnO) ratio as a function of the buffer thickness can be calculated. The photoionization cross sections depend on the chemical bond, so in principle, the cross sections of the ZnO and the ZnS contributions would be dissimilar. In practice, in a first approximation, these values are considered equal. Furthermore, in the literature data available only values for the core level are given, regardless of the chemical environment. In the case of the Zn2p$_{3/2}$ core level and for MgKα radiation (hν=1253.6 eV), the photoionization cross section is 18.01 in units of the C1s cross section of 22.200 barns [128]. The ZnS/(ZnS+ZnO) ratios for the buffer layers deposited on CuInS_2 substrates are summarized in table 5.3.

In order to exclude any impact of a varying band bending on the analysis of the energetic positions of the XAES and XPS signals and on the corresponding evaluation of the buffer layer composition, the value of the modified Auger parameter has been considered for the following discussion. The value of the modified Auger parameter $\alpha_1 = E_{kin}[ZnL_3M_{45}M_{45}(^1G) + E_B[Zn2p_{3/2}]$ calculated for the contributions attributed

Table 5.3: ZnS/(ZnS+ZnO) ratios calculated from the analysis of the Zn2$p_{3/2}$ photoemission spectra.

Deposition time	Zn2$p_{3/2}$ ZnS/(ZnS+ZnO)
3 min	1
6 min	0.94 ±0.05
9 min	0.82 ±0.05
13.5 min	0.76 ±0.05

to ZnS and ZnO of $Zn2p_{3/2}$ decreases with increasing deposition time (see table 5.4).

Table 5.4: Energetic positions of both contributions (ZnS and ZnO) of the $Zn2p_{3/2}$ photoemission line as measured for the ZnS/CuInS$_2$ sample series. In addition the corresponding values of the Auger parameter $\alpha_1 = E_{kin}[ZnL_3M_{45}M_{45}(^1G) + E_B[Zn2p_{3/2}]$ are calculated using the values presented in table 5.1. For comparison the energetic positions of the $Zn2p_{3/2}$ XPS signal and the respective values of α_1 for a ZnS and a ZnS reference as well as corresponding literature data (references [137, 125]) are also given. All values are given in eV and experimentally determined values have an uncertainty of ±0.1 eV.

Buffer/CIS	$Zn2p_{3/2}$ ZnS	$Zn2p_{3/2}$ ZnO	Lit. $Zn2p_{3/2}$	Expt. α_1(ZnS)	Expt. α_1(ZnO)	Lit. α_1
3 min	1021.6	/	/	2011.1	/	/
6 min	1021.8	1022.8	/	2011.3	2012.3	/
9 min	1021.7	1022.3	/	2010.9	2011.5	/
13.5 min	1022.1	1022.6	/	2010.5	2011.0	/
References						
ZnO		1022.4	1021.2-1022.5		2010.4	2009.5-2011.0
ZnS	1021.7		1021.7-1022.0	2011.2		2010.3-2011.9

The values of the contribution attributed to ZnS agree with the corresponding Auger parameters of ZnS (with both experimentally-determined and literature values) for samples where the deposition was stopped in the initial stage of the deposition process (transparency $\sim$ 100%). In contrast, the determined Auger parameter of contribution attributed to ZnO converges towards the experimentally-determined and literature values of the Auger parameter of ZnO for increasing deposition times.

These results support again the conclusion stated earlier in this chapter and in chapter 4, that the buffer layer deposition by the CBD process applied on CuInS$_2$ substrates forms a ZnS/Zn(S,O) bilayer.

Two different models can explain the shift of the Zn core levels as a function of the CBD deposition time. These are shown in figure 5.7.

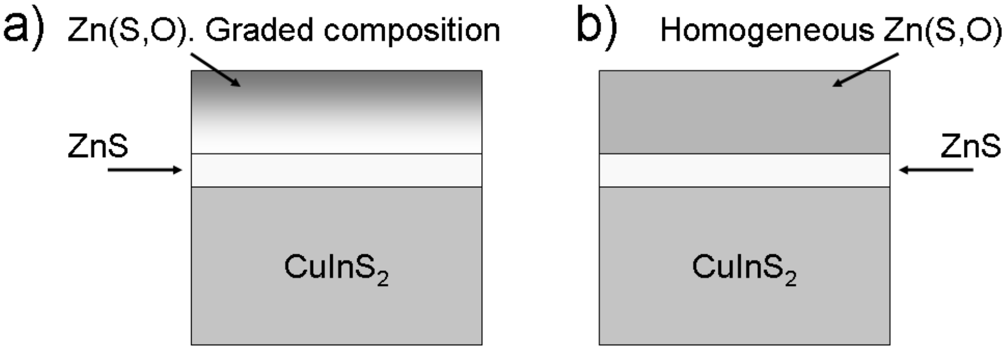

Figure 5.7: Schematic representation of the two different models that can explain the shift in the energetic position of the Zn core levels.

In figure 5.7 a) the buffer layer consists of a ZnS/Zn(S,O) bilayer in which the top Zn(S,O) layer has a graded composition, with an increasing oxygen content towards the surface. On the other hand, figure 5.7 b) represents the case in which the Zn(S,O) part of the ZnS/Zn(S,O) bilayer has a homogeneous composition. The energetic shift in the Zn core levels from energies corresponding to ZnS towards energies corresponding to ZnO is due to the disminishing contribution of the underlying pure ZnS layer. An exact evaluation of the correct model based on the XPS analysis is not possible without an exact knowledge of the thickness of the analyzed layers and the exact value of λ of ZnS and the corresponding composition of Zn(S,O).

On one hand, a desposition of a homogeneous material (in terms of composition) is expected during the second stage of the CBD, i.e. that where the cluster mechanism is dominant (see section 3.1). On the other hand EF-TEM investigations of ZnS/Zn(S,O) bilayers (see figure 4.5 in page 63) show a slight gradient in the sulphur distribution along the buffer layer. This can be explained by a simple model in which the deposition of ZnS (ion-by-ion process) is assumed to occur throughout the CBD process at a rate k_1. Firstly the deposition takes place directly on the substrate, but afterwards, when particles are formed in the solution, it can also take place on those particles. After a certain time, when conditions are reached for homogeneous nucleation, deposition of Zn(S,O) starts at a higher rate $k_2 > k_1$. Although the composition of this Zn(S,O) layer is homogeneous, the overall ZnS/(ZnS+ZnO) ratio decreases with time, with a speed that depends on both deposition rates and on the ZnS/ZnO ratio of the Zn(S,O) layer.

Considering that the deposition of the ZnS layer by means of the ion-by-ion process starts at $t = 0$ with a constant growth rate k_1 the amount of ZnS as a function of time can be expressed as:

$$[ZnS](t) = k_1 \cdot t \tag{5.6}$$

Parallely, if the deposition of Zn(S,O) starts after a given time t_i with a constant rate

k_2, the amount of Zn(S,O) as a function of time can be expressed as:

$$[Zn(S,O)](t) = \begin{cases} 0 & \text{if } t < t_i \\ k_2 \cdot (t - t_i) & \text{if } t > t_i \end{cases} \tag{5.7}$$

Figure 5.8 shows the amount of ZnS, ZnO and Zn(S,O) considering $k_2 = 10 \cdot k_1$ (the growth rate of the homogeneous nucleation 10 times that of the ion-by-ion deposition) and a ZnS:ZnO ratio of 4:1 (80% of ZnS) for the Zn(S,O) layer, which starts growing after 10 minutes. Additionaly the overall ZnS/(ZnS+ZnO) ratio as a function of the deposition time is also presented.

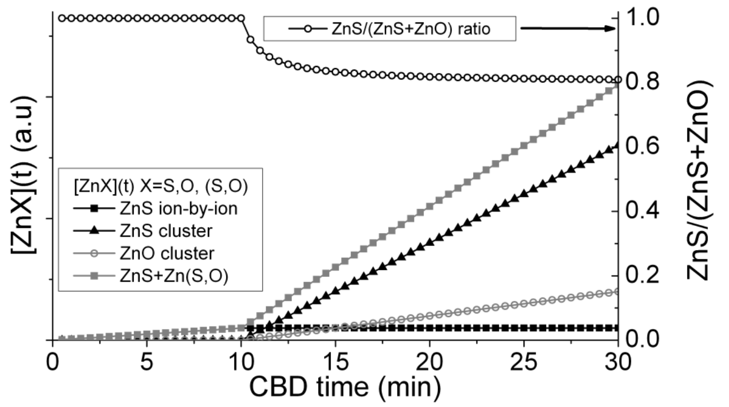

Figure 5.8: Schematic representation of the amount of ZnS (ion-by-ion and cluster mechanisms) and ZnO (cluster mechanism) deposited considering that ZnS is deposited at a constant rate k_1 at all times and a deposition of Zn(S,O) with a ZnS:ZnO ratio of 4:1 at a 10 times higher rate ($k_2 = 10 \cdot k_1$) for $t > t_i$. Additionally, the calculated ZnS/Zn(S,O) ratio as a function of time is also included.

With this model, the assumption of a homogeneous composition of the Zn(S,O) layer (i.e. a constant ZnS/ZnO ratio) is compatible with the slight gradient in the sulphur content observed in figure 4.5 (page 63). For the case of the XPS measurements one has to take into account that the probing depth of the technique lies below 10 nm, depending on the kinetic energy of the photoelectrons.

After a given time t_f, the amount of ZnS found on the layer as a result of the ion-by-ion deposition process can be determined as:

$$[ZnS] = \int_0^{t_f} k_1 t dt = \frac{k_1 t_f^2}{2} \tag{5.8}$$

and here again, after a given time t_f, the amount of Zn(S,O) found on the layer as a result of the heterogeneous deposition process can be determined as:

$$[Zn(S,O)] = \begin{cases} 0 & \text{if } t_i > t_f \\ \int_{t_i}^{t_f} k_2 t dt = \frac{k_1}{2}\left[t_f^2 - t_i^2\right] & \text{if } t_i < t_f \end{cases}$$

The calculations in this case must take into account the fact that the XPS intregrates the signals obtained within the probing depth. An schematic representation is shown in figure 5.9. The composition of the buffer layer is represented as a function of the deposition time. During the first stage, where only ZnS (ion-by-ion) is deposited, the position of the Zn-core levels remains constant at an energy E_1. The deposition of Zn(S,O) starts at $t = t_i$. For $t_i < t < t_x$ XPS detects signals from both the ZnS and the Zn(S,O) layer. Since the growth rate of Zn(S,O) by the cluster mechanism is higher than that of pure ZnS by means of ion-by-ion process, the positions of the Zn-core level shift towards higher binding energies, from E_1 to E_2. This accounts for the increasing ZnO contribution to the total detected signal. For $t > t_x$, the positions of the Zn-core levels should remain constant at a given energy E_2.

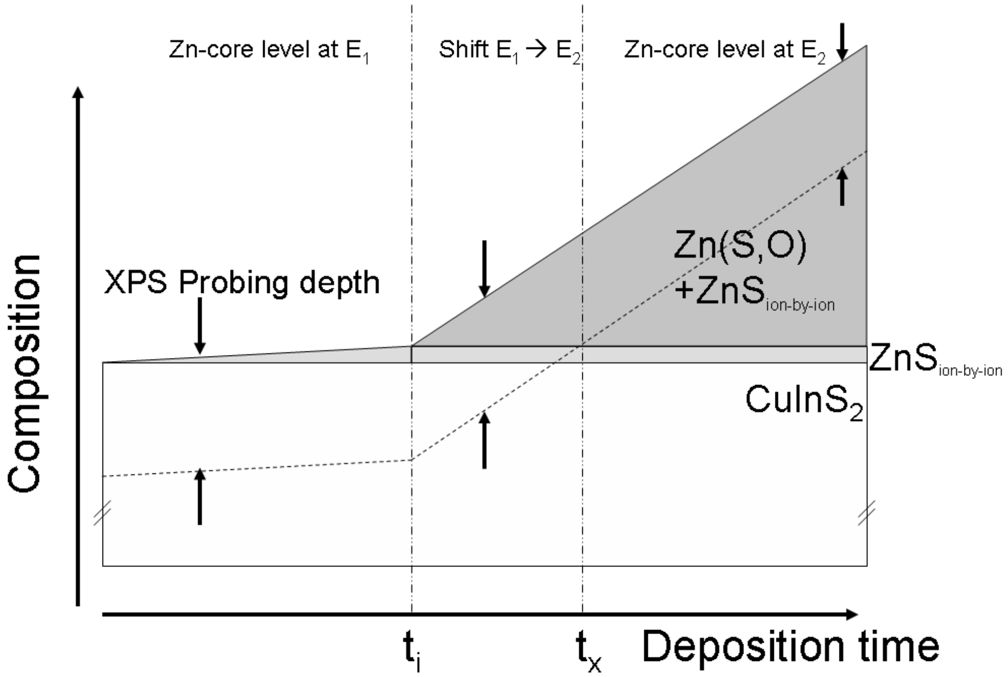

Figure 5.9: schematic representation of a CuInS2/ZnS/Zn(S,O) structure showing the composition of the buffer layer as a function of the chemical bath deposition time. A pure ZnS layer is deposited at a constant rate at all times. For $t > t_i$, an additional Zn(S,O) layer is deposited at a higher rate. The XPS probing depth is also included, assuming the same λ for all layers.

5.2.2 Modified CBD process

The inclusion of an additive in the chemical solution, as explained in section 3.4.3 (page 48), has a major impact in the formation speed of particles (mainly $Zn(OH)_2$ and ZnS aggregates) in the chemical solution. Whether this accelerated process is translated into an enhanced buffer growth rate and what composition this buffer has, are questions that can be investigated using XPS and XAES. Furthermore, the results are compared to those obtained for the buffer layer grown using the standard ZnS CBD (without additive) which were shown in the previous section (5.2.1).

For this study, KCN-etched $CuInS_2$ samples were buffered for different deposition times, namely 90, 120, 180 and 420 seconds (corresponding to transparency values of $\sim$ 95% (90 s), 50% (120 s) and $\sim$ 2% (180 and 420 s)) adding 1% additive to the chemical bath before submerging the samples. After the deposition of the buffer layers, the samples were sealed in a polyethylene bag filled with N_2 and transferred to the analysis chamber. The corresponding transparency curve of the process can be seen in figure 5.10. The formation of detectable particles begins within the first 90 seconds and after 2.5 minutes the transparency is already below 5%.

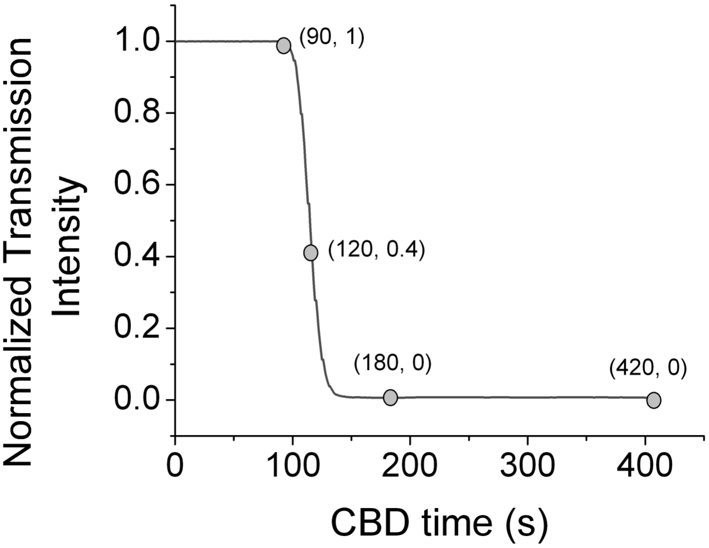

Figure 5.10: Normalized transmission intensity (transparency) graph obtained monitoring a CBD with the inclusion of 1% of additive. Dots indicate times (and transparencies) at which the samples were removed from the chemical bath.

The coverage of the $CuInS_2$ absorber by the deposited buffer layer can also be controlled by investigating the valence band region of the XPS spectra, where the In$4d$ and the Zn$3d$ core levels are visible. In figure 5.11 the measured XPS spectra of the sample series is shown. For the KCN-etched $CuInS_2$ reference (a) only the In4d core level is present. On the other hand, for the samples buffered during 90 (b) and 120 seconds (c), both In$4d$ and the Zn$3d$ core levels are present, which indicates that there is deposition of a zinc-containing layer, but that either this layer is not closed or it is thinner than the information depth of the XPS. According to the investigations regarding the structure of the buffer layer presented in chapter 4 (see figure 4.3) the presence of In- and Cu- related signals in this case is probably due to the fact that the layer is not completely closed. Finally, for deposition times above 3 minutes [(d), (e)] the In$3d$ core level is no longer visible. This means that the $CuIn_2$ absorber is covered by a closed Zn-containing layer with a thickness that exceeds the information depth. As explained in the previous section and assuming that, e.g., the In$3d_{5/2}$ photoelectrons (with a binding energy E_B ≈444 eV) are exclusively attenuated by a pure ZnS layer covering the absorber homogeneously, the thickness of the buffer layer can be estimated to be $\geq 5.4 \pm 1.1$ nm (based on the λ taken from reference [133] and equation (5.5)).

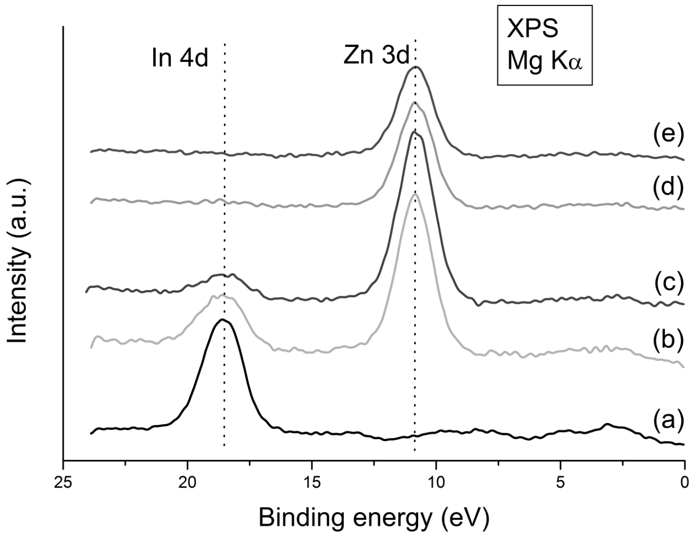

Figure 5.11: XPS detailed spectra of the valence band region, where the In$4d$ and Zn$3d$ core levels of the Zn(S,O) buffer layer deposited on $CuInS_2$ absorbers are shown. The buffer layer deposition times were 90 s (b), 120 s (c), 180 (s) and 420 (s). Additionally, the spectrum of a KCN-etched $CuInS_2$ is also shown (a).

This means that the deposition rate of the buffer layer grown using the additive is higher than in the standard case, where indium and copper related signals were still visible after a buffer deposition time of 9 minutes (see figures 5.3 and 5.5). Thus, the faster precipitation of the particles in the chemical solution obtained when using the additive (figure 3.15), has indeed been translated into a faster deposition of material on the absorber.

The second question corresponds to the thickness-resolved composition of the deposited buffer layer. The qualitative analysis of this composition can be also done by investigating the positions of the Zn$L_3M_{45}M_{45}(^1G)$ Auger peaks, as it was previously done for the buffer layer deposited without any additive (see figure5.4). Figure 5.12 shows the XAES spectra of the buffer/CuInS_2 sample series. It can be seen that there is no shift in the position of the Auger peak for increasing deposition times. No shifts are measured on the Zn$2p_{3/2}$ and the Zn$3d$ core levels. Therefore the same composition is expected for all samples, regardless of the deposition time. Comparing the position of the Zn$L_3M_{45}M_{45}(^1G)$ to the values found on the literature [137, 125] (represented as bars in figure 5.12) a composition of ZnO and/or ZnS is most probable, with only minor amounts of Zn$(OH)_2$.

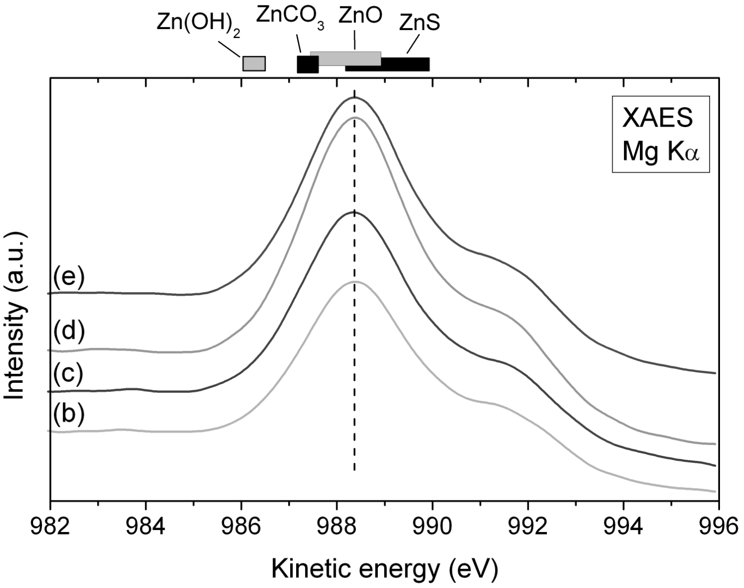

Figure 5.12: XAES detailed spectra of the Zn$L_3M_{45}M_{45}$ Auger peaks as measured on the CuInS_2/buffer sample series: b) 90 s, c) 120 s, d) 180 s and e) 420 s. The energetic positions of the Zn$L_3M_{45}M_{45}(^1G)$ Auger signal for different Zn compounds are additionally given as bars on the upper part of the graph, representing their range of variation found in references [137] and [125]. On cases where only a single value is reported in the literature an error of ±0.2 eV is assumed to represent its uncertainty, as suggested in reference [124].

The composition of the buffer can also be investigated quantitatively, as it was done in the previous case, by examining the Zn$2p_{3/2}$ core level. For this study, the Zn$2p_{3/2}$ photoemission signals can be again fitted using Voigt functions, accounting for two contributions (ZnS and ZnO). The energetic positions of the maxima of the Voigt functions is separated 0.7 ± 0.2 eV and the full width at half maximum FWHM (1.7 and 1.9 eV respectively for the Zn$2p_{3/2}$ core level) is kept constant. This is shown in figure 5.13, where the XPS spectra of the Zn$2p_{3/2}$ core level of the buffe/CuInS_2 series (90 s, 180 s and 420 s deposition time) are presented along with the contributions corresponding to ZnS and ZnO. The addition of both contributions (solid black line) agrees with the measured spectra (bullets).

The ZnS/(ZnS+ZnO) ratio is calculated by using the areas below the fit curves, which describe the contributions of ZnS and ZnO to the total Zn$2p_{3/2}$ spectra. The values determined from the Zn$2p_{3/2}$ photoemission lines are summarized in table 5.5. The ratio of the corresponding areas is an expression of the ZnS/(ZnS+ZnO) ratio. In this case, the ratio is close to 50% for all samples.

Table 5.5: Energetic position of the ZnS (Max 1) and ZnO (Max 2) contributions to the Zn$2p_{3/2}$ photoemission signal together with the area ratio of both contributions (Area 1 and Area 2 respectively). The ratio ZnS/(ZnS+ZnO) is approximately constant with deposition thickeness and can be directly calculated by averaging these values. The ratio is therefore $\sim 51 \pm 2\%$.

Deposition time	Max 1 (eV)	Max 2 (eV)	Area 1(%)	Area 2(%)	R^2
90 s	1022.1	1022.9	50	50	0.999
180 s	1022.2	1022.9	53	47	0.997
420 s	1022.2	1022.9	49	51	0.998

The conclusion of these analyses is that, in contrast with the buffer layer deposited by the standard CBD recipe, the use of the additive results in a Zn(S,O) layer without the initial pure ZnS layer (at least for deposition times above 90 seconds). Additionally, there is no gradient of the oxygen content through the cross-section of the buffer, the ratio ZnS/(ZnS+ZnO) being close to 50% in all samples. The increased oxygen content in the buffer layers deposited using the additive is due to the fact that hydrogen peroxide always decomposes exothermically into water and oxygen gas. ZnS particles can be then oxydized by means of H_2O_2 [141].

These results are also compatible with the model presented in section 5.2.1 (see equations (5.6) and (5.7) and figure 5.8). Figure 5.14 shows the amount of ZnS (deposited by ion-by-ion and cluster mechanism) and ZnO together with the ZnS/Zn(S,O) ratio, considering $k_2 = 50 \cdot k_1$ and the ratio ZnS:ZnO in the Zn(S,O) layer to be 1:1. It can be seen that as soon as the deposition of Zn(S,O) starts, the ZnS/Zn(S,O) ratio tends rapidly to 0.5. Therefore, no shift in the Zn-core levels is found by XPS.

The fact that a single phase material is grown on the absorber enables the calculation of the valence band offset at the absorber/buffer interface. These investigations are not feasible for the standard CBD-deposited ZnS/Zn(S,O) bilayer because, in addition to the band bending in the $CuInS_2$ due to the interface formation process, there is a shift due to a changing chemical environment with buffer layer thickness. These additional chemical shifts make it impossible to determine the buffer's contribution to the overall interface-induced band bending. In order to calculate the valence band offset at the absorber/buffer interface, the sample series is characterized by ultraviolet photoelectron spectroscopy. The results obtained are presented in the following section.

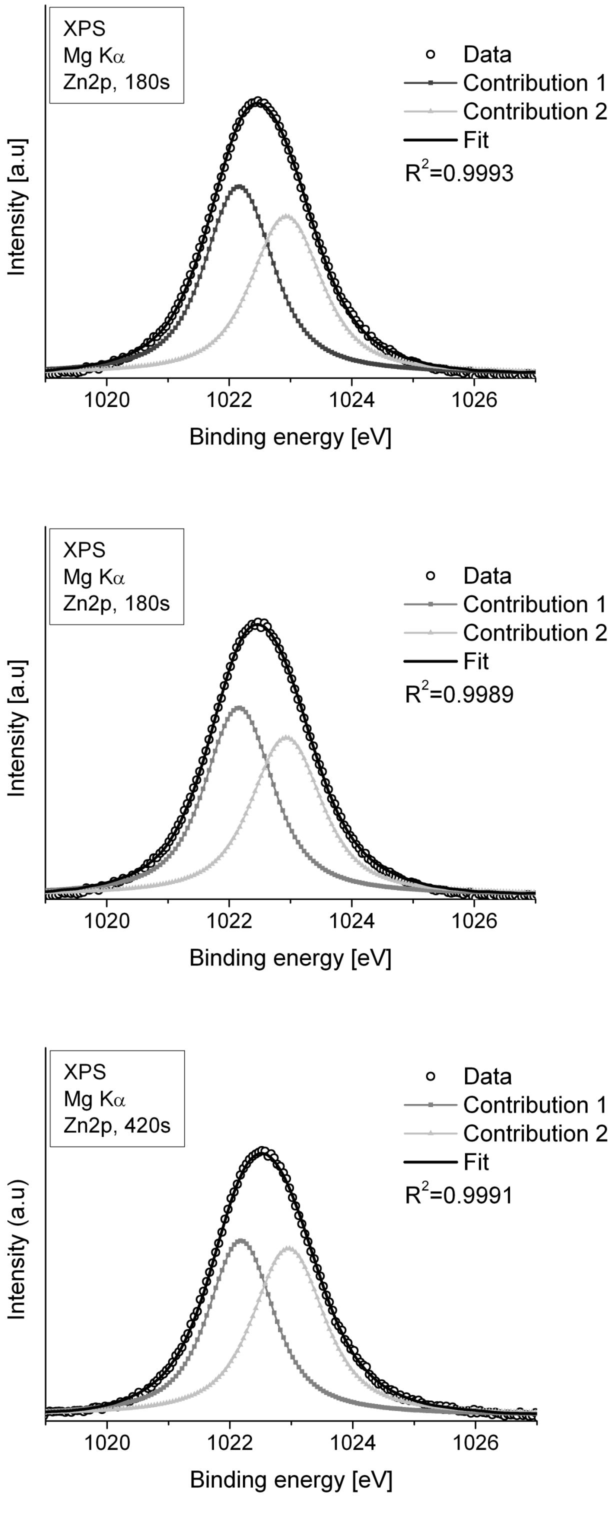

Figure 5.13: XPS spectra of the Zn2$p_{3/2}$ photoemission signals of the buffer/CuInS_2 samples (bullets). The Voigt profiles accounting for the contributions of ZnS (contribution 1) and ZnO (contribution 2), as well as the addition of these contributions are also presented (solid lines).

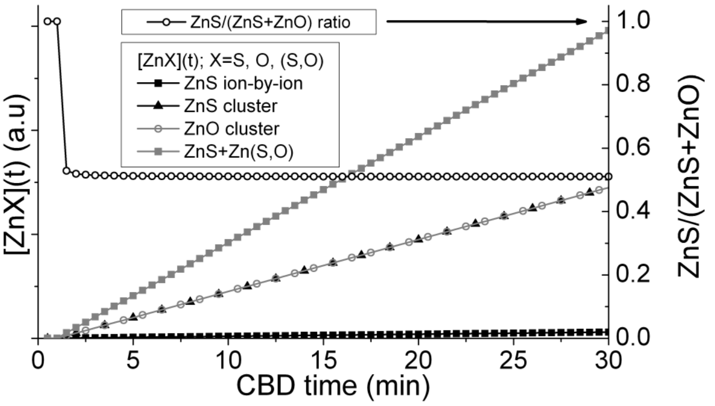

Figure 5.14: Schematic representation of the amount of ZnS (ion-by-ion and cluster mechanisms) and ZnO (cluster mechanism) deposited considering that ZnS is deposited at a constant rate k_1 at all times and a deposition of Zn(S,O) with a ZnS:ZnO ratio of 1:1 at a 50 times higher rate ($k_2 = 50 \cdot k_1$) for $t > t_i$. Additionally, the calculated ZnS/Zn(S,O) ratio as a function of time is also included.

5.3 Summary

The results presented in this chapter have corroborated and extended the conclusion extracted from the study of the structure of the buffer layers by means of electron microscopy:

Standard CBD process: With the results obtained by investigating the microstructure of Zn(S,O) buffer layers on $CuInS_2$ absorbers, it can be concluded that in the early stages of the standard CBD process, which corresponds to the initial plateau in the transparency of the chemical solution measured with the optical sensor, a ZnS layer is formed onto the $CuInS_2$ absorber. No particles are detected by the monitoring system during this stage, meaning that $Zn(OH)_2$ clusters and/or ZnS aggregates have not yet been formed in the solution. Therefore, the growth mechanism during this stage of the deposition process is believed to be an ion-by-ion growth mechanism. Whether the formation of the ZnS layer in this early stage of the CBD takes place between the S^{2-} ions released by the decomposition of thiourea and the Zn^{2+} ions present in the chemical bath or whether at this point there are no S^{2-} ions yet and the sulphur-containing surface acts as a source of anion is not clear.

In the second stage a Zn(S,O) layer is deposited with an increased growth rate. The ZnS/(ZnS+ZnO) ratio decreases gradually from 100% to $\sim$ 80%. After a deposition time of (at the most) 13.5 minutes, this ZnS/Zn(S,O) bilayer buffer covers the rough $CuInS_2$ with a minimal thickness of 5.4±1.1 nm. This increased growth rate occurs in parallel to the decrease of turbidity in the solution and correspondingly with the formation of detectable $Zn(OH)_2$ and ZnS aggragates. Therefore, the main growth mechanism taking place in this stage is believed to be a cluster mechanism, based on the formation of $Zn(OH)_2$ clusters which transform to ZnS as explained in section 3.1.2. Whether the growth mechanisms during the two stages of the process (ion-by-ion in the first, cluster -or hydroxide- based in the second) are simple or complex remains unclear.

Modified CBD process: The inclusion of the additive during the deposition process accelerates the formation of particles in the chemical solution and increases the reaction rate. This is translated into a higher deposition rate on the $CuInS_2$. After 3 minutes of deposition, the absorber is completely covered by a Zn(S,O) buffer layer with a thickness exceeding the information depth of XPS. The buffer layers deposited using the modified CBD process are homogeneous in terms of composition. The deposition of a pure ZnS layer is not detected. The calculated ZnS/(ZnS+ZnO) ratio is $\sim$0.5. The growth mechanism of the chemically deposited buffer layer is expected to be based mainly on a cluster mechanism.

Chapter 6

Study of the $CuInS_2$/Zn(S,O) interface by XPS and UPS

The $CuInS_2$/Zn(S,O) interface constitutes the p-n heterojunction. It is the critical component of the device since its properties and its quality determine the mechanisms that govern the current transport and thus the performance of the device. The two key aspects of the interface are the band alignment between absorber and buffer and the density of interfacial electronic states that may result from the dissimilar crystal lattices of the materials.

The energy band line up characterizes the properties of semiconductors heterojunctions. If two different materials with different properties (e.g. band gaps) are brought together, a certain equilibrium situation results, characterized by the constancy of the Fermi level across the entire device. As a result of this, band offsets will appear at the metallurgical junction, resulting in favourable or unfavourable features for the electronic transport across the junction [142, 30]

The starting point for the theoretical analysis of semiconductor heterojunctions is the Anderson model [143] which assumes an abrupt junction and neglects contributions from interface dipoles and surface states. The key element of the theory is the statement of a common reference level to which all energy levels of each compound are referred to. In the Anderson's model, this common reference level is the vacuum level, which by definition is continuous through the whole device. There are two fundamental parameters that determine the band line up between the semiconductors that form the heterojunction: the electron affinities χ_1 and χ_2 (defined as the energy difference between the bottom of the conduction band and the vacuum level) and the energy band gaps E_{g1} and E_{g2}. When both parameters are known for the materials constituting the heterojuction, the resulting band line up can be in principle inferred from the following calculations:

- The conduction band offset will be determined by the difference of the electron affinities on both sides of the junction:

$$\Delta E_C = \chi_1 - \chi_2 \tag{6.1}$$

- The valence band offset will be determined by:

$$\Delta E_V = (\chi_1 - E_{g1}) - (\chi_2 - E_{g2}) \tag{6.2}$$

This so called electron affinity rule allows to separate the band offset problem from that of the band bending on either side of the junction, which is defined by the doping and the corresponding voltage drop. This separation can be done as long as the electron affinity and the band gap do not depend on the doping concentration (that is, for non-degenerated materials).

In practice, this is a simple picture that fails in fully describing the heterojunction properties. But nevertheless, and based on practical considerations, the model from Anderson will be adopted for the analysis of the $CuInS_2$/Zn(S,O) interface under study. This decision is supported by the following considerations:

- TEM observations reveal a well defined metallurgical junction. There are indications that show that out-leached Cu from the absorber surface forms a $[Zn_{(1-Z)},Cu_{2Z}]$S-like interlayer between buffer and absorber. Furthermore, an incorporation of Zn into the uppermost region of the $CuInS_2$ absorber, where Zn-S bonds are formed, has been observed. A major fraction of the Cu and Zn can be found close to the interface in the buffer and absorber layer respectively, with a calculated spatial extension lower that 0.4 nm [144]*[1]. This further supports the original assumptiom of a well defined metallurgical junction.

- The polycrystalline nature of the semiconductors forming the interface makes unaffordable even the simplest attempts to estimate the contribution of interface dipoles, defect densities and lattice mismatches for every single pair of crystalline surfaces coming in contact. It could be argued that the polycrystallinity may act as a way of neutralizing some of these defects, provided a random distribution of crystallite orientations at the junction plane.

- Anderson's model is invariably used to predict energy band diagrams of semiconductor heterojunctions, and a reasonable agreement between the theory and the experiment is normally found regarding the band offsets [145].

Additionally, Anderson's model was originally enunciated for heterojunctions without interface traps. If interface traps are present equation (6.1) (i.e. $\Delta E_c = \Delta\chi$) is not a valid assumption [28]. However, by choosing ΔE_c as an empirical quantity, the Anderson model remains unaltered [146].

---

[1] References marked with * have Rodrigo Sáez-Araoz as an author and show results related to this work.

Based on this considerations, the approach followed in this section for the study of absorber-buffer heterojunctions will consist in the application of the electron affinity rule for the estimation of the band offsets. The empirical quantity needed to determine ΔE_c will be the band gap of each of the heterojunction partners, as it will be shown in section 6.3

6.1 Ultraviolet photoelectron spectroscopy

Ultraviolet photoelectron spectroscopy (UPS) is particularly useful for the study of valence electrons, as the exciting energy is limited to some tens of eV. Typical sources of UV radiation used in UPS analysis are the He I (21.2 eV) and He II (40.8 eV) lines of a discharge lamp. This method provides a practical way for the measurement of the sample work function. In a metal, the total width of the UPS spectrum "U" is limited by those electrons at the Fermi level (the ones having the highest kinetic energy $E_{kin} = h\nu - \Phi$) and the secondary electrons at the spectrum cut-off (the ones having the lowest energy $E_{kin} = h\nu - \Phi - U = 0$). Therefore:

$$\Phi = h\nu - U \tag{6.3}$$

In the case of semiconducting samples (as the ones studied in this work), the density of states at the Fermi level is negligible compared to that of the valence band. Thus, the UPS spectrum edge at low binding energies does not correspond now to the Fermi level, but to the uppermost valence band. The energy difference between the Fermi level and the uppermost valence band $E_F - E_V$ is also a parameter of interest, since it is related to the effective doping concentration of the sample, according to equation:

$$n = N_C exp(-\frac{E_C - E_F}{kT}) \tag{6.4}$$

where n is the free electron concentration, N_C is the effective density of states at the conduction band edge and E_C is the energetic position of the edge of the conduction band.

6.2 Calculation of the Zn(S,O)/CuInS$_2$ valence band offset

The study of the heterojunction formation between CuInS$_2$ absorber films and CBD-deposited Zn(S,O) buffer layers is carried out by means of X-ray- and ultraviolet- photoelectron spectroscopy measurements (XPS and UPS, respectively) on a the sample series described in section 5.2.2 (page 83). This technique is widely used for the estimation of the valence band offsets at semiconductor heterojunctions. The fact that in the present case the covering species (Zn(S,O)) has a larger band gap than the substrate species (CIS) prevents the application of the so called *direct* method [147, 148] of the valence band offset estimation, based on UPS spectra of the evolution of the valence band (VB) edge as a function of the coverage. The *indirect* method [149] must be then applied in order to take into account the possible band bending induced by the coverage. The reliability of this method has been demonstrated in a number of studies on chalcopyrite materials such as $CuGaSe_2$ [150, 151], $CuInS_2$ [152, 153] or $CuInSe_2$ [154]. This method involves the measurement of the valence band edge of substrate and adsorbate species with respect to the reference position of core levels of each species. The valence band offset is then given by:

$$\Delta E_V = BE_{CL}^{VBM}(CIS) - BE_{CL}^{VBM}(Zn(S,O)) - \Delta E_{CL} \tag{6.5}$$

where BE_{CL}^{VBM} denotes the core level to valence-band maximum binding energy difference of each compound and ΔE_{CL} represents the difference between core level binding energies of pairs of elements from each junction partner at low coverages, when the information depth of the emitted photoelectrons is sufficient to sample both the absorber and the buffer.

Figure 5.11 (page 84) shows a series of XPS spectra of the valence band region of the set of samples for increasing deposition times. In$4d$ core levels are visible in the substrate reference sample (bottom). With increasing deposition time the substrate coverage proceeds on and $CuInS_2$ emissions are gradually replaced by those characteristics from Zn(S,O). In$4d$ emissions are still visible after 120 s of deposition together with the Zn$3d$ peak. The uppermost spectrum (420 s) corresponds to the complete buffer layer, which serves as a Zn(S,O) reference.

In addition to the determination of reference core levels, the application of equations (6.2) and (6.5) for the estimation of the valence band offset between the absorber and the buffer layer requires the determination of the energy of the valence band edge of each compound with respect to the Fermi level. For this purpose, UPS was used, by means of both He I and He II emissions. A gold foil, sputter-cleaned with Ar^+, served as a reference for determining the Fermi level (zero in the abscissa). The energy difference between the valence band edge and the Fermi level was obtained from the linear extrapolation of the leading valence band edge on each sample over the background level. The method provides a resolution of ± 0.1 eV, as inferred from the sharpness of the gold Fermi-edge used as a reference [36]. In a practical case, the resolution is further limited by the curvature of the edge and the choice of the linear extrapolation. The results are shown in figure 6.1. The values of $E_V - E_F = 1.1 \pm 0.15$ eV for CIS and $E_V - E_F = 2.9 \pm 0.1$ eV for Zn(S,O) are calculated.

The obtained value of $E_V - E_F = 1.1$ is in agreement with previously measured valence band offsets with $CuInS_2$ as an heterojunction parter [155]. From simple calculations following equation (6.4) and considering an effective density of states at the valence band of approximately $10^{19}cm^{-3}$ [98], extremely low values ($< 10^2cm^{-3}$) of free charge

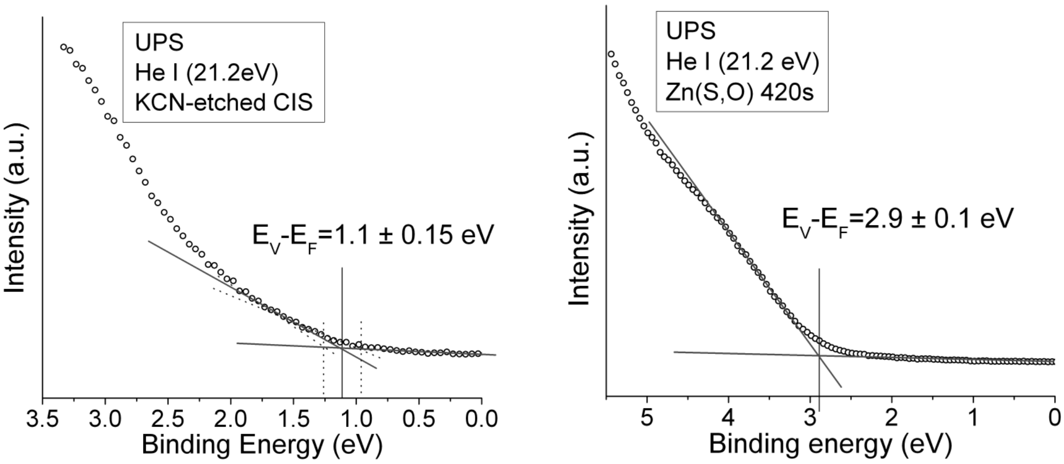

Figure 6.1: Onset of the UPS (He I)-derived valence band edges of a KCN-etched CuInS$_2$ absorber (left) and of a thick Zn(S,O) buffer deposited for 420 seconds (right). Additional lines help to visualize the position of the valence band maxima in both cases showing the linear extrapolation of the band edge. For the KCN-etched sample, the uncertainty of the chosen leading valence band edge is taken into account (boundaries marked as dotted lines) and a corresponding error of 0.15 eV is found. The positions, in energy scale, of the valence band edges are included and referred to the Fermi level.

carriers concentrations are obtained . It is therefore concluded that the position of the Fermi level E_F with respect to the valence band edge at the film surface is substantially different from that expected in the film bulk. Whether this is the result of charge carrier depletion due to the appearance of donor-like surface states, or it should be related to a different phase of dissordered nature at the surface of the absorber remains unclear.

Table 6.1: Energy differences between the core levels and valence band maxima (E$_{CL}$-E$_V$) of CuInS$_2$ (KCN-etched reference) and Zn(S,O) (420 s deposition time) elements. Energy differences between core level pairs from both materials ΔE$_{CL}$(CIS-Zn(S,O)) are also included. These values have been obtained by averaging the differences between the core levels of the samples buffered for 90 and 120 seconds. Finally, the calculated values for each core level pair are presented. The positive sign means an upward shift when transiting from CIS to Zn(S,O). All energies are given in eV.

Core Level	E$_{CL}$-E$_V$	ΔE$_{CL}$(CIS-Zn(S,O))			Core level pairs, ΔE$_V$	
Zn3d	7.9±0.1		Zn3d	Zn2p	In3d/Zn3d	1.7±0.2
Zn2p	1019.6±0.1	In4d	7.7±0.1	-1004±0.1	In3d/Zn2p	1.9±0.2
In4d	17.5±0.1	In3d	434.4±0.1	-577.3±0.1	In4d/Zn3d	1.7±0.2
In3d	444.0±0.1				In4d/Zn2p	1.9±0.2

Values of energy differences between core level binding energies and the valence band edges, as well as energies between core level pairs of both $CuInS_2$ and Zn(S,O) compounds are summarized in table 6.1. An average valence band offset of 1.8±0.2 eV between the $CuInS_2$ absorber layer and the Zn(S,O) buffer layer is found, according to equation (6.5).

A re-characterization of the sample series after annealing in air (200 °C, 5 minutes) enables the investigations of the influence of the heat treatment on the band alignment. The calulations in this case are also based in equation (6.5). The values of the energy differences between core level binding energies and the valence band edges, as well as energies between core level pairs of both $CuInS_2$ and Zn(S,O) compounds are summarized in table 6.2. In this case, an average valence band offset of 1.5±0.2 eV between the $CuInS_2$ absorber layer and the Zn(S,O) buffer layer is found.

Table 6.2: Energy differences between the core levels and valence band maxima (E_{CL}-E_V) of $CuInS_2$ (KCN-etched reference) and Zn(S,O) (420 s deposition time) elements after a heat treatment in air (200 °C, 5 minutes). Energy differences between core level pairs from both materials ΔE_{CL}(CIS-Zn(S,O)) are also included. These values have been obtained by averaging the differences between the core levels of the samples buffered for 90 and 120 seconds. Finally, the calculated values for each core level pair are presented. The positive sign means an upward shift when transiting from CIS to Zn(S,O). All energies are given in eV.

Core Level	E_{CL}-E_V	ΔE_{CL}(CIS-Zn(S,O))			Core level pairs, ΔE_V	
Zn3d	7.5±0.1		Zn3d	Zn2p	In3d/Zn3d	1.5±0.2
Zn2p	1019.1±0.1	In4d	7.7±0.1	-1003.9±0.1	In3d/Zn2p	1.5±0.2
In4d	16.4±0.1	In3d	434.3±0.1	-577.4±0.1	In4d/Zn3d	1.5±0.2
In3d	444.3±0.1				In4d/Zn2p	1.4±0.2

6.3 Estimation of the Zn(S,O)/$CuInS_2$ conduction band offset

Since the photo-generated electrons have to pass through the $CuInS_2$/Zn(S,O) heterostructure in order to be able to contribute to the photocurrent, the conduction band offset is crucial with respect to the performance of the final solar cell device. Thus, the conduction band minimum (CBM) of the $CuInS_2$ absorber surface and on the Zn(S,O) buffer surface was estimated based on the previously calculated valence band maxima (VBM) and the corresponding band gaps of both heterojunction partners, according to equation:

$$\Delta E_C = E_g^{Zn(S,O)} - E_g^{CIS} - \Delta E_V \tag{6.6}$$

The bulk band gap of the CuInS$_2$ is 1.5eV [101]. However, due to the copper-depletion of chalcopyrite surfaces [156, 157], a higher band gap can be expected at the CuInS$_2$ surface (E_g^{surf}). In order to estimate this value, the lower limit will be the bulk value of the band gap. In the case of the related Cu(In,Ga)S$_2$ absorber material with a Ga/(In+Ga) ratio of 0.2, a surface band gap of 1.76±0.15 eV was found [158]. This value of 1.76 eV will be taken as an upper limit for the surface band gap of the CuInS$_2$ absorber under analysis [159]*, although a lower value of the band gap is expected due to the absence of Ga in the CuInS$_2$ samples under study. Therefore, for the following calculations, the surface band gap E_g^{surf} of the CuInS$_2$ absorber layer will be considered to be 1.63±0.15 eV.

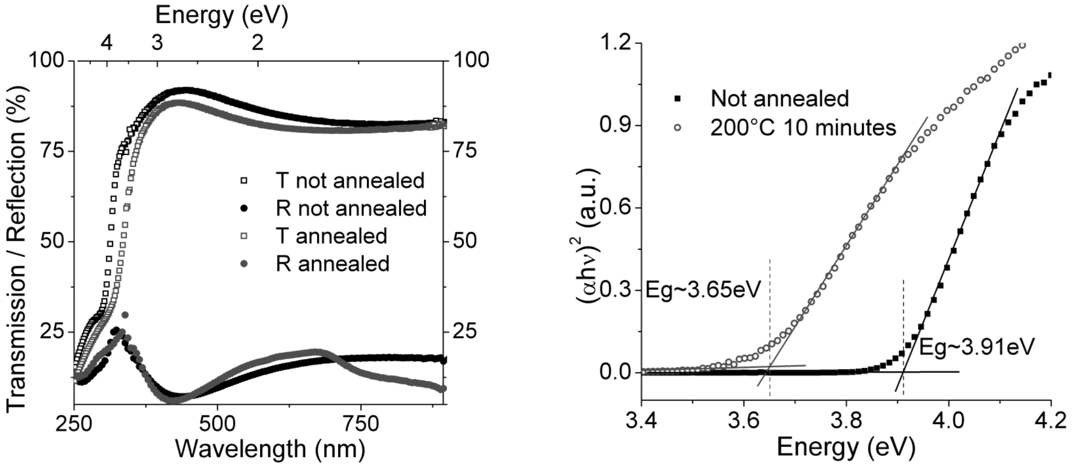

Figure 6.2: Left: transmission and reflection measurements of a glass/Zn(S,O) sample before and after an annealing step in air at 200 °C during 5 minutes. The Zn(S,O) layer was desposited in three consecutive chemical baths. Right: Spectra of the buffer absorption coefficient α (represented as $(\alpha h\nu)^2$) before and after the post deposition annealing step of the glass/Zn(S,O) sample. The linear extrapolations for the determination of the band gaps E_g are also shown.

For the determination of the buffer layer band gap, transmission/reflection spectra of Zn(S,O) deposited on quartz glass substrates are measured with an optical Cary 500 spectrometer with an integration sphere. The spectrometer is capable of measuring from the ultraviolet to the near infrared wavelength region and the measurements are performed before and after a post-deposition heat treatment (5 minutes at 200 °C in air). In order to grow a sufficiently thick sample, the final Zn(S,O) layer was deposited by three consecutive identical chemical baths. Parallel depositions of Zn(S,O) on Glass/Molybdenum and Glass/Molybdenum/CuInS$_2$ substrates are investigated by means of scanning electron microscopy of the respective cross-sections and the thickness of the deposited buffer layer was in both cases close to 100 nm. Since CBD-Zn(S,O) is assumed to be a typical direct semiconductor with a linear correlation between $(\alpha h\nu)^2$ and photon energy $h\nu$, the intersection of the linear extrapolated curve with the abscissa represents the width of the optical band gap [160]. This is shown in figure 6.2, where the transmission and reflection measurements before and after annealing are shown together with the spectra of the buffer absorption coefficient of a glass/Zn(S,O) sample.

One can then substitute the obtained values of the valence band offset and the band gaps of $CuInS_2$ and Zn(S,O) in equation (6.6) to calculate the value of the conduction band offset at the interface and to consequently represent the energy band diagram at the Zn(S,O)/$CuInS_2$ heterojunction[2]. The proposed band diagram is depicted in figure 6.3 for the not-annealed (left) and the annealed samples (right). The valence band offsets agree in both cases with those reported for $CuInS_2$/ZnS/Zn(S,O) heterojunctions. The conduction band offset can be calculated in this case due to the homogeneous composition of the buffer layer deposited using the modified CBD. A value of 0.5 ± 0.3 eV is found in both cases (before and after annealing). In the case of $CuInS_2$/ZnS/Zn(S,O) samples, the conduction band offset was qualitatively studied and resulted also in a spike-like offset [159]*. The additional band bending in the CIS absorber measured after annealing supports the model of formation of Zn_{Cu}^{+} states at the absorber's surface as a result of a CBD-induced and heat treatment promoted Cu-Zn intermixing at the Zn(S,O)/$CuInS_2$ interface, as suggested in [144]*.

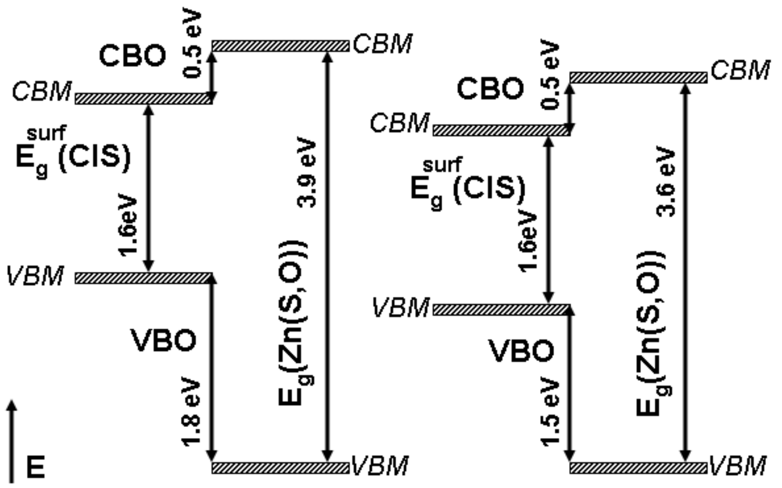

Figure 6.3: Determined energy band diagram at the Zn(S,O)/CIS heterojunction before (a) and after an annealing step is air, at 200 °C for 5 minutes.

The band alignment between a chalcopyrite material and nominal ZnS layers has been a matter of study in several groups. Table 6.3 shows the literature data regarding valence and conduction band offsets of chalcopytite/ZnS structures.

Pure ZnS buffer layers deposited by ALD or evaporation result in high spike-like conduction band offsets between the absorber and the buffer layer. These offsets are reduced if oxygen is included in the composition, leading to an improvement of the performance of the solar cells. According to device simulations [29], for spike-like conduction band off-

---

[2] It is assumed that the surface band gap of the absorber does not change after the heat treatment [159]*.

Table 6.3: Literature data regarding band alignment between a chalcopyrite material and a nominal ZnS buffer layer deposited on the substrate by atomic layer deposition (ALD), evaporation or chemical bath deposition. Additionally, efficiencies of related solar cells is also included.

Absorber	Buffer	Method	VBO (eV)	CBO (eV)	η (%)
CIGSe	Zn(O,S)10%[26]	ALD	1.65	0.2	13.6
CIGSe	Zn(O,S)20%[26]	ALD	1.25	0.7	13.5
CIGSe	ZnS[26]	ALD	1.19	1.21	11.3
CIGSe	Zn(S,O,OH)[161]	CBD	0.8	1.0	16.5
CIGSe	ZnS[161]	Evaporation	1.4	1.6	/
CIS(HZB)	ZnS/Zn(S,O)[159]*	CBD	1.51	> 0	11.4
CIS(SCG)	Zn(S,O)(this work)	CBD	1.5	0.5	8.5

sets higher than 0.5 eV, the efficiency decreases due to a drop of the short circuit current, as a result of the large barrier for photogenerated electrons.

6.4 Summary

In this chapter, the interface between $CuInS_2$ and CBD-deposited Zn(S,O) has been studied by means of XPS and UPS, based on Anderson's model. The valence band offset obtained using the modified CBD to deposit the buffer layer corroborates that previously reported for ZnS/Zn(S,O) bilayers. After annealing, an increased band bending in the CIS absorber was obtained, supporting the model of formation of Zn_{Cu}^{+} states at the interface. The fact that the Zn(S,O) buffer layer deposited using the modified CBD exhibits a homogeneous composition allows the calculation of the conduction band offset at the absorber/buffer interface. The resulting spike-like conduction band offset of 0.5 eV is mantained after annealing. According to device simulations, conduction band offsets below 0.6 eV are compatible with efficient devices.

Chapter 7

Photovoltaic performance of Zn(S,O) buffered solar cells

Once several aspects of the chemically deposited buffer layer, such as the growth, composition and microstructure, have been characterized, the next step is the study, in terms of their photovoltaic performance, of Zn(S,O) containing thin film devices. The evaluation of the photovoltaic performance of Zn(S,O)-buffered thin film solar cells has been carried out by means of current-voltage analysis under different temperatures and illumination intensities. This technique provides detailed information about the electronic transport mechanism governing the performance of the device under analysis, as well as a direct measurement of the photovoltaic parameters, namely the open circuit voltage (V_{oc}), the short circuit current (I_{sc}) and the fill factor (FF). The knowledge of these parameters and of the irradiation power enables the calculation of the efficiency of the solar cell. In the following section, the results of the characterization of single cell devices (0.5 cm^2 area) will be presented. The results on larger areas (up to 30 cm x 30 cm) will be shown in chapter 8.

7.1 Characterization methods

current-voltage J(V) characteristics have been obtained using two different set-ups, a continuous light sun simulator and the J(V,T) set-up. Their main features will be briefly reviewed in the following:

7.1.1 Sun simulator

A continuous light sun simulator working under standard test conditions is used to characterize the PV-parameters of the photovoltaic device under study. The use of the standard test conditions is important in order to obtain world-wide comparable results. In all cases the temperature of the cell is $25\,^{\circ}\mathrm{C}$. For measurements performed under illumination, the radiation power must be 100 mW/cm^2 and the light spectra should simulate, as closely as possible, that of the sun at AM1.5G[1]. In the experimental set up, the temperature is controlled by means of a thermostat set at $23\,^{\circ}\mathrm{C}$ and considering that the temperature of the cell is $\sim 2\,^{\circ}\mathrm{C}$ higher than that of the sample holder. The spectral content of the light is determined by the use of a halogen lamp (JQ324/04) and a xenon lamp (KX0 1000 HSDF) with a power of 120 W and 100 W respectively, together with optical lenses inside the sun simulator. The radiation power is calibrated regularly by means of a silicon reference solar cell, whose current output as a function of the light input and temperature is known. In this case, the temperature of the silicon solar cell is controlled by monitoring the series resistance at the probes. Once the value of the resistance is stabilized at 109.7 Ω, an output current of 141.7 mA is equivalent to a radiation intensity of 100 mW/cm^2. Figure 7.1 shows the spectral irradiance of the sun simulator used during this work together with the AM 1.5 reference spectrum. The calibration procedure is done every 40 working hours to check the aging of the lamps. The halogen lamp is changed every 80 working hours, while the xenon lamp can last up to 1000 hours. J(V) measurements are performed in the four-probe configuration in order to reduce the influence of the contact series resistance. One pair of needle probes is connected to the Mo back contact and a second one to the front contact (Ni-Al grids in the case of 0.5 cm^2 single cells). Both pairs are connected to the measuring unit (Keithley SMU 238), which generates the voltage and measures the corresponding current, as specified in a computer program.

Temperature-dependent J(V) analysis

The current-voltage characterization as a function of temperature -J(V,T)- is performed inside a cryostat provided with a quartz window that allows for illumination. The sample holder is a hollow piece of steel which may be flooded with liquid nitrogen if refrigeration is needed. The cryostat is evacuated with a turbo pump after the sample has been mounted. The temperature is controlled by a thermocouple and governed by an electrical heater. The usual temperature range of analysis extends from 150 K to 350 K in steps of 10 K. J(V) curves can be recorded for different illumination intensities I_{ilu}, with 0.00005$\leq I_{ilu} \leq 1$, being I_{ilu}=1 approximately the $AM1.5G$ reference. For this purpose, a rotating neutral filter wheel is located between the lamp and the cryostat quartz window. As in the case of the sun simulator, samples are contacted in the four-point-probe configuration and the measuring unit (Keithley SMU 238) generates the voltage and measures the current. The sample is illuminated by a single halogen lamp and there is a shutter for switching from dark to illuminated measurements. The fact that a single halogen lamp is used leads to differences in the spectral content when compared to the measurements performed in the sun simulator. The mismatch is partly compensated by adjusting the short circuit

---

[1] The standards are characterized by the so-called air mass (AM), equivalently the optical path of the real sun light when crossing the terrestial atmosphere before reaching the sample, and the kind of radiation incidence impinging on it, either direct (D) or global (G), which includes also scattered light. This work will only refer to the standard AM1.5G spectrum. Further details and numerical values can be found in Ref [37].

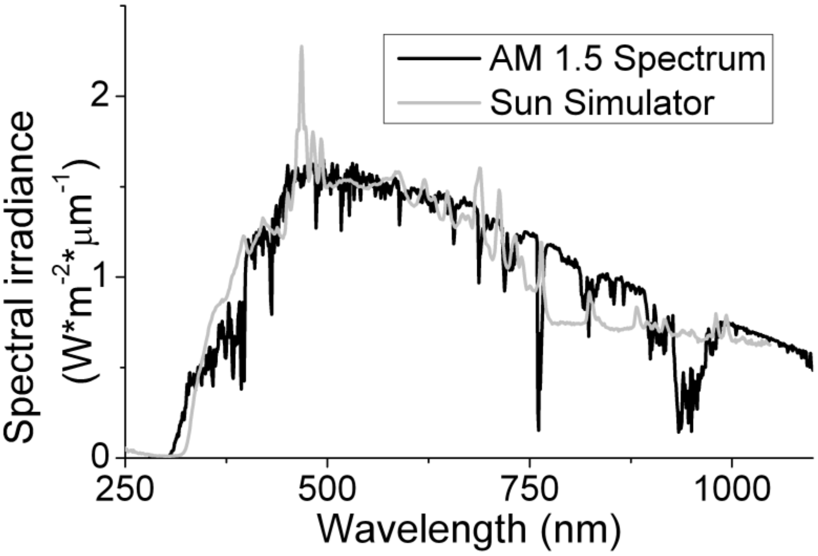

Figure 7.1: Spectral irradiance of the sun simulator used for the J(V) characterization in this work, compared to the reference AM 1.5 spectra.

current as measured in the J(V,T) set up to the value obtained in the sun simulator. This ensures that the same current is flowing through the device as in the standard conditions. Nevertheless, the absolute values of the PV parameters as recorded in the J(V,T) set up are only approximate, and their full meaning can be evaluated in a relative scale when comparing measurements under different illuminations.

7.2 J(V,T) analysis of Zn(S,O) buffered devices

Current-voltage characteristics as a function of temperature have been measured on Zn(S,O) buffered devices based on both $CuInS_2$ and $Cu(In,Ga)(S,Se)_2$ absorbers. Different recombination mechanisms seem to govern the performance of the device for the case of low band gap and wide band gap absorbers. In the case of $CuInS_2$ absorbers, samples buffered using the standard CBD process and the process including the additive (see section 3.2 and 3.4.3) have been characterized in order to find out if the inclusion of the additive that leads to an increase of the deposition rate and therefore to a reduction of the processing time has any impact in the recombination mechanisms that control the current transport. A detailed summary of the basics of recombination mechanisms is found in Appendix B.

J(V) curves measured in the dark are fitted using equation (2.2). On the other hand, a direct analysis of the J(V) curves measured under illumination according to equation (2.2) would lead in this case to erroneous parameter values, since it assumes that photogenerated current density J_L does not depend on the biasing conditions. A way of circumventing this problem includes the measurement of illuminated J(V) curves as a function of different illumination intensities. If equation (2.2) is written at open-circuit conditions $(J(V_{oc}) = 0)$ and assuming that the photogenerated current density is the short-circuit current density $(J_L = J_{sc})$:

$$J_{sc} = J_0 \left(exp \left(\frac{qV_{oc}}{AkT} \right) - 1 \right) + \frac{V_{oc}}{R_p} \tag{7.1}$$

This provides a direct relationship between the short-circuit current density and the open-circuit voltage of the solar cell. Different illumination intensities for a given temperature provide different points fulfilling equation (7.1), which preserves the qualitative J(V) dependence of the dark curve. This means that the fitting procedure remains valid and that any change in the electronic transport mechanism governing the performance of the device will in turn be translated into a change in J_0 and A, when compared to the values obtained by fitting the dark characteristic.

The $J_{sc}(V_{oc})$ plot resembles the behaviour of the dark J(V) characteristic (figure 2.6) in the forward bias range, excluding region IV, where the effect of the series resistance, explicitly eliminated from equation (7.1) at open circuit conditions, is most notable. Therefore, the standard analysis of illuminated J(V) curves will be referred to as $J_{sc}(V_{oc})$ in this work.

7.2.1 Ideality factor and activation energy

The discussion of the different recombination mechanisms will be based on the study of the diode ideality factor (A) and the activation energy (E_A) of the saturation current density (J_0). As a brief summary, the recombination current density can be generally expressed for the various recombination mechanisms detailed in Appendix B as:

$$J_R = J_0 exp \left(\frac{qV}{AkT} \right) = J_{00} exp \left(\frac{-E_A}{AkT} \right) exp \left(\frac{qV}{AkT} \right) \tag{7.2}$$

where J_{00} is a pre-factor. A method used to obtain the activation energy of the saturation current density from dark and illuminated J(V) curves is to re-write equation (7.2) as:

$$AlnJ_0 = \frac{-E_A}{kT} + Aln(J_{00}) \tag{7.3}$$

Considering that the dependence of the pre-factor J_{00} on the temperature is very weak [162], if A is not strongly temperature dependent, a plot of $AlnJ_0$ versus $1/T$ (an Arrhenius plot) yields a straight line [163]. From the slope of the straight line the activation energy can be found [164].

In cases where the diode quality factor depends strongly on the temperature (i.e. tunneling enhanced recombination processes), the analysis of the activation energy using equation (7.3) is not possible [163].

The temperature dependence of the saturation current density and the diode quality factor give hints regarding the dominant recombination mechanism in the solar cell. From the value of the activations energy, information about where the recombination is taking place can be found. If $E_A \neq E_g^{absorber}$ the recombination takes place at the interface. If the activation energy matches the value of the band gap of the absorber, the place cannot be unambiguously determined, although in most cases, the corresponding recombination mechanism can be tracked back to the space charge region [165]. For a more detailed description of the different recombination mechanisms in a pn-heterojunction device, the reader is referred to Appendix B.

7.2.2 Cu(In,Ga)(S,Se)$_2$/Zn(S,O) devices

Zn(S,O)-buffered Cu(In,Ga)(S,Se)$_2$ devices have been characterized by means of temperature dependent J(V) measurements in order to find out which are the recombination mechanisms that govern the performance of the device in the dark and under illumination. For this purpose, Cu(In,Ga)(S,Se)$_2$ absorbers (5x5 cm^2) are buffered using the standard CBD process. Samples are removed out of the bath when the transparency of the solution reaches 80%, 40%, 20% and 9% of the initial value, which corresponds to deposition times of approximately 11.5, 15, 18 and 21 minutes respectively. After the desposition of the buffer layer, solar cells are completed by sputtering the window layer and evaporating contact grids for better current collection. In addition, one sample without any buffer layer is also processed for comparison. The performance of single cells (0.5 cm^2 total area) where characterized by means of the sun simulator operating under standard test conditions. The average PV-parameters (and corresponding standard deviations) of the twelve single cells located in the center of the 5x5 cm^2 samples (to avoid possible non-homogeneities introduced during the cleaving of the absorber or from shadowing effects of the sample holder in the CBD), are presented in table 7.1. Additionally, the PV parameters of one single cell (transparency of the chemical solution = 22%) measured under standard test conditions, together with the fitting parameters extracted from the analysis of the dark J(V) characteristic at 300 K (see equation (2.2)) are included in table 7.2.

While results with no buffer layer show very low values in all PV parameters, in the case Zn(S,O)-buffered devices, high performances are achieved even for high transparency values, i.e. short deposition times. XPS studies of In$4d$ and Zn$3d$ core levels reveal that for these short CBD processes, the Cu(In,Ga)(S,Se)$_2$ absorber layer is either not completely covered or is covered by a layer not exceeding the escape depth [108]. This may account for the larger standard deviations observed in the open circuit voltage for samples buffered during 11.5 minutes (80% transparency) when compared to those samples which stayed longer in the chemical bath. Best efficiencies are obtained for the sample buffered during 18 minutes (22% transparency). In this case HR-TEM and XPS-XAES investigations show the formation of a bi-layer, starting with a thin (3-4) nm pure ZnS layer followed by a nanocrystalline Zn(S,O) layer (see chapters 4 and 5), with a total thickness of 20 nm.

Table 7.1: Average PV parameters and standard deviation of twelve Mo/Cu(In,Ga)(S,Se)$_2$/Zn(S,O)/ZnO single cells buffered for 11.5 minutes (80% transparency), 15 minutes (40% transparency), 18 minutes (22% transparency) and 21 minutes (9% transparency). For the case of the sample buffered during 18 minutes, the values of A, J_0, R_s and R_p extracted from the fit of the dark J(V) characteristic at 300K are also shown. V$_{oc}$ is given in mV, J$_{sc}$ and J_0 in mA/cm^2, the fill factor (FF) and the efficiency (η) in % and R_p and R_s in Ω·cm^2

Sample	V$_{oc}$	J$_{sc}$	FF	η
No buffer	283±6	26.3±1.1	32.1±0.7	2.4±0.2
80% Transparency	524±11	37.5±0.6	57.6±1.5	11.3 ±0.2
40% Transparency	561±7	37.9±1.4	58.6±2	12.5 ±0.6
22% Transparency	569±2	38.2±1	58.9±3.2	12.7±0.9
Best cell	570	38.9	62	13.7
9% Transparency	569±1	37.7 ±0.6	58.1±2.8	12.5 ±0.5

One single cell from the previously described sample (22% transparency) was additionally characterized by J(V,T), performing J(V) measurements in the temperature range from 320 K to 200 K in steps of 10 K. The resulting fitting parameters obtained at 300K (A, J_0, R_p and R_s are summarized in table 7.2. The dark-J(V) and $J_{sc}(V_{oc})$ plots, as a function of temperature, are shown in Figure 7.2. The inset of figure 7.2 a) shows the dark-J(V) characteristic at 300 K and the corresponding fit using the one diode model previously described (see equation (2.2).

Table 7.2: Values of A, J_0, R_s and R_p corresponding to the best cell (see table 7.1) extracted from the fit of the dark J(V) characteristic at 300K. J_0 in mA/cm^2, and R_p and R_s in Ω·cm^2

A	J_0	R_p	R_s
1.74 ± 0.01	$6.6 \cdot 10^{-8} \pm 2 \cdot 10^{-9}$	1002 ± 8	2.7 ± 0.1

Having measured the dark J(V) curves in the selected temperature range, the temperature dependence of the diode ideality factor is found by fitting the linear region in figure 2.6 (region labeled III). Since the $J_{sc}(V_{oc})$ plot resembles that of the dark J(V) in regions II and III, i.e, the forward bias excluding the effect of the series resistance, a similar procedure is followed to study the temperature dependence of the diode ideality factor under illumination. The results are shown in figure 7.3 (left). Both in the darkness and under illumination, the diode ideality factor remains between 1.5 and 2, pointing to a thermally activated recombination process in the temperature range under analysis. The slight temperature dependence can be modeled using equation (B.9), as shown in Appendix B. The fit is also included giving a characteristic energy of the exponentially distributed recombination centers of 130±12 meV. The value obtained by fitting the temperature dependence

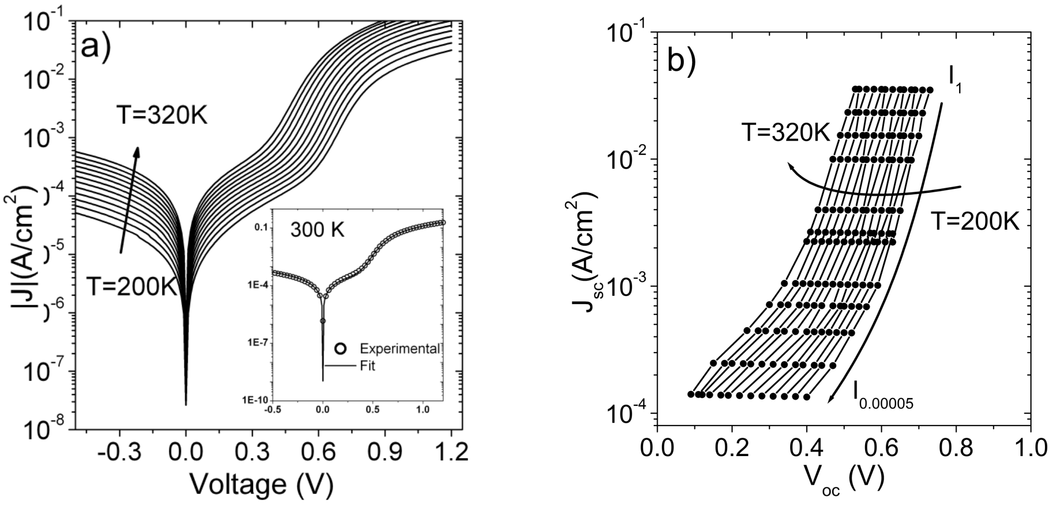

Figure 7.2: J(V,T) analysis of a Cu(In,Ga)(S,Se)$_2$/Zn(S,O) solar cell. a) Semilogarithmic plot of the absolute J(V) dark characteristics as a function of temperature (320-200 in steps of 10 K). In the inset, the one diode model based fitting obtained for the characteristic measured at 300 K is shown (for the values of the fitting parameters see table 7.1. b) Semilogarithmic plot of experimental $J_{sc}(V_{oc})$ characteristics for different values of temperature and light intensity.

of A in the dark lies within the error of the former one and it is not included in the graph for the sake of clarity. The corresponding activation energies are obtained from a linear fit of the modified Arrhenius plot (equation (7.3)). This is shown in figure 7.3 (right). In both cases, values of the activation energy of 1.1 eV are obtained. This value is close to the value of the bulk energy band gap of the Cu(In,Ga)(S,Se)$_2$ absorber (approximately 1.08eV, as determined from quantum efficiency measurements [108]), which means that the recombination in this device, in the darkness as well as under illumination, takes place probably in the space charge region and are not dominated by recombination processes at the interface. This is a necessary requirement to obtain high efficiency devices [30].

The determined behaviour of Zn(S,O)-buffered Cu(In,Ga)(S,Se)$_2$ solar cells, namely the thermally activated recombination in the space charge region in the temperature range under investigation, agrees well with the behaviour determined for CdS-buffered references [166] and keeps the path open for the replacement of CdS buffer layers by Zn(S,O) in Cu(In,Ga)(S,Se)$_2$-based thin film solar cells.

Reagarding the photovoltaic performance under standard test conditions measured at the sun simulator, the highest conversion efficiency reached within this work by a Zn(S,O)-buffered Cu(In,Ga)(S,Se)$_2$[2] single cell (0.5 cm^2) is 15.1%. The corresponding PV parameters and the current voltage curve are shown in figure 7.4.

---

[2] Absorber material from an industrial pilot line delivered by AVANCIS GmbH & Co. KG.

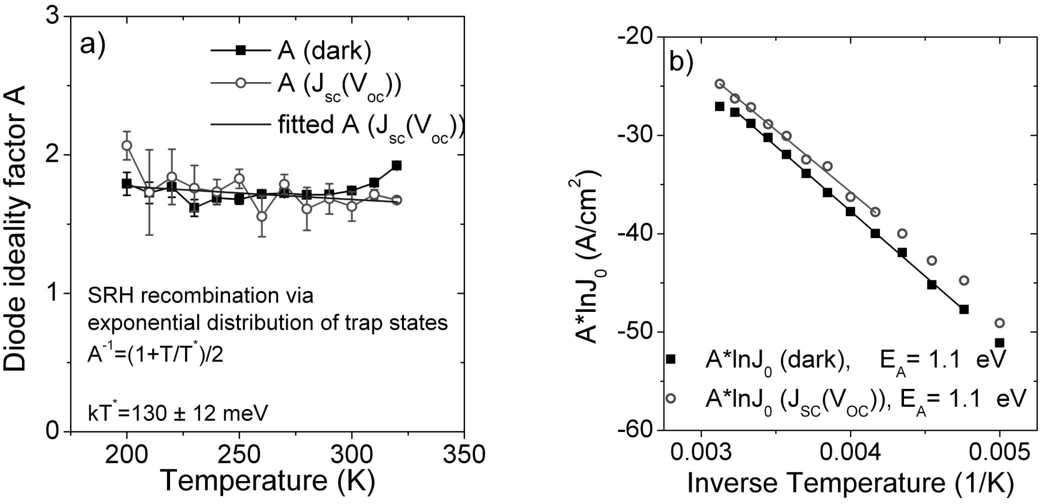

Figure 7.3: a) Temperature dependence in the dark and under illumination of the diode quality factor of a Cu(In,Ga)(S,Se)$_2$/Zn(S,O) solar cell. The linear fit of A for the measurement performed under illumination is included. b) Corrected Arrhenius plot of the saturation current density over the inverse temperature in the dark and under illumination. The corresponding activation energies obtained from the linear fit of the curves are also given.

7.2.3 CuInS$_2$/Zn(S,O) devices

In order to investigate the performance of solar cell devices by means of J(V,T), CuInS$_2$ absorbers are buffered using the standard CBD and the modified process using the additive previously described. The deposition times are 30 minutes for the standard process and 5 minutes for the modified process using additive. The substrate size is chosen to be one square inch and from each substrate eight single cells with a total area of 0.5 cm^2. The performance of each cell is measured at the sun simulator under standard test conditions and from each substrate, the best cell is investigated by means of J(V,T) for temperatures ranging from 320 to 200 K in steps of 10 K. Table 7.3 summarizes the PV-parameters measured at the sun simulator of the cells characterized by means of J(V,T). No significant differences can be observed between the two sets of parameters.

The measured dark-J(V,T) characteristics and $J_{sc}(V_{oc})$ plots are shown in figure 7.5 for both analyzed cells. The graphs in the upper side correspond to the cell buffered with the standard CBD process, while the graphs located on the bottom side correspond to the cell buffered using the additive. The fittings obtained applying the one diode model to the dark J(V) characteristic measured at 300 K can be seen in the inset of the corresponding figures (top left for the standard CBD and bottom left for the CBD including additive). The fitting parameters A, J_0, R_s and R_p are summarized in table 7.4. In both cases, the diode ideality factors show values above 2, pointing to a tunneling assisted recombination

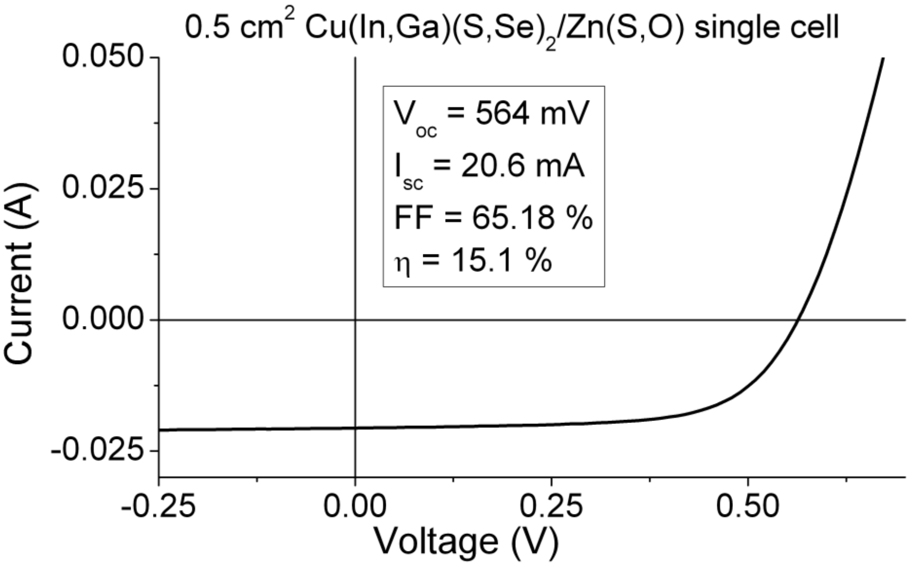

Figure 7.4: Current voltage curve of a Zn(S,O)-buffered Cu(In,Ga)(S,Se)$_2$ single cell (0.5 cm^2) showing the highest conversion efficiency obtained within this work. The corresponding PV paramenters are included.

mechanism at this temperature. Relatively high are the values of the series resistance, in good agreement with the relatively low values of the fill factor (see table 7.3).

The J(V,T) analysis (both in the dark and under illumination) of the CuInS$_2$/Zn(S,O) solar cells under study, deliver similar results. For both the standard buffer layer and the layer grown with the inclusion of the additive the temperature dependence of the dark J(V) characteristics and the $J_{sc}(V_{oc})$ plot are very similar. The similar behaviour at lower voltages (V<0.4) and the differences between the dark and light behaviour at higher voltage are clearly seen. The shape of the $J_{sc}(V_{oc})$ plot do not resemble that of the dark characteristics. This points to a light-induced difference in the recombination mechanism. This phenomenon has been documented earlier for CdS-buffered CuInS$_2$ absorbers, although

Table 7.3: PV parameters of 0.5 cm^2 CuInS$_2$/Zn(S,O) single cells investigated by means of J(V,T). The different CBD processes (standard and with additive) are explained in sections 3.2 and 3.4.3. V$_{oc}$ is given mV, J$_{sc}$ in mA/cm^2, and the fill factor (FF) and the efficiency (η) in %.

Process	V$_{oc}$	J$_{sc}$	FF	η
Standard	654	21	54.3	7.5
Additive	657	21.3	52.3	7.4

Table 7.4: Fitting parameters A, J_0, R_s and R_p obtained by applying the one-diode model to the dark-J(V) characteristic of the $CuInS_2$/Zn(S,O) cells under study at a temperature of 300 K. J_0 is given in mA/cm^2, and the parasite resistances R_s and R_p in $\Omega \cdot cm^{-2}$. The different CBD processes (standard and with additive) are explained in sections 3.2 and 3.4.3.

Process	A	J_0	R_s	R_p
Standard	2.28±0.01	$(2.9\pm0.2)\cdot10^{-8}$	4.3±0.1	1134±12
Additive	2.03±0.01	$(9.5\pm0.4)\cdot10^{-9}$	5.7±0.1	2087±15

this is not the case in $CuGaSe_2$ or $CuInSe_2$ [167], nor for Cu(In,Ga)$(S,Se)_2$ (see figure 7.2 and the discussion above).

The behaviour of the diode ideality factor A with decreasing temperature is similar for both cells, but differs from dark to illuminated conditions. The high values ($A > 2$) and temperature dependency of the diode ideality factors in the dark point to a tunneling enhanced recombination. An evaluation of the activation energy of the saturation current density following (7.3) is therefore not possible. Under illumination, A remains slightly temperature dependent and an evaluation of the activation energy $E_A$is possible by plotting the product of the ideality factor with the logarithm of the saturation current density $AlnJ_0$ as a function of inverse temperature (modified Arrhenius plot), as shown in figure 7.6. The results obtained for the $CuInS_2$ processed with the standard CBD are found in the upper side of the graph, and those obtained with the additive in the lower. For both CBD processes (standard and with additive) the recombination in the dark seems to be dominated by tunneling, since the diode ideality factor remains above 2 and shows the characteristic temperature dependence. This dependence can be modeled using equation B.15.

The resulting values of the characteristic temperatures are included in the graphs. The cell buffered using the standard CBD process shows a stronger contribution of tunneling. On the other hand, under illumination, the diode ideality factor remains approximately constant with values below 2, pointing to a thermally activated recombination process. In order to determine the location at which the dominant recombination mechanisms are taking place, the evaluation of the activation energy from the modified Arrhenius plot is necessary. For both cells under study, the activation energy of the saturation current density is approximately 1 eV, lower than the value of the absorber's band gap. Therefore, under illumination, a thermally activated recombination mechanism at the interface between the buffer and the absorber is predicted.

As in the previously discussed case of Cu(In,Ga)$(S,Se)_2$/Zn(S,O) devices, Zn(S,O)-buffered $CuInS_2$ absorbers show similar dominant recombination mechanism as in the case of CdS-buffered references [167]. These results support the feasibility of the Zn(S,O) buffer layer studied in this work to replace the reference CdS buffer in state of the art chalcopyrite-based thin film devices. Furthermore, the inclusion of the additive, which

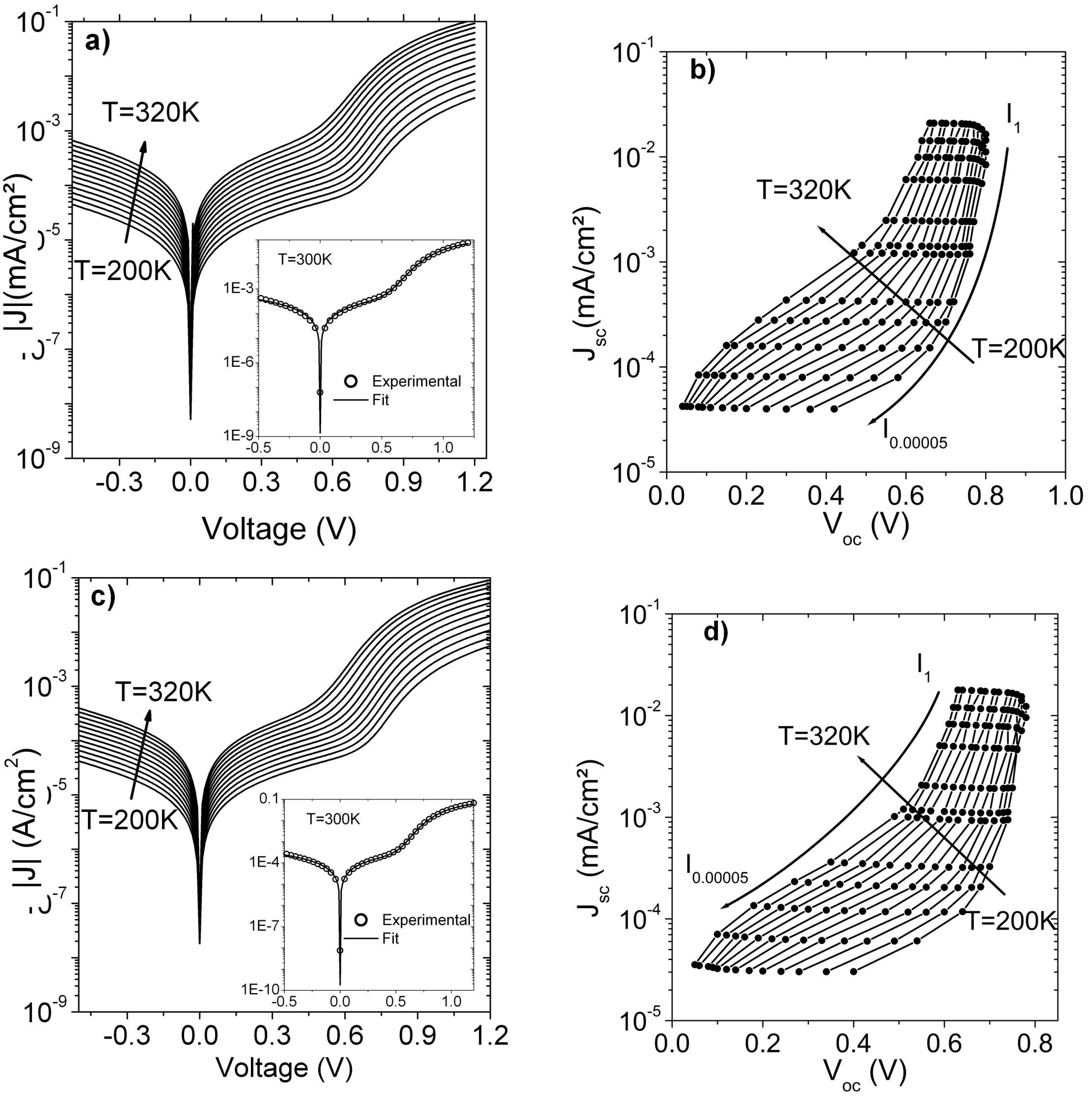

Figure 7.5: J(V,T) analysis of CuInS$_2$/Zn(S,O) solar cells buffered with the standard CBD process -a) and b)- and with additive -c) and d)-. The graphs on the left side -a) and c)- show the semilogarithmic plots of the absolute J(V) dark characteristics as a function of temperature (320-200 in steps of 10 K). In the insets, the one diode model based fitting obtained for the characteristic measured at 300 K is shown. The graphs on the right side -b) and d)- show the semilogarithmic plots of experimental $J_{sc}(V_{oc})$ characteristics for different values of temperature and light intensity.

enhances the deposition rate, does not have any harmful impact on the transport properties of the studied devices which in turn makes the modified CBD process, a feasible replacement of the standard one in order to reduce the deposition time.

Reagarding the photovoltaic performance under standard test conditions measured

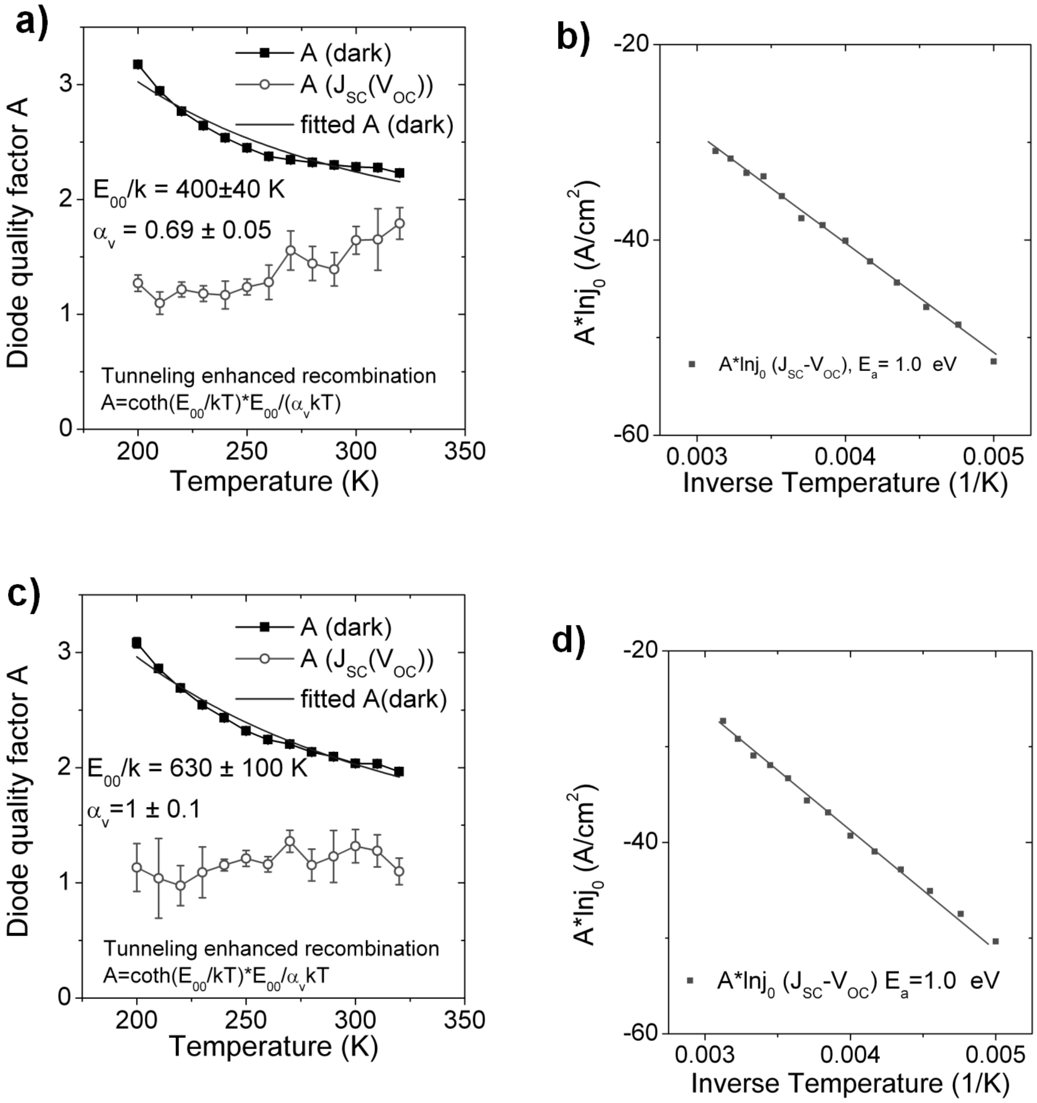

Figure 7.6: J(V,T) analysis of $CuInS_2$/Zn(S,O) solar cells buffered with the standard CBD process -graphs a) and b)- and with additive -graphs c) and d)-. Graphs a) and c) show the temperature dependence in the dark and under illumination of the diode quality factor. Graphs b) and d) show the corrected Arrhenius plots of the saturation current density over the inverse temperature in the dark and under illumination. The corresponding activation energies obtained from the linear fit of the curves are also given.

at the sun simulator, the highest conversion efficiency reached within this work by a Zn(S,O)-buffered $CuInS_2$[3] single cell (0.5 cm^2) is 8.5%. On laboratory scale $CuInS_2$ absorbers provided by the technology department at the Helmholtz Zentrum Berlin the

---

[3] Absorber material from an industrial production line delivered by Sulfurcell Solartechnik GmbH.

highest conversion efficiency achieved has been 11.4% [168]*[4]. The corresponding PV parameters and the current voltage curve are shown in figure 7.7.

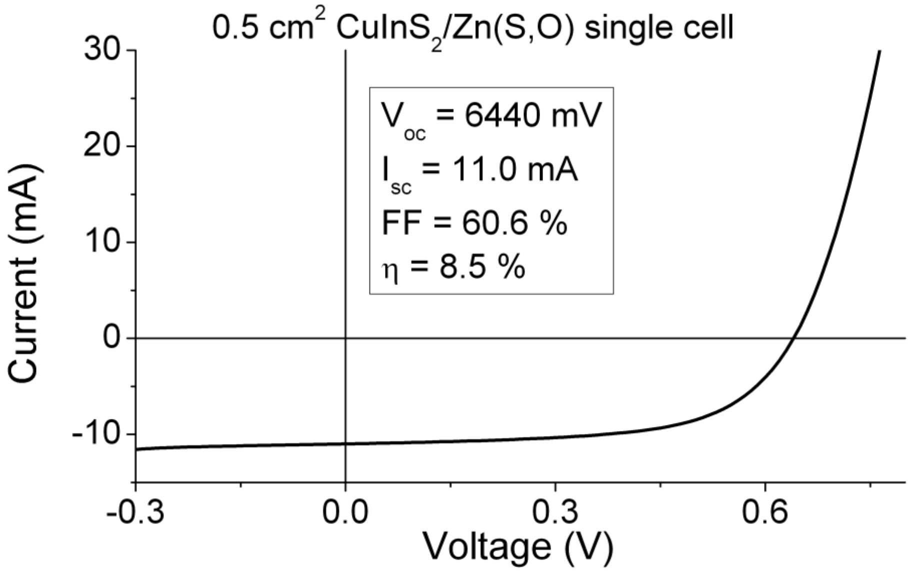

Figure 7.7: Current voltage curve of a Zn(S,O)-buffered CuInS$_2$ single cell (0.5 cm^2) showing the highest conversion efficiency obtained within this work. The corresponding PV parameters are included.

7.3 Band alignment in Zn(S,O) buffered CuInS$_2$ devices

The flat bands-band diagram estimated in chapter 5 (see figure 6.3) can be modified to obtain a more realistic one by adding the information obtained from the electrical characterization of Zn(S,O) buffered CuInS$_2$ devices. In these devices the energy conversion efficiency is limited by interface recombination due to an incomplete absorber inversion.

In cases where the activation energy of the saturation current density shows a value below the band gap of the absorber, two different situation might be occurring [169]:

- A negative conduction band offset, which shows up as $E_A = E_{g,i}$ where $E_{g,i}$ is the value of the band gap at the interface and is lower than the band gap of the absorber.
- The Fermi level is pinned. This can be diagnosed by $E_A = \phi_b^{p,0}$ where $\phi_b^{p,0}$ is the position of the Fermi level at the interface.

---

[4] References marked with * have Rodrigo Sáez-Araoz as an author and show results related to this work.

In the case of CdS-buffered $CuInS_2$ devices, the lower activation energy of the saturation current density is commonly related to the presence of a cliff ($\Delta E_c < 0$) at the conduction band offset [98]. In the case of Zn(S,O)-buffered references it has been demonstrated in section 6.3 that the presence of a spike ($\Delta E_c > 0$) is most probable. Therefore, the origin of the activation energy lower than the value of the absorber's band gap must be related to the pinning of the Fermi level at an unfavourable position, which in turn leads to an incomplete inversion of the absorber at the interface.

This situation has been modelled using the simulation program SCAPS-1D (Solar cell capacitance simulator in one dimension), which realistically simulates the electrical characteristics of thin film heterojunction solar cells.

The program SCAPS-1D finds dc solutions for structures consisting of an arbitrary number of semiconductor layers, with arbitrary doping profiles, with arbitrary energetic distributions of deep donor and/or acceptor levels in the semiconductor and at the heterogeneous interface [170, 171]. The basic equations used by SCAPS 1-D are the Poisson equation in one dimension, which relates the charge density $\rho(x)$ with the potential V:

$$-\frac{\partial^2 V}{\partial x^2} = \frac{\partial \mathbf{E_x}}{\partial x} = \frac{\rho(x)}{\epsilon_0 \epsilon_s} \tag{7.4}$$

and the continuity equations for electrons and holes:

$$\nabla \cdot \mathbf{J_n} = q(R - G) + q\frac{\partial n}{\partial t} \tag{7.5}$$

$$-\nabla \cdot \mathbf{J_p} = q(R - G) + q\frac{\partial p}{\partial t} \tag{7.6}$$

where J_n and J_p are the electron and hole current densities, R is the recombination rate and G is the generation rate. In the case of steady-state solutions (the one investigated in this work) $\nabla \cdot \mathbf{J} = 0$. For a detailed description of numerical simulation for photovoltaic devices, the reader is referred to [5].

Several different parameters for the different semiconductor layers of the device are used. These are listed in table 7.5 for the different layer materials and represent only an approximation. In the case of the buffer layer band gap, the value of the annealed material (3.6 eV, see figure 6.2) has been chosen, since the samples processed for photovoltaic applications are annealed. A conduction band offset of 0.5 eV is set for the simulations. This can be modelled by appropriately choosing the affinities of the heterojunction layers. Differences in the affinities correspond to either cliffs ($\chi_{CIS} < \chi_{Zn(S,O)}$) or spikes ($\chi_{CIS} > \chi_{Zn(S,O)}$) with a magnitude of $|\Delta E_C| = \left|\chi_{Zn(S,O)} - \chi_{CIS}\right|$.

The actual electronic characteristics of the different layers probably vary from production batch to production batch, even using the same process, thus causing different resulting efficiencies of the ready made solar cells. Many of the parameters cited refer to $CuInSe_2$ or $Cu(In,Ga)Se_2$ as no values for $CuInS_2$ are available. The parameters which are given in brackets, are only derived intuitively from the ones found in the literature and

Table 7.5: Parameters used for the simulation of the multilayered semiconductor devices.

	Absorber		Buffer layer	Front contact	
Parameter	CIS	CIS$_{surf}$	Zn(S,O)	i-ZnO	Al:ZnO
D[μ m]	1.99	(0.01)	0.015	0.1	0.5
E_g[eV]	1.5	(1.64)	3.6	3.3	3.3
χ[eV]	4[29]	(4)	3.6	(3.9)	(3.9)
ϵ_s	10[172]	(10)	(10)	(10)	(10)
N_{CB}[cm^{-3}]	2.2x10^{18}[29]	(2.2x10^{18})	(2.2x10^{18})	(2.2^{18})	(2.2^{18})
N_{VB}[cm^{-3}]	1.9^{19}[29]	(1.9^{19})	(1.9^{19})	(1.9x10^{19})	(1.9x10^{19})
$v_{th(n,p)}$[cm/s]	10^{7}	10^{7}	10^{7}	10^{7}	10^{7}
μ_n[cm^2/(V.s)]	100[98]	(100)	(100)	100[173]	(100)
μ_p[cm^2/(V.s)]	25[174]	(25)	(25)	(25)	(25)
N_D[cm^{-3}]	0	0	5x10^{16}[29]	10^{18}[98]	10^{20}[98]
N_A[cm^{-3}]	2x10^{16}[98]	(2x10^{16})	0	0	0
B	4.9x10^{5}[175]	(4.9x10^{5})	(2x10^{5})	(2x10^{5})	(2x10^{5})

those without any reference have been deduced in this work. The value of the band gap of the buffer layer has been taken from the optical measurements after annealing shown in figure 6.2. In the case of constant B (last row in table 7.5), it is in general found in the literature or by fitting experimental absorption data to the following expression:

$$\alpha(\nu) = \frac{B}{h\nu}\sqrt{h\nu - E_g} \tag{7.7}$$

Finally, the characteristics of the defects in the layer bulk have been chosen in a way that minority carrier lifetime τ comes to $1 \cdot 10^{-9}$ s in all layers of the solar cell, except the surface of the absorber, for which deviations from the stoichiometry could be translated in a larger defect density, and the buffer layer, whose nanocrystalline structure (see chapter 4) may also generate a larger defect density. The resulting minority carrier lifetime in these layer is set $1 \cdot 10^{-10}$ s.

Even a moderately charged interface can cause a significant variation of the field zones extending to both sides of the junction. Positive interface charge is desired because it increases the band bending in the absorber and thus the inversion. Fermi level pinning (FLP) is characterized by a charge neutrality level. Above this level, defects are acceptors and below it, donors. Depending on this neutrality level, inversion can be enhanced or reduced, leading to an improvement or deterioration of the open circuit voltage respectively [30]. In this case, the Fermi level has been pinned by placing uniformly distributed charged defects (concentration $> 10^{13}$ cm^{-3}) with an acceptor like character below the conduction band and donor like character above the valence band [176]. According to the value of the activation energy of the saturation current density obtained for Mo/CIS/Zn(S,O)/ZnO devices by means of J(V,T) analysis, $E_A \sim 1eV$, the Fermi level is pinned at 1 eV above the valence band at the interface. The final interface recombination velocity remains to 10^6 cm/s as in the case with neutral defects. The simulated band diagrams results can be seen in figure 7.8.

By pinning the Fermi level 1 eV above the valence band, the inversion of the absorber is hindered, lowering the open circuit voltage of the device according to the model proposed by R. Scheer [169]. In the unpinned case (black lines), the surface of the absorber layer is totally inverted providing a nearly full barrier for the holes (black arrow).

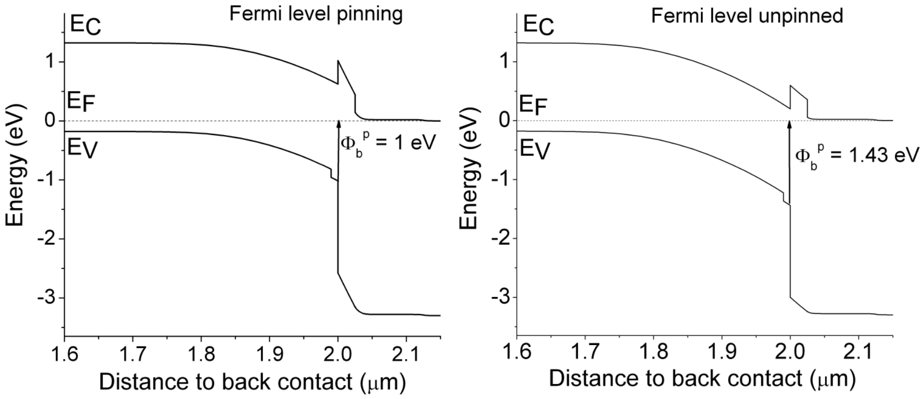

Figure 7.8: Modification of the band diagram at the $CuInS_2$//Zn(S,O) interface for two different set of interface states, one of them leading to Fermi level pinning. The interface recombination velocity is $S = 10^6$ cm/s in both cases.

7.4 Summary

In this chapter, the dominant recombination mechanisms of Zn(S,O) buffered chalcopyrite-based solar cells have been studied. Differences are found depending on the nature of the absorber:

- For $Cu(In,Ga)(S,Se)_2$, a low band gap absorber ($E_g \sim 1$ eV), an activation energy of the saturation current density showing the value of the band gap is found. Additionally, for dark and illuminated conditions, the diode ideality factor shows a negligible dependency on the temperature. These facts point to a dominant recombination mechanism which is thermally activated and which takes place at the space charge region. These are necessary conditions to be fulfilled in order to obtain high-efficiency devices.

- For $CuInS_2$, a wide band gap absorber ($E_g \sim 1.5$ eV), an activation energy of the saturation current density showing a value lower than that of the absorber's band gap is found. This is due to the presence of a recombination path with a reduced energy barrier. This analysis could only be performed on the data obtained under illumination, where the recombination process is thermally activated. In the dark, the diode ideality factor is strongly temperature dependent and an evaluation of the activation energy is not possible. This reduced barrier has also been reported in the case of CdS buffered $\mathrm{CuInS_2}$ devices, where it is commonly explained by presence of a cliff-like conduction band offset. Until now, the option of a pinned Fermi level in $\mathrm{CuInS_2}$/CdS devices as an explanation for the reduced barrier at the interface has not been taken into account. In the case of Zn(S,O) buffer layers, the formation of a spike is most probable and the reduced barrier can be explained by the pinning of the Fermi level at an energetic position equal to the energy barrier experimentally found. Simulations with the software package Scaps 1-D have shown how the pinning of the Fermi level 1 eV above the valence band at the interface reduces the energetic barrier for holes Φ_b^p, which represents the activation energy E_A of the saturation current density J_0.

Chapter 8

Towards industrial feasibility

In the previous chapters, different aspects of CBD-grown Zn(S,O) layers such as the growth mechanisms, the structure and microstructure as well as the performance of Zn(S,O) buffered thin film devices have been studied. The final aim is to obtain a feasible replacement for the CdS buffer layer used in state of the art chalcopyrite-based solar cells. From the previous sections (see chapter 7) it has been concluded that the transport mechanisms that govern the performance of Zn(S,O) buffered devices do not differ from those obtained investigating CdS-buffered reference cells. Resulting efficiencies are also comparable to reference devices, in the case of $CuInS_2$ and $Cu(In,Ga)(S,Se)_2$. This situates chemically deposited Zn(S,O) as a potential alternative to replace CdS, not only in laboratory scale solar cells (with sizes usually ranging from 0.1 to 1 cm^2, 0.5 cm^2 in this work), but also in production- or pilot line-scale solar modules. However, the challenges faced when working on either scale are different. Once the replacement has been proved successful in small scale devices, other factors come into play, which involves among other aspects, the economical feasibility of the process.

In the case of thin film solar cells, fundamental research and development is done mainly on small area single cell devices and have been widely treated in the previous chapters. Compositional and structural analysis are also preformed on small area samples. Therefore, one of the most important aspects to bear in mind is the homogeneity of the process, which will ensure that the conclusions extracted from the analysis of small area samples are relevant for large areas.

One of the most important aspects is that large scale exploitation of chalcopyrite-based thin film devices is partly dependent on a reduction of the potential environmental impact of the technology, as cadmium-containing compounds and wastes are highly regulated in the EU and elsewhere [177]. A reduction of the environmental impact is already achieved by the replacement of the CdS buffer layer by the alternative Zn(S,O) without significant efficiency losses.

Regarding the deposition process of buffer layers for industrial applications, metal chalcogenide thin film preparation by chemical bath deposition is a very attractive technique since it is relatively inexpensive, simple and convenient for large area deposition. Additionally a large variety of substrates can be used since it is a low temperature process that avoids oxidation or corrosion of metallic substrates. It also allows for the homogeneous and closed deposition of buffer layers on rough absorbers (see chapter 4), which may present inhomogeneities due to shadowing problems in other techniques.

8.1 Challenges

In order to have a process that could substitute the chemical bath deposition of CdS buffer layers in an industrial pilot line in the first stage, and then in a production scale fabrication process, many aspects have to be taken into account. First of all, the resulting devices have to deliver performances comparable (if not higher) to the standard CdS buffered devices. The deposition time should be also comparable in order to maintain the production yield and not to introduce a bottleneck in the production chain. Also the critical issues of efficient use of the chemicals and recycling must be faced. This is very important in the case of Zn(S,O) buffer layers, since due to the solubility constants, more concentration of chemicals is needed (see chapter 3), thus increasing the manufacturing costs. The basic fact of using a zinc compound as a substitute for CdS, has already important benefits not only from the environmental point of view, but also from the economic one, since it reduces the costs of the waste treatment and lowers the security level of the installations.

8.2 Up-scaling from laboratory scale to large area devices: homogeneity

The upscaling of the CBD process for the deposition of Zn(S,O) buffer layers has to transfer the quality and properties of the buffer layer grown on small area to large area substrates. In principle CBD techniques allows for an easy upscaling when compared to other deposition techniques such PVD or ILGAR, where the investment needed for the upscaling is much higher. In the case of CBD what is needed is a homogeneous distribution of the temperature throughout the solution. The homogeneity of the deposited buffer has been tested by buffering 10x10 cm^2 CIS absorbers, characterizing 96 individual solar cells and mapping the resulting PV parameters as a function of the cell's position on the absorber. These mappings for V_{oc} (in mV), J_{sc} (in mA/cm^2), FF and η (both in %) can be seen in figure 8.1. The respective averages and standard deviations are presented in table 8.1. The results show very small standard deviations, which account for a very homogeneous stack of layers (this includes the absorber -CIS-, the buffer layer -ZnS/Zn(S,O)- and the window layer -i-ZnO/Al:ZnO-). Losses can only be spotted at the borders of the absorber, probably due to some damage in the absorber during the cleaving stage or due to shadowing effects of the sample holder during the deposition of the buffer layer. This losses are not significant because in module production, the areas close to the

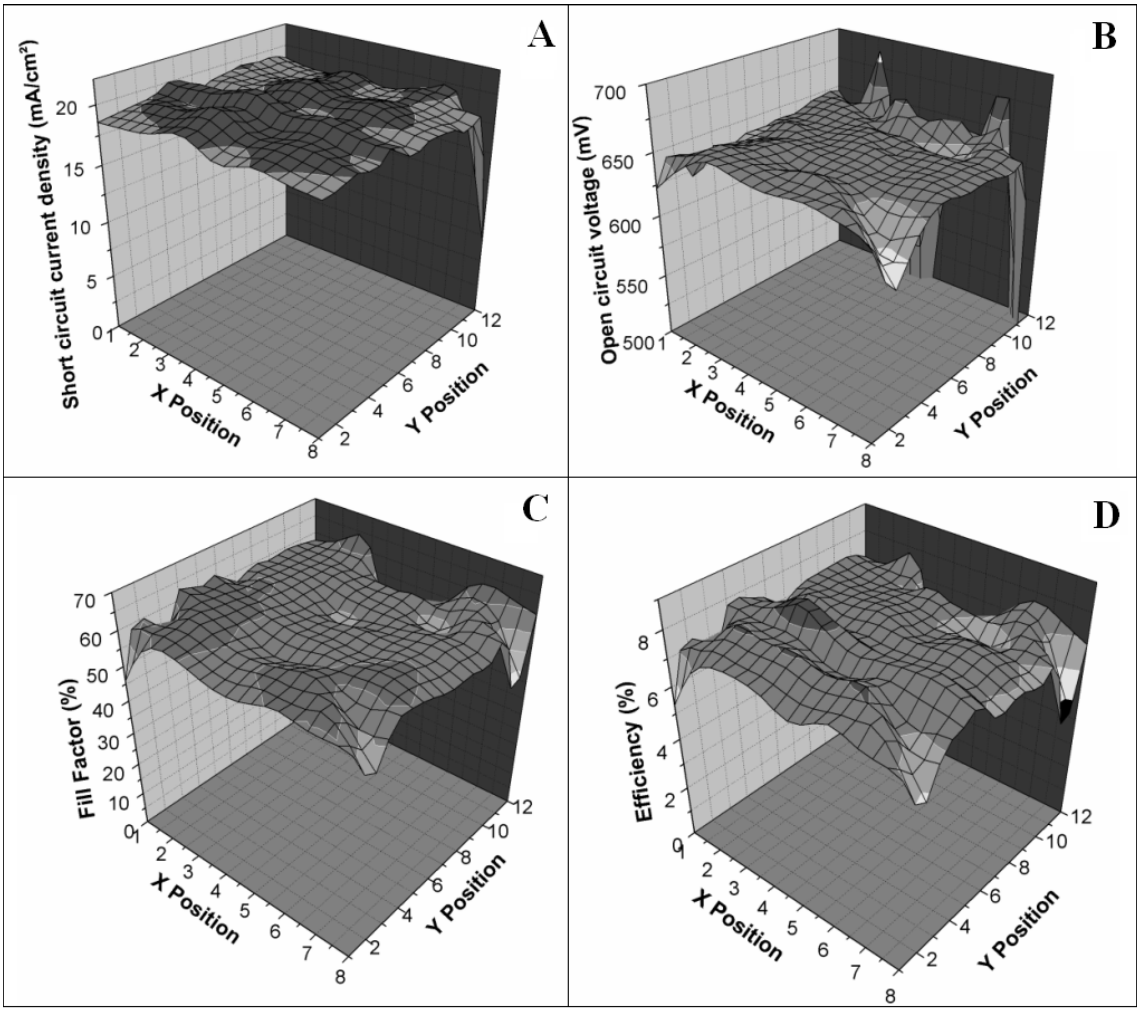

Figure 8.1: Spatial mapping of the PV parameters (A: short circuit current density, B: open circuit voltage, C: Fill factor and D: efficiency) obtained by characterizing ninety-six 0.5 cm^2 solar cells scribed from a single 10x10 cm^2 absorber.

border of the absorber are not active area.

A proof for the successful upscaling from 10x10 cm^2 to 30x30 cm^2 is the performance of CIGSSe modules buffered with Zn(S,O). 30x30 cm^2 CIGSSe absorbers from the pilot line of AVANCIS GmbH & Co. KG have been buffered in an up-scaled chemical reactor which can be simple described as a larger version of that used to deposit the buffer layer on smaller absorber sizes. These absorbers have been buffered using both the standard CBD and the CBD including the additive. After the deposition of the buffer layer, infrared thermography images are taken in order to check the homogeneity of the device. In this technique, an infrared camera is used to check the slight temperature differences. For the measurements, the module is placed in front of the camera and an external voltage is applied. The differences of temperature are shown in a colour scale on a monitor. Bright regions correspond to hot spots and indicate areas where a large current is flowing and

Table 8.1: Average PV parameters and standard deviation of 96 single cells (0.5 cm^2) scribed from a $10x10cm^2$ Zn(S,O) buffered CIS absorber together with the PV parameters of the cell showing the highest efficiency. V_{oc} is given mV/cell, J_{sc} in mA/cm^2, and the fill factor (FF) and the efficiency (η) in %.

Sample	V_{oc}	J_{sc}	FF	η
060606-38-10/11-14715	636 ± 4	21.5 ± 0.4	58.8 ± 1.6	8.1 ± 0.2
Best cell	640	21.9	60.6	8.5

power is being dissipated in form of heat. If there is an active shunt that shortcircuits a given cell lowering the open circuit voltage of the device (and consequently the efficiency), its location can be spotted and it can be mechanically passivated by removing the ZnO top layer by means of a needle. This simple procedure has shown good results in terms of performance's improving. Figure 8.2 shows two IR-thermography images of a CIS 5x5 cm^2 minimodule. The image on the left shows a shunt (bright spot) which was removed before recording the image on the right. The cell where the shunt in located appears as a dark region, since all current is flowing through the shunt and the temperature in the rest of the cell is lower. By removing the shunt an efficiency improvement of 1.7% (absolute) was achieved, stating at 6.7% prior to shunt removal and reaching 8.4% afterwards.

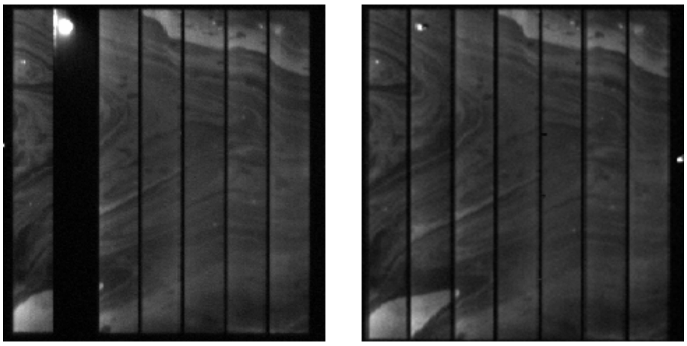

Figure 8.2: Infrared thermography image of a CIS/Zn(S,O) 5x5 cm^2 minimodule before (left) and after removing the shunt (right). The active shunt appears as a bright spot in a dark cell.

A thermography image of a 30x30 cm^2 CIGSSe/Zn(S,O) module is shown in figure 8.3. No active shunts are detected, accounting again for a homogeneous deposition of all layers forming the device. The efficiency of the final device is 11.8%.

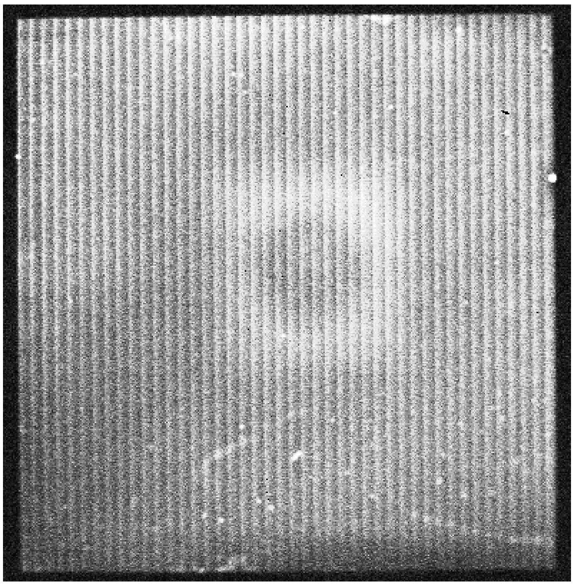

Figure 8.3: Infrared thermography image of a CIGSSe/Zn(S,O) 30x30 cm^2 module. Final efficiency is 11.8%.

8.3 Reduction of processing time

Standard Zn(S,O) buffer layer have been deposited in times ranging from 15 to 25 minutes. The inclusion of the turbidity monitoring system has greatly helped to understand the mechanisms of the deposition process and thus to reduce the deposition time. This was studied in section 3.3 where the impact of the different CBD condition on the chemical reaction and particle formation was presented. According to the results, different strategies can be followed in order to reduce the deposition time.

Concentration of precursors

By increasing the concentrations of precursors in the chemical bath, the deposition time was reduced (see figure 3.10 in page 42). Unfortunately, such a strategy is not economically feasible, since it increases the overall costs of the buffer production. In order to obtain deposition times below 10 minutes (as it is the case in CdS deposition), twice as much precursors as in the standard case must be used. Also the efficient use of chemicals is questionable. Therefore no further investigations have been done in this direction.

Concentration of ammonia

The decrease of the ammonia concentration in the bath accelerates the formation of particles, thus reducing the deposition time. Such a strategy would be optimal since the reduction of the deposition time is due to a reduction of one of the chemicals used in the deposition process, in opposite to the previous example. This would result in a decrease of the total costs. In order to study the impact of varying the concentration of ammonia in the device performance, 5x5 cm^2 Cu(In,Ga)$(S,Se)_2$ absorbers were buffered with Zn(S,O) layers prior to device completion by sputtering the i-ZnO/Al:ZnO window layer and evaporation NiAl grids for better current collection. 0.5 cm^2 single cells were characterized at the sun simulator under standard test conditions. The average PV parameters are shown in table 8.2.

Table 8.2: Average PV parameters and standard deviations of twelve 0.5 cm^2 single cells (Mo/Cu(In,Ga)$(S,Se)_2$/Zn(S,O)/i-ZnO/Al:ZnO) processed using different concentrations of ammonia. The concentration of ammonia is given normalized to the standard concentration. The deposition time (in seconds) is considered to be the time at which the transparency of the solution reaches 20% of the initial value. V_{oc} is given in mV, J_{sc} in mA/cm^2, and the fill factor (FF) and the efficiency (η) in %.

rel $[NH_3]$	Time (s)	V_{oc}	J_{sc}	FF	η
1	1350	536 ± 5	38.4 ± 0.3	65.1 ± 2.5	13.5 ± 0.5
0.5	930	437 ± 18	38.3 ± 0.7	57.1 ± 1.5	9.6 ± 0.8
0.42	430	416 ± 18	38.9 ± 2.7	59.8 ± 4.3	9.6 ± 0.9

Although using 42% on the standard ammonia concentration leads to the reduction of the deposition time below 10 minutes, the PV performance of buffered devices sinks. Some explanations to this behaviour can be found by looking at the turbidity graphs presented in figure 3.13 (page 46). It is clear that by reducing the concentration of ammonia, the homogeneous nucleation starts to take place earlier and the first plateau dissapears from the graph. It was shown that the first stage of the process, where the solution stays clear but there is deposition of a Zn-containing layer, corresponds to a slow ion-by-ion growth of a ZnS layer. The gitter constants of CIS and ZnS are very similar, enabling a quasi-epitaxial growth of the buffer on the absorber. In the case of a reduced ammonia concentration, the particles formed in the bulk of the solution and detected by the optical monitoring set up are deposited right away, which in turn has a negative influence on the absorber-buffer interface, as it can be seen in the particularly low values of the open circuit voltage. On the other hand, the particle formation speed is higher (as deduced from the values of dt). This fact leads to a non-homogeneous (in the geometrical, not the chemical acception) deposition process, where the thickness of the buffer layer is not uniform throughout the substrate, which in turn leads to the higher values of the standard deviation found for the cells buffered with lower concentrations of ammonia.

Control temperature

Another strategy that leads to a reduction of the deposition time is the increase of the bath temperature (see figure 3.9 in page 40). Experiments in order to verify if the performance of the devices is maintained with a reduced deposition time by increasing the temperature were done using 10x10 cm^2 CIGSSe absorbers. The absorbers were buffered and sent to AVANCIS GmbH & Co. KG for device completion (including mechanical scribing -P2 and P3- and window layer deposition) and analysis. Table 8.3 shows the performance of the best four 10x10 cm^2 modules process using the standard CBD and the hight temperature CBD. As it can be seen, the device performance is identical in both cases, which means that the deposition time can be successfully reduced by increasing the bath temperature.

Table 8.3: Average PV parameters and standard deviation of the best four 10x10 cm^2 CIGSSe/Zn(S,O) modules processed using the standard and the high temperature CBD. Deposition time is given in seconds, V$_{oc}$ in mV/cell, J$_{sc}$ in mA/cm^2, and the fill factor (FF) and the efficiency (η) in %.

CBD	Time (s)	V$_{oc}$	J$_{sc}$	FF	η
Standard	1100	536 ± 8	34.1 ± 0.2	66.9 ± 0.7	12.2 ± 0.1
High Temperature	400	539 ± 7	34.0 ± 0.4	67.1 ± 1.0	12.3 ± 0.1

Increasing the temperature to reduce the deposition time while maintaining the previous efficiencies has been successfully tried in devices up to 10x10 cm^2. Unfortunately no data on 30x30 cm^2 modules is available, since due to technical difficulties it is not possible to heat up the whole bath used for this substrate size to the desired temperature. Minimizing the heat losses in the water circuit is necessary.

Inclusion of additive

It has already been shown throughout this work how the use of an additive affects the growth and properties of the buffer layer and the final device. From the results obtained, it can be foreseen, that the inclusion of the additive in the chemical bath may lead to a reduction of the deposition rate without losses in the performance.

Nineteen 30x30 cm^2 CIGSSe with a Zn(S,O) buffer layer deposited with additive have been characterized using the continuous light sun simulator located at AVANCIS GmbH & Co. KG. The results are shown in figure 8.4. Efficiencies as high as 12.5% have been obtained with an average efficiency exceeding 11%. The best efficiency obtained on a 30x30 cm^2 CIGSSe absorber buffered with the standard Zn(S,O) CBD is also 12.5% and the average is also found at approximately 11.5%. Therefore, the new process developed to reduce the deposition time has proven successful and has fulfilled the necessary steps before being transferred to an industrial pilot line.

The different strategies suggested are summarized in table 8.4 as a function of the actual reduction of deposition time, the effects on the costs and the increase in the performance.

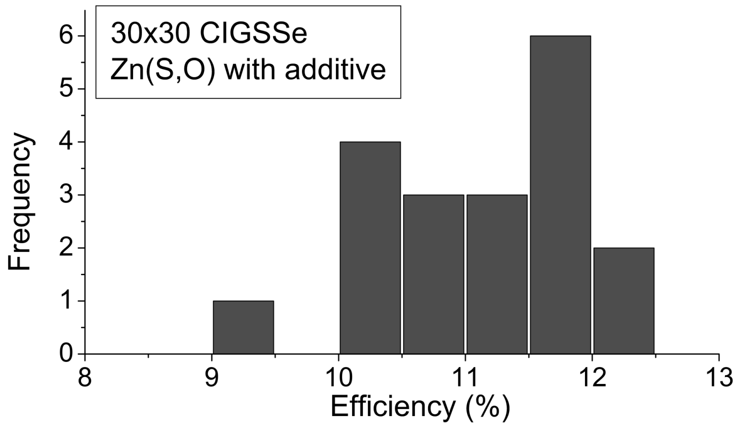

Figure 8.4: Efficiency results of nineteen 30x30 cm^2 CIGSSe absorbers with a Zn(S,O) buffer deposited using a CBD including the additive.

Table 8.4: Summary of the different modifications of the standard CBD process and their influence on the deposition time, the potential reduction of production costs and the device efficiency.

Modification	Deposition time	Costs	Device efficiency
Higher [Zn^{2+}], [TU]	$\leq$ 10 min	Higher	Not tried
Lower [NH$_3$]	$\leq$ 10 min	Lower	Lower
Higher temperature	$\leq$ 10 min	$\sim$	Comparable
Additive	$\leq$ 10 min	$\sim$	Comparable

Using either a higher temperature or the additive slightly increases the process costs, but the benefits are much higher, since the duration of the buffer deposition process is halved without decreasing the final efficiency of the device, thus increasing the potential yield of the whole process.

8.4 Efficient use of the chemicals. Recycling

A major drawback of the CBD process is the inefficiency of the process, in terms of the utilization of starting materials and their conversion to thin films. The extent of the heterogeneous reaction on the substrate surface is limited by two major factors, the competing homogeneous reaction in solution (which results in massive precipitation in solution) and deposition of material on the CBD reactor walls. It has been widely argued that most of the chemicals used are not deposited on the substrate, but remain in the solution, lowering the material efficiency of the process. In order to improve the utilization of the chemicals, two tactics can be simultaneously followed. On one hand the volume of the solution should be decreased and on the other hand the recycling of the remaining solution should be optimized. These two tactics lead to an immediate impact on the material utilization which in turn leads to a direct reduction of the production costs. During the upscaling of the process from 0.5 cm^2 single cell devices to 10x10 cm^2 and 30x30 cm^2 modules the volume of the solution per cm^2 has been constantly reduced from approximately 20 ml/cm^2 in the case of single cells to less than 1 ml/cm^2 for 30x30 cm^2 modules just by designing optimized beakers. In terms of material consumption this is translated in a reduction from 0.9 g/cm^2 of Zn(SO)$_4$ and TU in the case of 0.5 cm^2 single cells to less than 0,05 g/cm^2 for 30x30 cm^2 absorbers using the optimized beakers. A significant reduction of the concentrations of the chemicals is in principle not possible if we want to obtain comparable results in terms of efficiency. Reducing the concentration of precursors leads to slower deposition rates and the decrease of the ammonia concentration alters the composition of the buffer layer with increased Zn-oxygen/ZnS ratio [94].

On the other hand, the reuse of the solution for further deposition processes can significantly help to reduce the materials costs. Preliminary experiments have been carried out within this work using CIGSSe absorbers (size 10x10 cm^2) as a proof of concept. Three different strategies have been followed, all of them beginning with the filtering of the CBD solution previously used to buffer 30x30 cm^2 CIGSSe absorbers.

1. The thermostat is set to the desired temperature. Once this temperature is reached, the sample is introduced into the reactor and the filtered solution is poured inside (at room temperature). Transparency and temperature are controlled during the process and the sample is removed out of the chemical bath when the transparency reaches a value of 20% (14.5 minutes). The solution stayed clear at the early stages and a loss in the transparency was visible after 8-9 minutes, when the temperature of the bath reached 70 °C. Afterwards, the sample is annealed in air for 10 minutes at 200 °C.

2. The thermostat is set to the desired temperature. Once this temperature is reached, the filtered solution (at room temperature) is added to the reactor. Once the temperature of the solution reaches 50 °C (3.5 minutes), the samples are introduced, 3 minutes later, (T=65 °C), 0.4% of additive is added. A pronounced step-like drop is immediately observed in the transparency curve. Samples are removed after a deposition time of 7.5 minutes (3 minutes in absence of additive and 4.5 after the additive is added). Afterwards, the samples are annealed in air for 10 minutes at 200 °C.

3. The thermostat is set to the desired temperature. Once this temperature is reached, the filtered solution (at room temperature) is added to the reactor. When the temperature reaches 65 °C, 6% of ammonia and 0.4% of additive are added. The samples are then introduced in the bath and removed after 5 minutes. Afterwards, the samples are annealed in air for 10 minutes at 200 °C.

The obtained results can be found in table 8.5. The numbers correspond to the previous enumeration.

Table 8.5: PV parameters of 10x10 cm^2 CIGSSe/Zn(S,O) devices buffered with a previously used chemical solution. The number under CBD correspond to the previous enumeration. Deposition time is given in minutes, V_{oc} in mV/cell, J_{sc} in mA/cm^2, and the fill factor (FF) and the efficiency (η) in %.

CBD	Time	V_{oc}	J_{sc}	FF	η
1	14	485	30.9	60.5	9.1
2	10	496	32.8	62.5	10.1
2	10	506	32.7	60.8	10.1
3	5	518	34.3	64.8	11.5
3	5	518	34.1	64.5	11.4

8.5 Summary

After this short discussion, it is clear that the up-scaling of Zn(S,O) as a replacement for CdS in large area, production scale absorber, is feasible, and that the challenges that such step requires, such as homogeneity of the deposited buffer, the reduction of the deposition time and the optimization of the material utilization in the chemical bath can be successfully faced with the CBD process detailed in this work. Zn(S,O)-buffered $Cu(In,Ga)(S,Se)_2$ absorbers (900 cm^2) from the pilot line of AVANCIS GmbH & Co. KG. have shown efficiencies as high as 12.5%, comparable to those obatained by CdS-buffered references.

Chapter 9

Summary and outlook

Chalcopyrite absorbers with a chemically deposited CdS buffer layer constitute the state of the art thin film solar devices and, depending on the chalcopyrite material of choice, efficiencies as high as 20% can be obtained. The aim of this work is to successfully replace the toxic CdS buffer layer by a chemically deposited Zn(S,O) layer without losses in the performance and to upscale the technologies used in laboratory scale experiements to pilot and production line absorbers for industrial applications. The work included in this thesis has been done within the framework of the European integrated project ATHLET (Advanced Thin Film Technologies for Cost Effective Photovoltaics) using $CuInS_2$ and $Cu(In,Ga)(S,Se)_2$ absorber layers provided by the industrial partners (Sulfurcell Solartechnik GmbH and AVANCIS GmbH & Co. KG. respectively).

After a review of the roles of the different layers that form chalcopyrite-based thin-film solar cells and modules in chapter 2, in chapter 3, the basics of chemical bath deposition have been used as the starting point to describe a new and well controlled deposition process for Zn(S,O) buffer layers, that has been used as an alternative to state of the art CdS buffer layers. A novel monitoring tool has been developed, which measures in situ the turbidity of the chemical solution during the process. A series of experiments have been performed to evaluate the influence of the different process parameters (temperature, concentration of chemicals and reaction times) on the kinetics of the chemical reactions. A model has been presented to explain the formation of the turbidity in the solution and it has been successfully applied to the turbidity measurements performed during the various experiments. Two distinct stages have been identified:

- During the first stage no detectable particles are formed and the solution stays clear. Formation of ZnS by means of an ion-by-ion process is expected.
- After a certain time which depends on the conditions of the chemical bath (namely bath temperature and precursors' concentrations), formation of clusters starts in the solution which is translated in an increasing turbidity. The clusters's formation rate is also intimately correlated to the conditions of the chemical bath. The dominant growth mechanims in this stage is expected to be based on the homogeneous nucle-

ation. Formation of ZnS and ZnO (from the conversion of $Zn(OH)_2$ into ZnO and H_2O) is expected in this stage.

Based on these results, several strategies have been identified that accelerate the reactions in the chemical bath (increase of bath temperature and precursor's concentrations, decrease of ammonia concentration), and aimed improvements have been introduced in order to increase the deposition rate of the buffer layer (and thus reduce the deposition time). The positive results in terms of shorter deposition times (a reduction of more than 50% of the original time) obtained by modifying the deposition process with the inclusion of a highly oxidizing agent in the chemical bath has led to the presentation of a patent proposal that is currently being evaluated.

In chapter 4, the growth of the Zn(S,O) buffer layer on both chalcopyrite materials $CuInS_2$ and $Cu(In,Ga)(S,Se)_2$ has been studied by electron microscopy. The formation of a nanocrystalline buffer layer has been observed. Analysis of the lattice plane distances by means of transmission electron microscopy have shown the formation of ZnS crystallites with sizes up to 3 nm in diameter. The formation of ZnO crystallites could not be confirmed by these techniques. Additionally, and by means of energy dispersive x-ray analysis on $Cu(In,Ga)(S,Se)_2$/Zn(S,O) samples, a thin (3-4 nm) layer with a higher sulphur content has been detected which if formed during the first stage of the chemical bath deposition process. The sulphur content is then reduced in the rest of the layer, accounting for the material deposited during the second stage. The average growth rate has also been estimated for the cases of the standard CBD process and the modified one (with the inclusion of the additive). The faster nucleation rate confirmed by the analysis of the turbidity measurements has been successfully translated into a higher deposition rate on the chalcopyrite material, increasing from a growth rate of $\sim$ 0.25 nm/min to $\sim$ 2 nm/min in the case of $CuInS_2$ absorbers.

The microstructure of the chemically deposited Zn(S,O) has been studied by means of x-ray photoelectron spectroscopy and the results of these investigations are presented in chapter 5. CBD processes were interrupted at different deposition times in order to obtain a time-resolved (and thus thickness-resolved) view of the formation of the buffer layer on $CuInS_2$ absorbers. The higher deposition rate in the case of the modified CBD process has also been confirmed by the faster attenuation of the absorber related core levels. The composition of the buffer layer has been studied for both the standard and the modified CBD and differences have been observed, which confirm the predictions based on the analysis of the turbidity during the process:

- In the case of the standard CBD, the composition of the buffer layer is thickness dependent. A pure ZnS layer is deposited on the absorber material whereas for thicker buffer layers, the chemical compositions shifts to a Zn(S,O) compound, with a ZnS/(ZnS+ZnO) ratio of approximately 0.8 after 13.5 minutes. This supports the predictions obtained from the analysis of the turbidity and the results presented in chapter 4.

- In the case of the modified process, the first stage of the CBD, where the solution stays clear, is greatly reduced and a homogeneous buffer layer composition is found, with a ZnS/(ZnS+ZnO) ratio of approximately 0.5.

In both cases, the composition of the buffer layer does not significantly change after a post deposition heat treatment in air (5 minutes at 200 °C)

These results have been combined in chapter 6 with those obtained by means of ultraviolet photoelectron spectroscopy to determine the valence band offset before and after the post deposition heat treatment at the interface between $\mathrm{CuInS_2}$ and Zn(S,O) deposited by the modified CBD process. A value of 1.8 eV is found which agrees with those previously reported for the case of the standard CBD and laboratory scale $\mathrm{CuInS_2}$ delivered by the Technology Department at the Helmholtz Zentrum Berlin. After the heat treatment this value is reduced to 1.5 eV. This reduction can be explained by the heat-induced formation of $\mathrm{Zn_{Cu}^{+}}$ antisites. The corresponding offsets at the conduction band have been estimated based on the analysis of the valence band offsets and the values of the energy band gaps of both heterojunction partners. A value of 0.5 eV is obtained in both cases, i.e. before and after the heat treatment, indicating the presence of a spike-like conduction band offset ($\mathrm{E_{CB}^{Zn(S,O)}} > \mathrm{E_{CB}^{CIS}}$).

The results regarding the photovoltaic performance of laboratory scale single cells (with an area of 0.5 $\mathrm{cm^2}$) are shown in chapter 7. The best conversion efficiency obtained on production scale $\mathrm{CuInS_2}$ absorbers has been 8.5 %[1]. In the case of $\mathrm{Cu(In,Ga)(S,Se)_2}$ absorbers from the AVANCIS's pilot line, the highest conversion efficiency reached 15,1%. For both materials, the dominant recombination mechanisms governing the performance of the devices has been studied by means of temperature dependent current-voltage analysis:

- In the case of $\mathrm{CuInS_2}$/Zn(S,O) there is a difference in the dominant recombination mechanisms as a function of the illumination conditions. In the dark, tunneling processes dominate the recombination, while under illumination these become thermally activated. In both cases, the recombination takes place at the interface due to a reduced barrier.

- In the case of $\mathrm{Cu(In,Ga)(S,Se)_2}$/Zn(S,O) devices, a thermally activated recombination in the space charge region is found both in the dark and under illumination.

For both chalcopyrite materials, these characterization results are similar to those obtained for CdS-buffered references, thus supporting the feasibility of ZnS to replace the conventional CdS buffer layer for Cd-free thin film solar cell.

After having shown that Zn(S,O) is a feasible replacement for CdS buffer layers in laboratory scale devices, the final step was the up-scaling of the deposition process in

---

[1] On laboratory scale $\mathrm{CuInS_2}$ absorbers provided by the Helmholtz Zentrum Berlin the highest conversion efficiency obtained reached 11.4%.

order to buffer large area absorbers (with sizes up to 30x30 cm^2). The results are presented in chapter 8. The absence of pin holes on large area devices has been confirmed by means of infrared thermography whereas the homogeneity of the layer has been investigated by mapping the local PV parameters of single cells scribed on 10x10 cm^2 $CuInS_2$ substrates. Average efficiencies (96 single cells) of 8.1±0.2 % account for the high homogeneity of the deposition process on large area. Based on the results obtained from the analysis of the turbidity measurements several strategies were identified which led to a reduction of the deposition time. Both an increased temperature and the inclusion of the additive have resulted in high efficiency solar modules with a reduced buffer layer deposition time (below 10 minutes). The best conversion efficiencies obtained for both chalcopyrite materials in large area solar modules are 7.2% ($CuInS_2$, 10x10 cm^2), 6.6%($CuInS_2$, 30x30 cm^2), 12.5% ($Cu(In,Ga)(S,Se)_2$, 10x10 cm^2) and 12.5% ($Cu(In,Ga)(S,Se)_2$, 30x30 cm^2).

Finally, another important aspect is the efficient utilization of the chemicals in CBD. Regarding this issue two complementary strategies have been followed:

- The volume of solution has been reduced by using specially designed reactors and beakers. This has allowed a reduction of one order of magnitude, from $\sim$10 ml/cm^2 used for processing samples of approximately 5 cm^2, to $\sim$1 ml/cm^2 used when four modules (size 30x30 cm^2) are processed in the same bath.
- Re-using the chemical solution would greatly help to decrease the costs associated to buffer deposition. Three different processes have been tried and the results are promising: efficiencies as high as 11.5% on 10x10 cm^2 CIGSSe/Zn(S,O) devices have been obtained.

In this work it has been therefore demonstrated that Zn(S,O) can successfully replace CdS buffer layers not only in laboratory scale but also in large area devices without losses in the performance of the corresponding devices. The next step is then the investigation of the long term stability and the life time of such devices, which is a critical issue for industrial applications.

Appendix A

Energy ranges of investigated core levels and Auger signals

Surface analysis by x-ray photoelectron spectroscopy (XPS) and x-ray excited Auger electron spectroscopy (XAES) is accomplished by irradiating the sample under analysis with MgKα x-rays, with an energy of 1253.6 eV. Table A.1 summarized the binding energies scanned to analyze each of the core levels and Auger signals investigated.

Table A.1: Binding energies (in eV) of core levels and Auger signals investigated in this work. MgKα x-rays, with an energy of 1253.6 eV are used.

Core level	Binding energy range (eV)	Comments
Au4f$_{7/2}$	79-91	Calibration
Survey	0-1150	
01s	525-537	Partly contamination
C1s	281-295	Contamination
Cu2p$_{3/2}$	928-945	
In3d	439-453	
S2p	156-173 eV	
Zn2p$_{3/2}$	1015-1029	
Valence band	0-23 eV	In4d and Zn3d
Auger signals		
InLMM	835-870	
ZnLMM	256-276	
OKLL	729-755	

Appendix B

Recombination mechanisms in thin film solar cells

The impact of the recombination mechanisms on the performance of the device is of major importance in device diagnosis, since they determine to a large extent the characteristic diode parameters (A and J_0) and therefore the values of the photovoltaic performance. The role of the heterojunction interface as a drain for charge carriers is of critical importance, as a result of the high density of electronically active defects that appear due to the lattice mismatch between the dissimilar absorber and buffer materials brought into contact. Recombination taking place at the interface has a direct effect on obtainable open-circuit voltages and must be minimized in order to achieve high efficiencies [30]. In the following, the main recombination mechanisms expected to operate in the devices under study will be reviewed, with particular attention to those aspects that may help discerning between them.

Generally speaking, the total recombination current can be expressed as:

$$J = q \int R dx \tag{B.1}$$

where R denotes the recombination rate of electron-hole pairs and the integral extends over the region where recombination events occur (e.g. the space charge region or the entire absorber layer). A generalized expression for the recombination rate R was given by Rau [162] based on the classical Shockley-Read-Hall (SHR) model [178, 179] of bulk recombination via a discrete defect level in the band gap, and the work of Hurkx *at al.* [180], which includes tunneling-assisted recombination. The expression reads:

$$R = \frac{np - n_i^2}{\gamma_p(n + n^*) + \gamma_n(p + p^*)} \tag{B.2}$$

where n_i^2 is the intrinsic carrier concentration for a given temperature, $n^* = N_C exp[(E_T - E_C)/kT]$ and $p^* = N_V exp[(E_V - E_T)/kT]$ are the electron and hole concentrations obtained if the Fermi level lied at the defect level E_T, and $\gamma_{n,p}$ include corrections due to tunneling processes. Equation (B.2) can be used to describe interface- as well as bulk-recombination via trap states. In the case of interface recombination, R is given in cm^{-2}s^{-1}, and $\gamma_{n,p}$ are defined according to:

$$\gamma_{n,p} = \frac{1}{S_{n,p}(1-\Gamma)} \tag{B.3}$$

where $S_{n,p}$ denote the interface recombination of electron and holes, as explained later, and Γ is the correction factor describing the recombination enhancement due to tunneling-assisted processes. In the case of bulk recombination, R is expressed in units of cm^{-3}s^{-1} and $\gamma_{n,p}$ are defined according to:

$$\gamma_{n,p} = \frac{\tau_{n,p}}{(1-\Gamma)} \tag{B.4}$$

where $\tau_{n,p}$ are the lifetimes of electrons and holes.

Starting from equation (B.2) and based on the works by Hengel [31] and Reiss [32], it will be shown that the theoretical models developed for the different recombination mechanisms predict particular relationships between the diode parameters (A and J_0), including temperature dependencies, that will be used to identify experimentally those processes controlling the performance of the device.

Recombination in the SCR: thermally activated

It can be seen in equation (B.2) that the recombination rate is driven by the difference between the term $n \cdot p$ and n_i^2, which accounts for the excess carrier concentration induced e.g. by illuminating the device. According to the general theory of semiconductors (e.g. [181]), the following expression holds within the entire semiconductor between majority and minority carrier concentrations, for given biasing conditions:

$$np = n_i^2 exp\left(\frac{qV}{kT}\right) \tag{B.5}$$

If this expression is substituted in equation (B.2), and assuming that $\gamma_n = \gamma_p$[1], it follows that the recombination rate is maximum when $n + p$ is minimum, which is the case when $n = p$. Excluding at this point the participation of tunneling processes ($\Gamma = 0$), equation (B.2) leads to:

$$R_{max} = \frac{n_i}{2\tau}\left(exp\left(\frac{qV}{2kT}\right) - 1\right) \tag{B.6}$$

the recombination being effective in the region $dx \sim 2kT/qE_{max}$ (E_{max} denotes the maximum electric field) around the position where $n = p$. If dx does not strongly depend

---

[1] This assumption implies equal capture cross section for electron and holes. This is a reasonable statement following the SRH theory for defects lying at mid-gap.

on the applied bias, the recombination current (Eq. (B.1)) can be approximated by:

$$J = qR_{max}dx \approx \frac{qn_i}{2\tau}dx\left(exp\left(\frac{qV}{2kT}\right)-1\right) = J_0\left(exp\left(\frac{qV}{2kT}\right)-1\right) \tag{B.7}$$

This expression obtained for the case in which the electronic transport is controlled by carrier recombination in the space charge region, without tunneling enhancement and via a single defect level in the band gap of the absorber resembles that derived for the diode, predicting an ideality factor $A = 2$. In this case the saturation current can be written as:

$$J_0 = J_{00}exp\left(\frac{-E_g}{2kT}\right) \tag{B.8}$$

which states that the thermally activated activation energy of the saturation current of such a deviced is $E_A = E_g/2$.

This model accounts for the recombination within the space charge region based on the SRH theory of a single defect level in the band gap, but may be extended to the case where a continuous exponential defect density distribution from the band edge decaying into the gap is present [182].

In the case of a device controlled by recombination over a distribution of defect states, the ideality factor is slightly temperature dependent, ranging from 1 to 2 with decreasing temperatures following:

$$A^{-1} = \frac{1+\frac{T}{T^*}}{2} \tag{B.9}$$

where kT^* is the characteristic energy of the exponential decay [32].

Recombination in the SCR: tunneling enhancement

The model of tunneling enhanced recombination over a continuous exponential defect distribution within the SCR predicts a temperature dependence of the ideality factor given by [162]:

$$A^{-1} = \frac{1}{2}\left(1-\frac{E_{00}^2}{3(kT)^2}+\frac{T}{T^*}\right) \tag{B.10}$$

for $kT > E_{00}$, where E_{00} is the characteristic energy of the transition from tunneling to thermally activated processes and kT^* is the characteristic energy of the defect distribution. The saturation current J_0 is in this case:

$$J_0 = J_{00}\cdot exp\left(-\frac{E_g}{AkT}\right) \tag{B.11}$$

Recombination at the interface: thermally activated

The recombination of charge carriers taking place at an interface (or surface) can be interpreted in terms of a surface recombination velocity $S_{n,p}$ as shown in equation (B.3). S is defined as the number of carriers recombining at a surface per unit area per unit time per unit volume of excess charge carriers at the boundary between the quasi-neutral region and the depletion region associated to the surface [183]. This velocity is proportional to the surface density of states and it is limited by the velocity with which carriers arrive at the surface (the drift velocity associated to the surface potential). Each recombination center is characterized by the capture cross-section of holes and electrons, and which in turn determine the effectiveness of the given trap as a recombination center or simply as a trapping center. The most effective recombination centers are those located between the Fermi level at the surface and mid gap, with a maximal S when the value of the Fermi level is pinned at mid gap.

The ideality factor A of a device governed by interface recombination depends strongly on the ratio of doping concentrations on either side of the interface. For the case of materials with identical dielectric constants the dependence can be approximated by [184]:

$$A = 1 + \frac{N_A}{N_D} \tag{B.12}$$

For the case of $N_A = N_D$ an ideality factor of 2 is predicted, whereas $A = 1$ is expected for the case of a junction where $N_D >> N_A$. This is the case of chalcopyrite thin film solar cells. The recombination current can be then written as:

$$J = q\gamma_n N_V \left(exp\left(\frac{qV}{kT}\right) exp\left(\frac{-E_A}{kT}\right)\right) = J_{00} exp\left(\frac{qV}{kT}\right) exp\left(\frac{-E_A}{kT}\right) \tag{B.13}$$

where E_A is the potential barriers that holes have to surmount in order to reach the interface and recombine with electrons from the window. An ideality factor $A = 1$ is predicted in this case.

Recombination at the interface: tunneling enhancement

In this case, the general expression of the recombination current can be written as:

$$J = J_{00} exp\left(\frac{-E_A}{AkT}\right) exp\left(\frac{qV}{AkT}\right) \tag{B.14}$$

The activation energy of the saturation current is given by E_A, as in the case of thermally activated recombination at the interface. The ideality factor in this case is temperature dependent and follows:

$$A = \frac{E_{00}}{\alpha_v kT} coth\left(\frac{E_{00}}{kT}\right) \tag{B.15}$$

where E_{00} is again the characteristic energy of the transition from tunneling to thermally activated processes. If an external voltage is applied, it can happen that not all of it falls on the absorber. This is dealt with the inclusion of the correction factor α_v [164].

A summary of the discussion presented above is found in table B.1. For each of the recombination mechanism mentioned the corresponding activation energies of the saturation current density and the temperature dependence of the ideality factor is given. In real devices one or more of these mechanisms may dominate the electronic transport and changes can be recorded as a function of temperature or as a function of the illuminating conditions. In principle, these contributions can be identified from the analysis of J(V,T) curves as it will be shown in this chapter.

Table B.1: Recombination mechanisms in thin film solar cells with their corresponding predicted activation energies of the saturation current density and diode ideality factors as a function of temperature.

Recombination mechanism	Activation energy (E_A)of J_0	Ideality factor A
Bulk	E_g	1
Thermally activated SCR -single defect	E_g	2
Thermally activated SCR exponential defect distribution	E_g/A	$2T^*/T + T^*$; $1 \leq A \leq 2$
Tunneling SCR	N/A	$2\left(1 - E_{00}^2/3(kT)^2 + T/T^*\right)^{-1}$; $A \uparrow$ as $T \downarrow$
Thermally activated interface	$E_A < E_g$	$1 + N_A/N_D$; $1 \leq A \leq 2$
Tunneling interface	N/A	$E_{00}/\alpha_v kT \cdot coth\,(E_{00}/kT)$; $A \uparrow$ as $T \downarrow$

The total recombination current will be given by the addition of the different contributions resulting from the corresponding recombination processes, which can be generally written as:

$$J = \sum_{1} J_{0i}\left[exp\left(\frac{qV}{A_i kT}\right) - 1\right] \tag{B.16}$$

where i runs over the recombination processes involved in the transport.

Appendix C

List of symbols

Table C.1: Abbreviations

AM1.5G	Air Mass 1.5 Global
CBD	Chemical Bath deposition
CIGSSe	Copper indium-gallium sulphur-selenide ($Cu(In,Ga)(S,Se)_2$)
CIS	Copper indium sulfide ($CuInS_2$)
ESCA	Electron spectroscopy for chemical analysis
EF-TEM	Energy-filtered transmission electron microscopy
EQE	External quantum efficiency
fcc	Face centered cubic structure
FWHM	Full width at half maximum
hex	Hexagonal structure
HR-TEM	High-resolution transmission electron microscopy
IFMP	Inelastic free mean path
I(V)	Current-voltage characteristic
I(V,T)	Temperature dependent current-voltage characteristic
Lig	Ligand
PES	Photoelectron spectroscopy
PV	Photovoltaics
PVD	Physical vapour deposition
QE	Quantum efficiency
QNR	Quasi-neutral region
RTP	Rapid thermal processing
SEL	Stacked elemental layer

SEM	Scanning electron microscopy
SLG	Soda Lime glass
TCO	Transparent conductive oxide
TEM	Transmission electron microscopy
tetr	Tetragonal structure
TU	Thiourea $SC(NH_2)_2$
UHV	Ultra high vacuum
UPS	Ultraviolet photoelectron spectroscopy
XAES	X-ray excited Auger electron spectroscopy
XPS	X-ray photoelectron spectroscopy
ZTS	Tris (thiourea) zinc sulphate

Table C.2: Symbols

A	Activation energy of the saturation current
$\alpha_{1,2}$	Auger parameters
BE	Binding energy (also E_B)
χ	Electron affinity
$D_{n,p}$	Diffusivity of free electrons / holes
d	length
ΔE_C	Conduction band offset
ΔE_V	Valence band offset
E(x)	Electric field
E	Energy level
E_A	Activation energy of the saturation current
E_B	Binding energy (also BE)
E_C	Conduction band minimum
E_F	Fermi level
E_f	Energy of the final electronic state
$E_{Fn,Fp}$	Quasi-Fermi level for electron / holes
E_g	Energy band gap
E_i	Energy of the initial electronic state
E_{max}	Maximum electric field
E_T	Energy of defect level
E_{kin}	Kinetic energy
E_{00}	Characteristic energy of tunnelling-enhanced recombination

E_S	Surface energy
E_V	Valence band maximum
ϵ, ϵ_s	Relative dielectric constant
F(E)	Probability of electron occupation in the conduction band
f(t)	Time evolution of volume fraction
FF	Fill factor
Φ	Work function
G	Generation rate
g(t)	Turbidity of the chemical solution
h(t)	Transparency of the chemical solution
η	Energy conversion efficiency
I	Current
I	Light intensity
I_{ilu}	Illumination intensity
I_{mpp}	Current at maximum power point
I_0	Initial light intensity
I_{ref}	Reference light intensity
I_{rel}	Relative light intensity
I_{sc}	Short circuit current
J	Current density
J_D	Diode current density
J_L	Photogenerated current density
$j_{n,p}$	Current density of electrons / holes
J_0	Saturation current density
J_{00}	Prefactor of the saturation current density
J_R	Recombination current density
J_{sc}	Short circuit current density
k	rate constant
n	Avrami exponent, order of reaction
K_{sp}	Solubility product
$L_{n,p}$	Diffusion length for electrons / holes
L	Heat of solution
L_{eff}	Effective diffusion length
λ	wavelength, inelastic free mean path
$m^*_{e,h}$	Effective mass of electrons / holes
$\mu_{n,p}$	Mobility of electrons / holes
n	Free electron concentration
N_A	Ionized acceptor density
N_C	Conduction band effective density of states
N_D	Ionized donor density
n_i	Intrinsic free carrier concentration
N_V	Valence band effective density of states
ν	Frequency
p	Free hole concentration
$\mathbf{p}$, p	Momentum
P_{in}	Power input

P_{out}	Power output
R	Recombination rate
R_c	Critical nuclei radius
R_{max}	Maximum recombination rate
R_p	Parallel resistance
R_s	Series resistance
ρ	Density
ρ(x)	Charge density
S	Interface recombination velocity
σ	Surface energy per unit area
T	Temperature
T^*	Characteristic temperature of tunnelling process
t_i	Induction time
$\tau_{n,p}$	Carrier lifetime for electrons / holes
Θ	Angle
U	Width of UPS spectrum
V	Potential drop, voltage
V_{bi}	Built-in potential
V_{mpp}	Voltage at maximum power point
V_{oc}	Open circuit voltage
w	Space charge region width
$x_{n,p}$	Space charge region edges

Table C.3: Physical constants

q	$1.602 \cdot 10^{-19}$ C	Elementary charge
ϵ_0	$8.854 \cdot 10^{-12}$ F/m	Permitivity in vacuum
m_0	$9.11 \cdot 10^{-31}$ kg	Electron rest mass
h	$6.626 \cdot 10^{-34}$ J·s	Planck constant
k	$1.381 \cdot 10^{-23}$ J/K	Boltzmann constant
c	$2.998 \cdot 10^{8}$ m/s	Speed of light in vacuum

Acknowledgements

Reached this point I would like to thank all of those who have helped and contributed to this work:

- Above all, I would like to thank Prof. Lux-Steiner for letting my write my thesis at the Helmholtz-Zentrum Berlin, for allowing me to dive into the world of photovoltaics and for carefully correcting this work.
- Not to forget Prof. Pascual for accepting to be my second supervisor.
- My colleagues in the Physical Chemistry group, leaded by Dr. Ennaoui, and including Timo Kropp and various summer students with whom I have shared many hours in the laboratory.
- Rainer Klenk, whose door was always open for discussion and his group, specially Carola Kelch and Michael Kirsch, who fulfilled my whishes when it came to ZnO.
- The members of the CISSY group: I. Lauermann, H. Monig, A. Grimm, B. Johson (and M. Bär) and the whole SE2 department, specially the co-suffering PhD students.
- A. Belaidi for the hours at the SEM and M. Rusu for the hours at the IVT.
- The people at the technology department (SE3) for the scribing and the patterning of 10x10 cm^2 CIS modules and for the thermography images.
- The whole microscopy team: P. Schubert-Bischoff, U. Bloeck for the preparation of the TEM-samples and D. Abou-Ras for the investigation with energy-filtered TEM and the corresponding discussions.
- Our industrial partners in the ATHLET project, specially T. P. Niesen (AVANCIS), A. Neisser and K. Wilchelmi (SULFURCELL).
- Special thanks go to David Fuertes Marrón and Iver Lauermann for proof reading this work and for their constant support.
- And last, but not least, to Cristina and Aurora. El parto ha sido largo, pero la criatura es guapa.

Curriculum Vitae

For reasons of data protection,
the curriculum vitae is not included in the online version

List of publications

Patent

- *Verfahren zum Aufbringen einer Zn(S,O)-Pufferschicht auf ein Halbleitersubstrat mittels chemischer Badabscheidung.* A. Ennaoui, R. Sáez-Araoz, T. Kropp, M. Ch. Lux-Steiner. Patent pending (2009)

Journal Publications

- *In situ monitoring the growth of thin-film ZnS/Zn(S,O) bilayer on Cu-chalcopyrite for high performance thin film solar cells.*
  R. Sáez-Araoz, D. Abou-Ras, T. P. Niesen, A. Neisser, K. Wilchelmi, M. Ch. Lux-Steiner, A. Ennaoui
  Thin Solid Films 517:7, pp. 2300-2304 (2009).

- *Use of different Zn precursors for the deposition of Zn(S,O) buffer layers by chemical bath deposition for chalcopyrite-based Cd-free thin-film solar cells.*
  R. Sáez-Araoz, A. Ennaoui, T. Kropp, E. Veryaeva, T. P. Niesen, M. Ch. Lux-Steiner.
  Phys. Stat. Sol (a) Vol 205, Issue 10. pp 2330-2334. (2008).

- *Formation of a ZnS/Zn(S,O) bilayer buffer on $CuInS_2$ thin film solar cell absorbers by chemical bath deposition.*
  M. Bär, A. Ennaoui, J. Klaer, T. Kropp, R. Sáez-Araoz, N. Allsop, I. Lauermann, H. -W. Schock, M. C. Lux-Steiner.
  J. Appl. Phys. 99, 123503 (2006).

- *Intermixing at the heterointerface between ZnS/Zn(S,O) bilayer buffer and $CuInS_2$ thin film solar cell absorber.*
  M. Bär, A. Ennaoui, J. Klaer, T. Kropp, R. Sáez-Araoz, S. Lehmann, A.Grimm, I. Lauermann, Ch. Loreck, St. Sokoll, H. -W. Schock, Ch. -H. Fischer, M. C. Lux-Steiner.
  J. Appl. Phys. 100, 064911 (2006).

- *The electronic structure of the [Zn(S,O)/ZnS]/$CuInS_2$ heterointerface - Impact of post-annealing.*
  M. Bär, A. Ennaoui, J. Klaer, R. Sáez-Araoz, T. Kropp, L. Weinhardt, C. Heske, H. -W. Schock, Ch. -H. Fischer, M. C. Lux-Steiner.
  Chem. Phys. Lett. 433, 71-74 (2006).

- *Highly-efficient Cd-free CuInS$_2$ thin-film solar cells ans mini-modules with Zn(S,O) buffer layers prepared by an alternative chemical bath process.*
  A. Ennaoui, M. Bär, J. Klaer, T. Kropp, R. Sáez-Araoz, M. Ch. Lux-Steiner.
  Prog. Photovolt: Res. Appl. (2006); 14:499-511.

Conference Proceedings

- *Chemical composition and electronic properties of CuInS$_2$/Zn(S,O) interfaces.*
  R. Sáez-Araoz, I. Lauermann, A. Neisser, M. Ch. Lux-Steiner, A. Ennaoui.
  2009 Material Research Society Spring Meeting. San Francisco, USA, 13th-17th April 2009.

- *Current transport in Cu(In,Ga)S$_2$ based solar cells with high open circuit voltage - Bulk vs. Interface.*
  S. Merdes, B. Johnson, R. Sáez-Araoz, A. Ennaoui, J. Klaer, I. Lauermann, R. Mainz, A. Meeder, R. Klenk.
  2009 Material Research Society Spring Meeting. San Francisco, USA, 13th-17th April 2009.

- *High performance thin film Cu-Chalcopyrite PV-devices with a Zn(S,O) buffer layer.*
  R. Sáez-Araoz, A. Ennaoui, T. P. Niesen, A. Neisser, K. Wilchelmi, M. Ch. Lux-Steiner.
  Proc. 23rd European Photovoltaic Solar Energy Conference, pp. 2133-2136. 1-5 September 2008, Valencia, Spain.

- *Scaling up of efficient Cd-free thin film Cu(In,Ga)(S,Se)$_2$ and CuInS$_2$ PV-devices with a Zn(S,O) buffer layer.*
  R. Sáez-Araoz, A. Ennaoui, T. P. Niesen, A. Neisser, M. Ch. Lux-Steiner.
  Proc. 22nd European Photovoltaic Solar Energy Conference, pp. 2133-2136. 3-7 September 2007, Milan, Italy.

- *Highly Efficient CuInS2-based solar cell devices with an optimized Cd-free window structure.*
  A. Ennaoui, M. Bär, M. Rusu, R. Klenk, J. Klaer, T. Kropp, R. Sáez-Araoz, H. -W. Schock, and M. C. Lux-Steiner.
  Proc. 21st European Photovoltaic Solar Energy Conference, pp. 1835-1838. 4-8 September 2006, Dresden, Germany.

- *New chemical route for the deposition of ZnS buffer layers: Cd-free CuInS$_2$-based thin film solar cells with efficiencies above 11%.*
  A. Ennaoui, M. Bär, J. Klaer, T. Kropp, R. Sáez-Araoz, M. Ch. Lux-Steiner.
  Proc. 20th European Photovoltaic Solar Energy Conference, pp. 1882-1885. 6-10 June 2005, Barcelona, Spain.

Bibliography

[1] A. S. Blinder. Economic Policy and the great stagflation. Academic Press. New York. 1979.

[2] World Health Organization. Informe sobre la evaluación mundial del abastecimiento de agua y el saneamiento en 2000 (2001)

[3] Marketbuzz^{TM} 2008: Annual world solar photovoltaic industry report. http://www.solarbuzz.com/Marketbuzz2008-into.htm

[4] R. Haas, Solar Energy 54, pp. 25-31. 1995.

[5] M. Gloeckler. Device Physics of Cu(In,Ga)Se_2 thin-film solar cells. Dissertation. (2005). Colorado State University.

[6] National Renewable Energa Laboratory. What is energy payback for PV? URL: http://www.nrel.gov/docs/fy04osti/35489.pdf.

[7] I. Repins, M. A. Contreras, B. Egaas, C. DeHart, J. Scharf, C. L. Perkins, B. To, R. Noufi. Prog. Photovoltaic: Research and Appl. (2008); 16(3): 235-239.

[8] C. A. Kaufmann, R. Klenk, M. Ch. Lux-Steiner, A. Neisser, P. Korber, R. Scheer, H. W. Schock. Proceedings of the 20^{th} European Photovoltaic Solar Energy Conference, Barcelona, Spain (2005).

[9] R. Caballero, C. A. Kaufmann, T. Eisenbarth, M. Cancela, R. Hesse, T. Unold, A. Eicke, R. Klenk, H. W. Schock. Thin Solid Films 517 (2009) p. 2187-2190.

[10] M. Bär. Neuartige Cd-freie Fensterstruktur für Chalkopyrit-Dünnschichtsolarzellen. PhD. Thesis. Technische Universität Berlin, (2003).

[11] S. B. Zhang, S. -H. Wei, A. Zunger. Phys. Rev. Lett. 78 (1997) pp. 4059-4062.

[12] Sulfurcell Solartechnik GmbH. URL: http://www.sulfurcell.de

[13] AVANCIS GmbH & Co. KG. URL: http://www.avancis.de

[14] J. Palm, V. Probst, W. Stetter, R. Toelle, S. Visbeck, H. Claver, T. Niesen, H. Vogt, O. Hernandez, M. Wendl, F. H. Karg. Thin Solid Films. 451-452, pp. 544-551 (2004).

[15] N. Meyer, A. Meeder, D. Schmid. Thin Solid Films. 515 pp. 5979-5984 (2007).

[16] K. Granath. The influence of Na on the growth of CIGSe layers for thin film solar cells, PhD. Thesis, University of Uppsala (1999).

[17] S. Schuler. Transporteigenschaften und Defekte in polykristallinen $CuGaSe_2$-Schichten und Heterostrukturen. PhD. Thesis, Freie Universität Berlin (2000).

[18] R. Scheer, R. Klenk, J. Klaer, I. Luck. Solar Energy 77. pp. 777-784 (2004)

[19] M. Weber, R. Scheer, H. J. Lewerenz, U. Störkel, H. Jungblut. Proc. of Spring meeting E-MRS, Strasbourg, France, (1999).

[20] L. Kronik, L. Burstein, M. Leibovich, Y. Shapira, D. Gal, E. Moons, J. Beier, G. Hodes, D. Cahen, D. Hariskos, R. Klenk, H. -W. Schock. Appl. Phys. Lett. 67. 1405. (1995)

[21] A. Rumberg. Chemische Gasphasendeposition von ZnSe-Puffern für die Anwendung in Chalkopyrit-Dünnschichtsolarzellen. PhD Thesis, Freie Universität Berlin, (2001).

[22] K. Ramanathan, H. Wiesner, S. Asher, D. Niles, R. N. Bhattacharya, J. Keane, M. A. Contreras, R. Noufi. Proc 2^{nd} world conference and exhibition on photovoltaic energy conversion. Luxemburg (1998). pp. 477-481.

[23] A. Kylner. J. Appl. Phys. 85, 9. (1999).

[24] N. A. Allsop, A. Schönmann, H. -J. Muffler, M. Bär, M. C. Lux-Steiner, Ch. -H. Fischer. Prog. Photovoltaic: Research and Appl. 13:607.(2005), 1-10.

[25] P. Pistor, R. Caballero, D. Hariskos, V. Izquierdo-Roca, R. Wächter, R. Klenk. 17^{th} International Photovoltaic Science and Engineering Conference (PVSEC-17): Fukuoka, Japan, 2007. p. 1-2.

[26] C. Platzer-Björkman, T. Törndahl, D. Abou-Ras, J. Malmström. J. Appl. Phys. 100, 044506 (2006).

[27] U. Rau, M. Schmidt. Thin Solid Films 387 (2001) pp. 141-146.

[28] S. M. Sze. Physics of semiconductor devices. John Wiley & sons, 1981.

[29] M. Gloeckler, J. R. Sites. Thin Solid Films 480-481 (2005) pp. 241-245.

[30] R. Klenk. Thin Solid Films 387 (2001) pp.135-140.

[31] I. Hengel. Ladungsträgertransport und Rekombinationsmechanismen in Chalkopyrit-Dünnschichtsolarzellen. PhD. Thesis, Freie Universität Berlin. Fachbereich Physik (2002).

[32] J. Reiss. Generation und Rekombination von Ladungsträger in $CuInS_2$ Dünnschichtsolarzellen. PhD. Thesis, Freie Universität Berlin. Fachbereich Physik (2002).

[33] S. S. Hegedus, W. N. Shafarman. Prog. Photovoltaics 12, 155 (2004).

[34] A. R. Burgers, J. A Eikelboom, A. Schönecker, W. C. Sinke. Proc. 25^{th} IEEE PVSEC, Washington DC. pp 569-572 (1996).

[35] S. Tober. Herstellung und Charakterisierung von Dünnschicht-Solarzellen auf der Basis von $CuGaSe_2$ und $CuInSe_2$, Diplomarbeit, Freie Universität Berlin, Fachbereich Physik (1999).

[36] D. Fuertes-Marrón. Structural and electronic characterization of thin film solar cells based on CVD-grown $CuGaSe_2$. Ph.D. Thesis. Freie Universität Berlin. Fachbereich Physik. May 2003.

[37] M. Green. Solar Cells. Prentice Hall, Englewood Cliff, NJ, 1982.

[38] M. A. Green, K. Emery, Y. Hishikawa, W. Warta. Prog. Photovolt: Res. Appl. 2009; 17:85-94.

[39] D. M. Dobkin, M. K. Zuraw. Principles of Chemical Vapor Deposition. Kluwer Academic (2003).

[40] J. Liebig. Ann. Pharma. 14:124, 1835.

[41] C. Puscher. Dingl. J. 190:421, 1869.

[42] J. Emerson-Reynolds. J. Chem. Soc. 45:162, 1884.

[43] G. Rosenheim, W. Stadler, V.J. Mayer. Z. Anorg. Chem. 49:1, 1906.

[44] G. Rosenheim, W. Stadler, V.J. Mayer. Z. Anorg. Chem. 49:13, 1906.

[45] R. H. Bube. Photoconductivity of Solids. New York: Wiley 1960.

[46] D. E. Bode. Physics of Thin Films, Vol 3. Academic Press, New York and London, 1966, p 275.

[47] S. G. Mokrushin, Y. V. Tkachev. Kolloidn Zh. 23:438, 1961.

[48] R. Ortega-Borges, D. Lincot. J. Electrochem. Soc. 140:3464, 1993.

[49] S. Gorer, G. Hodes. J. Phys. Chem 98:5338, 1994.

[50] A. Ennaoui, M. Weber, R. Scheer, H. J. Lewerenz. Sol. Energy Mater. Sol. Cells 54:277, 1998.

[51] G. K. Padam, S. K. Gupta. Appl. Phys. Lett. 53:865, 1998.

[52] R. N. Bhattacharya. J Electrochem. Soc. 130:2040, 1983.

[53] G. N. Chaudhari, S. Manorama, V. J. Rao. J. Phys. D: Appl. Phys. 25:862, 1992.

[54] K. Kushiya, T. Nii, I. Sugiyama, Y. Sato, Y. Inamori, H. Takeshita. Jpn. J. Appl. Phys, 35:4383, 1996.

[55] T. L. Chu, S. S. Chu, C. Ferekides, C. Q. Wu, J. Brit, C Wang. J. Appl. Phys 70:7608, 1991.

[56] B. Basol, V. Kapur. IEEE Trans. Electron. Dev. 37:418, 1990.

[57] G. Hodes Chemical solution deposition of semiconductor films, Marcek Dekker, Inc. New York, Basel 2003.

[58] I. Kaur, D. K. Pandya, K. L. Chopra. J. Electrochem Soc. 127, 943 (1980).

[59] M. Froment, D. Lincot. Electrochimica Acta, Vol. 40, No. 10, pp.1293-1303, (1995).

[60] P. O'Brien, J. McAleese. J. Mater. Chem. 1998, 8(11), 2309-2314.

[61] W. Ostwald. Lehrbuch der Allgemeinen Chemie, Vol. 2, part 1. Leipzig, 1896.

[62] L. Ratke, P. W. Voorhees. Growth and Coarsening: Ostwald Ripening in Material Processing, Springer 2002.

[63] R. T. Morrison and R. N. Boyd. Organic Chemistry, 4^{th} ed. Allyn and Bacon, Inc. Boston, MA. 1983

[64] T. Nakada, M. Mizutani. Jpn. J. Appl. Phys. 2002; 41: L165-L167

[65] A. Ennaoui, U. Blieske, M. C. Lux-Steiner. Progress in Photovoltaics: Research and application 1998; 6: 447-451.

[66] A. Ennaoui, W. Eisele, M. C. Lux-Steiner, T. P. Niesen, F. Karg. Thin Solid Films 431-432, (2003) pp. 335-339.

[67] A. Ennaoui, S. Siebentritt, M. C. Lux-Steiner, W. Riedl, F. Karg. Sol. Energy Mater. Sol. Cells 2001; 67:31-40.

[68] R. N. Bhattacharya, M. A. Contreras, G. Teeter. Jpn. J. Appl. Phys. 2004; 43: L1475-L1476.

[69] K. Kushiya, M. Ohshita, I. Hara, Y. Tanaka, B. Sang, Y. Nagoya, M. Tachiyuki, D. Yamase. Sol. Energy Mater. Sol. Cells 2003; 75: 171-178.

[70] M. A. Contreras, T. Nakada, M. Hongo, A. O. Pudov, J. R. Sites. Proceedings of 3rd World Conference on Photovoltiac Energy Conversion (WCPEC-3), Osaka, Japan 2003; 570.

[71] A. Ennaoui. Canadian Journal of Physics 1999; 77: 723-729.

[72] S. D. Sartale, B. R. Sankapal, M. Lux-Steiner, A. Ennaoui. Thin Solid Films, 480-481, (2005) pp.168-172.

[73] A. Ennaoui, M. Bär, J. Klaer, T. Kropp, R. Sáez-Araoz, M. Ch. Lux-Steiner. Proceeding of the 20^{th} EU-PVSEC, 6-10 June 2005, Barcelona, Spain. pp 1882-1885.

[74] A. Ennaoui, M. Bär, J. Klaer, T. Kropp, R. Sáez-Araoz, M. Ch. Lux-Steiner. Prog. Photovolt: Res. Appl. 2006; 14:499-511.

[75] A. Ennaoui, T. Kropp, M. Ch. Lux-Steiner. German Patent. Publication number: WO/2006/018013, 2006.

[76] J. Ramajothi, S. Dhanuskodi and K. Nagarajan. Crys. Res. Technol. 39, No. 5, 414-420, 2004.

[77] J. M. Doña and J. Herrero. J. Electrochem. Soc. Vol 141, No. 1, 1994.

[78] A. M. Chaparro, M. T. Gutiérrez, J. Herrero, J. Klaer, M. J. Romero, M. M. Al-Jassim. Prog. Photovolt: Res. Appl. 2002; 10:465-480.

[79] ASTM International, 2003a, D1889-00 Standard test method for turbidity of water, in ASTM International, Annual Book of ASTM Standards, Water and Environmental Technology, 2003, v.11.01, West Conhohocken, Pennsylvania, 6 p.

[80] C. W. Anderson. USGS field manual on measuring turbidity.
http://water.usgs.gov/owq/FieldManual/Chapter6/6.7_contents.html

[81] S. Jun, H. Zhang, J. Bechhoefer. Physical Review E 71, 011908 (2005).

[82] R. Zhai, R. Wang, H. Wang, M. Zhu, H. Yan. J. Phys. D: Appl. Phys. 40 (2007) 4039-4042.

[83] M. Avrami. Journal of chemical Physics. Vol. 7 (1939) 1103-1112.

[84] M. Avrami. Journal of chemical Physics. Vol. 8 (1940) 212-224.

[85] M. Avrami. Journal of chemical Physics. Vol. 9 (1941) 177-184.

[86] C. P. Yang, J. F. Nagle. Phys. Rev. A 37, 3992 (1998).

[87] B. Kämpfer. Ann. Phys. (Leipzig) 9, 1, (2000).

[88] L. Gránásy, T. Pusztai, G. Tegze, J. A. Warren, J. F. Douglas. Physical Review E 72, 011605 (2005).

[89] M. Iwamatsu. J. Chem. Phys. 128, 084504 (2008).

[90] I. Foubert, P. A. Vanrolleghem, B. Vanhoutte, K. Dewettinck. Food Research International 35 (2002) 945-956.

[91] B. Wünderlich. Thermal analysis. New York: Academic Press (1990).

[92] C. D. Lokhande. Materials Chemistry and Physics, 27, 1-43, 1991.

[93] K. Yamaguchi, T. Tsukasa, D. Lincot, H. Minoura. J. Phys. Chem. B 2003, 107, 387-397.

[94] S. Neve, W. Bohne, J. Röhrich, R. Scheer. Mat. Res. Soc. Symp. Proc. Vol 688 (2001)

[95] P. O'Brien, D. J. Otway, D. Smyth-Boyle. Thin Solid Films 361-362 (2000) pp.17-21.

[96] A. Ennaoui. Internal report NEBULES. EU-Project ENK6 2002-00664.

[97] D. Lincot, R. Ortega-Borges. J. Electrochem. Soc. 139 (1992) 1880.

[98] Ch. Kaufmann. Chemical Bath Deposition of Thin Semiconductor Films for Use as Buffer Layers in $CuInS_2$ Thin Film Solar Cells. PhD. Thesis. Department of Engineering Science. University of Oxford. 2002.

[99] U. Gangopadhyay, K. Kim, S. K. Dhungel, H. Saha, J. Yi. Advances in OptoElectronics, Vol. 2007, 18619.

[100] I. Lauermann, T. Kropp, D. Vottier, A. Ennaoui, W. Eberhardt, E. F. Aziz. ChemPhysChem 2009, 10, 532-535.

[101] A. Ennaoui, M. Bär, J. Klaer, T. Kropp, R. Sáez-Araoz, M. Ch. Lux-Steiner. Prog. Photovolt: Res. Appl. 2006; 14:499-511.

[102] J. Touskova, D. Kindl, J. Tousek. Thin Solid Films 293 (1996) pp.272-276.

[103] A. Ennaoui, R. Sáez-Araoz, T. Kropp, M. Ch. Lux-Steiner. Verfahren zum Aufbringen einer Zn(S,O)-Pufferschicht auf ein Halbleitersubstrat mittels chemischer Badabscheidung. Patent pending. (2009).

[104] L. de Broglie. Recherches sur la théorie des quanta (Researches on the quatum Theory). Thesis. Paris. 1924.

[105] E. Ruska. Über ein magnitisches Objektiv für das Elektronenmikroskop. Dissetation, Technische Universität Berlin (1933). Published in Z. Phys. 89. p.90 (1934).

[106] J. I. Goldstein, D. E. Newbury, P. Echelin, D. C. Joy, A. D. Romig, C. E. Lyman, C. Fiori, E Lifshin. Scanning electron microscopy and X-ray microanalysis. Plenum Press (1992).

[107] L. Reimer. Transmission electron microscopy, physics of image formation and microanalysis. Springer Series in Optical Sciences (1997).

[108] R. Sáez-Araoz, A. Ennaoui, T. Kropp, E. Veryaeva, T. P. Niesen. M. Ch. Lux-Steiner. Phys. Stat. Sol. (a). Vol. 205. Issue 10. pp. 2330-2334 (2008).

[109] G. Schimmel. Elektronenmikroskopische Methodik. Springer Verlag, Berlin, Heidelberg, New York. 1969.

[110] B. Beeston, R. Horne, R. Markham. Electron diffraction and optical diffraction techniques. North Holland / American Elsevier, Amsterdam, London, New York. 1972

[111] R. Stahl et al. Z. Anprg. Allg. Chem. 624, 1130 (1998). ICSD 050447.

[112] A. N. Christensen. Acta Chem. Scand. 23, 2016 (1969). ICSD 015008.

[113] M. I. Baneeva, S. V. Popova. Geokhimiya 1969, 1014 (1969) ICSD 020285.

[114] B. Dubey, N. Tiwari. Bull. Chem. Soc. Jpn. 65, 495 (1992).

[115] A. Clark et al. Mineral. Mag. 48, 276 (1984).

[116] A. Clark et al. Mineral. Mag. 52, 699 (1988).

[117] C. Yeh et al. Phys. Rev. B: Condens. Matter. 46, 10086 (1992). ICSD 067790 and 067777.

[118] H. Sawada, R. Wang, A. W. Sleight. J. Solid State Chem. 122, 148 (1996). ICSD 082029.

[119] H. Hahn et al. Z. Anorg. Allg. Chem. 271, 153 (1953). ICSD 028739.

[120] R. Sáez-Araoz, D- Abou-Ras, T. P. Niesen, A. Neisser, K. Wilchelmi, M. Ch. Lux-Steiner. Thin Solid Films 517:7, pp. 2300-2304 (2009)

[121] A. Einstein, Ann. Phys. 17. pp. 132-148. 1905.

[122] K. Siegbahn, C. Nordling, A. Fahlman, H. Nordberg, K. Hamrin, J. Hedman, G. Johansson, T. Bergmark, S. E. Karlssom, J. Lindgren, B. Lindberg. Electron spectroscopy for chemical analysis: atomic, molecular and solid state structure studies ba means of electron spectroscopy. Almquist and Wiksells (1967).

[123] D. Briggs, M. P. Seah, editors. Practical Surface Analysis by Auger and X-ray Photoelectron Spectroscopy. John Wiley & Sons, Chichester, 1983.

[124] C. D. Wagner, W. M. Riggs, L. E. Davis and J. F. Moulder. Handbook of X-ray photoelectron spectroscopy. Perkin Elmer Cooperation, Eden Prarie, 1978.

[125] NIST X-Ray Photoelectron Spectroscopy Database, NIST Standard Reference Database 20, Version 3.4, http://srdata.nist.gov/xps/

[126] P. Auger. Sur l'effect photoélectrique composé. J. Phys. Radium 6 pp.205-208. (1925).

[127] L. Weinhardt. Elektronenspektroskopische Untersuchungen an Grenzflächen und Oberflächen in Cu(In,Ga)(S,Se)$_2$ Dünnschichtsolarzellen. Master Thesis, Bayerische Julius-Maximilian-Universität Würzburg (2001).

[128] J. H. Scofield. J. Electr. Spectr. rel. Phen. 8, 129 (1976).

[129] M. Bär. Neuartige Cd-freien Fensterstruktur für Chalkopyrit-Dünnschichtsolarzellen. Ph. D. Thesis. Technische Universität Berlin (2003).

[130] I. Lauermann et al. Mater. Res. Soc. Symp. Proc. 763, B4.5.1 (2003).

[131] D. Briggs, M. P. Seah. Auger and X-ray Photoelectron Spectroscopy, Practical Surface Analysis Vol. 1. Wiley, New York, 1990.

[132] S. Tanuma, C. J. Powell, D. R. Penn. Surf Interface Anal. 21, 165 (1993).

[133] S. Tougaard. QUASES-IMFP-TPP2M code for the calculation of the inelastica electron mean free path, Version 2.2, http://www.quases.com

[134] M. Bär, A. Ennaoui, J. Klaer, T. Kropp, R. Sáez-Araoz, N. Allsop, I. Lauermann, H.-W. Schock, M. C. Lux-Steiner. J. Appl. Phys. 99, 123503 (2006).

[135] Gmelins Handbuch der Anorganischen Chemie-Ergänzungsband Zinc, Syst. -Nr. 32, edited by E. H. E. Pietsch (Verlag Chemie GmbH, Weinheim, 1956).

[136] C. D. Wagner. Faraday Discuss. Chem. Soc., 1975, 60, 291 - 300.

[137] L. S. Dake, D. R. Baer, J. M. Zachara. Surf. Interface Anal. 14, 71 (1989).

[138] S. W. Gaarenstroom, N. Winograd. J. Chem. Phys. 67, 3500, (1977).

[139] B. R. Strohmeier, D. M. Hercules. J. Catal. 86, 266 (1984).

[140] D. W. Langer, C. J. Vesely. Phys. Rev. B 2, 4885 (1970).

[141] J. D. G. Durán, M. C. Guindo, A. V. Delgado. J. Colloid and Interface Science. 173, 436-442 (1995).

[142] B. L. Sharma, R. K. Purohit. Semiconductor heterojuctions. Pergamon Press (1974).

[143] R. L. Anderson. Sol. St. Electr. 5 pp.341-351 (1962).

[144] M. Bär, A. Ennaoui, J. Klaer, T. Kropp, R. Sáez-Araoz, S. Lehmann, A. Grimm, I. Lauermann, Ch. Loreck, St. Sokoll, H. -W. Schock, Ch. -H. Fischer, M. C. Lux-Steiner. J. Appl. Phys. 100, 064911 (2006).

[145] J. Tersoff. Heterojunction band discontinuities: physics and device applications. pp.3-57. Ed. F. Capasso and G. Margaritondo. Elsevier Sci. Publishers (1987).

[146] W. R. Frensley, H. Kroemer. Phys. Rev. B., 16, 2642 (1997).

[147] A. D. Katnami, G. Margaritondo. Phys. Rev. B 28 pp.1944-1956 (1983).

[148] M. Sugiyama, H. Nakanishi, S. F. Chichibu. Jpn. J. Appl. Phys. 40 pp.L428-L430 (2001).

[149] M. Turowski, G. Margaritondo, M. H. Kelly, R. D. Thomlinson. Phys. Rev. B 31 pp.1022-1027 (1985).

[150] V. Nadenau, D. Branger, D. Hariskos, H. W. Schock. Inst. Phys. COnf. Ser. 152 pp.955-958 (1998).

[151] A. Bauknecht, U. Blieske, T. Kampschulte, J. Albert, H. Sehnert, M. Ch. Lux-Steiner, a Klein, W. Jaegermann. Appl. Phys. Lett. 74 (1999).

[152] Y. Hashimoto, K. Takeuchi, K. Ito. Appl. Phys. Lett. 67 (1995).

[153] A. Klein, T. Löher, Y. Tomm, C. Pettenkoffer, W. Jaegermann. Appl. Phys. Lett. 70 (1997).

[154] T. Löher, W Jaegermann, C. Pettenkoffer. J. Appl. Phys. 77 (1995).

[155] Dr. I. Lauermann. Private communication.

[156] R. Scheer, H. J. Lewerenz. J. Vac. Sci. Technol. A 12 (1994) 51.

[157] R. Scheer, H. J. Lewerenz. J. Vac. Sci. Technol. A 12 (1994) 56.

[158] L. Weinhardt, O. Fuchs, F. Groß, G. Storch, E. Umbach, N. G. Dhere, A. A. Kadam, S. S. Kulkani, C. Heske. Appl. Phys. Lett. 86, 062109, (2005).

[159] M. Bär, A. Ennaoui, J. Klaer, R. Sáez-Araoz, T. Kropp, L. Weinhardt, C. Heske, H. -W. Schock, Ch. -H. Fischer, M. C. Lux-Steiner. Chem. Phys. Lett. 433, (2006), pp.71-74.

[160] H. J. Muffler, Ch. H. Fischer, M. Giersig, M. Bär, M. C. Lux-Steiner. J. Appl. Phys. 91, 10 (2002).

[161] T. Nakada, M. Hongo, E. Hayashi. Thin Solid Films. 431-432 (2003) 242-248.

[162] U. Rau. Appl. Phys. Lett. 74 (1999) pp. 111-113.

[163] U. Malm, J. Malmström, C. Platzer-Björkman, L. Stolt. Thin Solid Films 480-481 (2005) pp. 208-212

[164] V. Nadenau, U. Rau, A. Jasenek, H. -W. Schock. J. Appl. Phys. 87 (2000) p. 584.

[165] U. Rau, A. Jasenek, H. -W. Schock, F. Engelhardt, T. Meyer. Thin Solid Films, 361-362 (2000) p. 298.

[166] U. Rau, H. -W. Schock. Appl Phys. A, 69 (1999) p. 131.

[167] J. Reiß, J. Malmström, A. Werner, I. Hengel, R. Klenk, M. Ch. Lux-Steiner. Mat. Res. Soc. Symp. Porc. Vol. 668 (2001).

[168] A. Ennaoui, M. Bär, M. Rusu, R. Klenk, J. Klaer, T. Kropp, R. Sáez-Araoz, H. -W. Schock, and M. C. Lux-Steiner. Proc. 21^{st} European Photovoltaic Solar Energy Conference, pp. 1835-1838. 4-8 September 2006, Dresden, Germany.

[169] R. Scheer. Proc. 23^{rd} European PVSEC, Valencis, September (2008).

[170] M. Burgelmann, P. Nollet, S. Degrave. Thin Solid Films. 361-362. pp. 527-532 (2000).

[171] A. Niegemeers, M. Burgelmann. In 25^{th} IEEE PVSC, Washington D.C. U.S.A. (1996).

[172] R. Márquez, C. Rincón. Phys. Stat. Sol. (b), 191. pp. 115-119 (1995).

[173] S. A. Studenikin, N. Golego, M. Cocivera. J. Appl. Phys. 87(5) pp. 2413-2421 (2000).

[174] I. Dirnsthofer, D. M. Hofmann, D. Meister, B. K. Meyer, F. Börner, R. Krause-Rehberg, F. Karg. In 2^{nd} WCPEC, Vienna, July (1998).

[175] C. Kaufmann. Herstellung von $CuInS_2$-Absorberschichten für photovoltaische Anwendungen. Diplomarbeit. Fachbereich Physik, Freie Universität Berlin (1997).

[176] H. K. Henisch. Semiconductor COntacts - An approach to ideas and models. Clarendon Press, Oxford 1989.

[177] Directive 2002/95/EC of the European Parliament and of the Council of 27 January 2003 on the restrictions of the use of certain hazardous substances in electrical and electronic equipment. Official Journal of the Europena Union. L 37. pp. 19-23. (2003).

[178] W. Shockley, W. T. Read, Jr. Phys. Rev. 87 (1952) pp. 853-842.

[179] R. N. Hall. Phys. Rev. 87 (1952) p. 387.

[180] G. A. M. Hurkx, D. B. M. Klaasen, M. P. G. Knuvers. IEEE Trans. Electron. Devices. ED39 (1992) pp. 331-338.

[181] J. P. McKelvey. Solid state and semiconductor physics. Chapters 12 and 13. Harper & Row (1966).

[182] T. Walter, R. Herberholz. H. W. Schock. Solid State Phenomena 51-52 pp. 309-316 (1996).

[183] D. T. Stevenson, R. J. Keyes Physica 20 (1954) pp. 1041-1046.

[184] A. L. Fahrenbuch, R. H. Bube. Fundamentals of solar cells, photovoltaic energy conversion. Academic Press (1983) p. 42.

Erklärung

Hiermit erkläre ich, dass ich die vorliegende Arbeit selbständig verfasst und keine anderen als die angegebenen Quellen und Hilfsmittel benutzt habe.

Berlin, den.. Unterschrift..